

Scuola Normale Superiore

Ph.D. Thesis in Nanosciences

Gate tunable coherent heat transport: Study of the heat transfer in gate controlled hybrid superconducting systems

---

Author:
Sebastiano Battisti

Supervisor:
Dr. Francesco Giazotto
Dr. Giorgio De Simoni

A thesis submitted in fulfillment of the requirements
for the degree of Doctor of Philosophy
in

Nanosciences

Acknowledgements

The journey of a PhD thesis is definitely a challenging one, and without the support and guidance of people surrounding me it would not have been possible to finish this journey. My deepest gratitude goes to all of them.

First of all, I would like to express my deepest gratitude to Francesco Giazotto, my supervisor during this four years, for his support and everyday advices that he bring in the labs. He taught me how to be independent and he never missed to encourage me in front of harsh problems. His ideas and enthusiasm are one of the reasons which make the SQEL group a fantastic one.

I will always be in debt with Giorgio De Simoni, my other supervisor, who was (literally) always present in the lab when I needed his help. When I started my master thesis in this group he began to teach me how to measure physical processes and until the last day in lab he was a never ending source of great ideas and troubleshooting. I definitely was very lucky to work with such a scientist and person.

I would also like to acknowledge Fabio Beltram, who kindly accepted to be my intern supervisor and during my first year taught me never to settle for mediocrity.

I am thankful to Alessandro Paghi, my nearest colleague, who became a trusted researcher and friend during our fight against the Indium Arsenide. I really have to express my gratitude to him for his ideas inside the cleanroom and the laboratories, without him this thesis would not have been the same.

I have to express my gratitude to the other members of the group, Elia Strambini, Alessandro Crippa and Angelo Greco who always were ready to discuss about physics and gave me precious advices.

Many thanks to Alessandro Braggio, the theoretical father of my works. I am thankful to his non experimentalist-like vision which surely made our works better.

I would also like to thank Claudio Puglia, who left our group some years ago but taught me all the secrets of the cleanroom during the time we spent together.

I am indebted also with all the people at NEST who helped my in everyday challenges, such as the technical staff Claudio and Pietro, the cleanroom managers Daniele and Frnaco (before) and Domenica and Leonardo (after), Lucia Sorba and her group who supported our research with their substrates.
I would also like to thank all my colleagues and friends inside the group, who helped creating an enjoyable environment in the lab: Giacomo, one of the most skilled physicists I know; Matteo: always kind and polite and incredibly prepared in physics; and Filippo, Laura and Elisa.
I don't want to forget the friends from outside who seriously changed my life from the first year of the bachelor degree to nowadays. Thank you Alessandro, Francesco, Giulio, Giulia, Leonardo and Lorenzo for dealing with me and my continuous delays.
I can't forget my friends back home: Edoardo, my lifetime best friend, Matteo, Francesca, Giacomo, Francesco Paolo, Altea, Carolina, Edoardo, Niccolò, Christian, and all the others. You can't imagine how the time spent with you recharges my energies and makes me ready for new challenges.
A special thank to my band mates: Francesco, Filippo, Andrea, Hilary, Michele and Fabrizio. I found a second family when we met and playing with you really changed my life in the last 3 years.
Last but not least, I would like to express my deepest and unconditioned gratitude to my family. My parents Emiliano and Patrizia made me the person I am today (for better and for worse) and supported me in every sense since the day I was born, I really don't know how to say thank you. My grandparents which are still here and the ones passed away: Tosca, Lido, Assunta and Aldo, I know you are my everlasting supporters. My in-laws Ionuţ and Petronela and my brother in-law Vlad, since the day we met I have always felt how much you support and love me. Finally, my soulmate, Aida; you are my everyday partner and I know how much effort it takes, thank you for always being at my side. This thesis is dedicated to you all.

List of Publications

The main topics of this thesis consist of the overview of my core studies during the PhD (publications **1**, **2**, **3**), as well as the fundamental supplementary works (publications **4**, **5**). Publications **6**, **7**, and **8** are not included in this work as they are related to different topics (supercurrent rectification and non-centrosymmetric materials).

[1] **S. Battisti**, G. De Simoni, L. Chirolli, A. Braggio and F. Giazotto. "*Bipolar thermoelectric superconducting single electron transistor*", Physical Review Research **6**, L012022 (2024).

[2] **S. Battisti**, G. De Simoni, A. Braggio, A. Paghi, L. Sorba and F. Giazotto. "*Extremely weak sub-Kelvin electron-phonon coupling in InAs on Insulator*", Applied Physics Letters, **125**, 202601 (2025).

[3] **S. Battisti**, M. Pioldi, A. Paghi, G. De Simoni, A. Braggio, G. Senesi, L. Sorba and F. Giazotto. "*Giant thermal modulation via a semiconductor-superconductor photonic field-effect heat transistor*", arXiv preprint arXiv:2510.17683 (2025).

[4] A. Paghi, **S. Battisti**, S. Tortorella, G. De Simoni and F. Giazotto. "*Cryogenic behavior of high-permittivity gate dielectrics: The impact of atomic layer deposition temperature and the lithographic patterning method*", Journal of Applied Physics, **137**, 044103 (2025).

[5] A. Paghi, L. Borgongino, **S. Battisti**, S. Tortorella, G. Trupiano, G. De Simoni, E. Strambini, L. Sorba and F. Giazotto. "*Josephson Field Effect Transistors with InAs on Insulator and High Permittivity Gate Dielectrics*", ACS Applied Electronic Materials **7**, 3756-3764 (2025).

[6] **S. Battisti**, J. Koch, A. Paghi, L. Ruf, A. Gulian, S. Teknowijoyo, C. Cirillo, Z. Makhdoumi Kakhaki, C. Attanasio, E. Scheer, A. Di Bernardo, G. De Simoni and F. Giazotto. "*Demonstration of high-impedance superconducting NbRe Dayem bridges*", Applied Physics Letters, **124**, 172601 (2024).

[7] J. Koch, C. Cirillo, **S. Battisti**, L Ruf, Z Makhdoumi Kakhaki, A. Paghi, A. Gulian, S. Teknowijoyo, G. De Simoni, F. Giazotto, C. Attanasio, E. Scheer and A. Di Bernardo. "*Gate-controlled supercurrent effect in dry-etched Dayem bridges of non-centrosymmetric niobium rhenium*" Nano Research **17**, 6575-6581 (2024).

[8] F. Antola, **S. Battisti**, A. Braggio, F. Giazotto and G. De Simoni. "*Streamline controlled rectification of supercurrent in thin-film asymmetric weak links*". ArXiv preprint arXiv:2507.12280 (2025).

Contents

Acknowledgements iii

List of Publications v

1 Introduction 1

2 Theoretical background 5
2.1 Fundamentals of BCS theory 5
2.2 Weak-links 8
2.2.1 SIS junction 9
2.2.2 SNS junction 11
2.2.3 Short junction 13
2.2.4 Long junction 14
2.3 Superconductive bipolar thermoelectricity 15
2.4 Sequential tunneling and Coulomb blockade 17
2.5 Heat relaxation in mesoscopic circuits 23
2.5.1 Energy balance 26
2.6 Photonic heat transport 27
2.6.1 Theoretical circuital approach 27

3 Experimental methods 31
3.1 Nanofabrication techniques 31
3.1.1 Wet etching 36
3.2 Low temperature measurement setup 37

3.2.1 Switching current measurements 40

4 Bipolar thermoelectric single-electron transistor 41
4.1 Theoretical model 42
4.1.1 Strong violation of detail balance 43
4.1.2 Sufficient conditions for the strong violation of the detailed balance 44
4.1.3 Quasiparticle current 48
4.2 Results 49
4.2.1 Coulomb diamonds 49
4.2.2 Thermoelectric figures of merit 53
4.3 Differences with the conventional thermoelectricity in quantum dots 55
4.4 Robustness of the effect 57

5 e-ph coupling in InAs on insulator (InAsOI) 59
5.1 Aim of the work 59
5.2 Device layout 60
5.3 Thermometers calibration 61
5.3.1 Behavior of the thermometers in a magnetic field and temperature sensitivity 64
5.4 Energy relaxation experiment 65
5.4.1 Phenomenological model 65
5.4.2 Experimental results 67
5.5 Comparison with other commonly used materials . . 68
5.6 Further considerations on the model 70
5.7 Final consideration on InAsOI 71

6 Photonic heat transport 73
6.1 Photonic heat transport 73
6.1.1 Brief state of the art 73
6.1.2 What can we improve? 74
6.2 Field effect control of photonic heat transport: building blocks 76

6.2.1 Gate dielectric characterization and planar capacitors . . . 77
6.2.2 Tunable impedance: JoFETs with InAsOI . . 79

7 Field effect tunable photonic heat transfer 83
7.1 Explanation of the experiment . . . 83
7.2 Device and experimental setup . . . 86
7.3 JoFET characterization . . . 90
7.3.1 Operation regimes . . . 92
7.4 Thermometry . . . 94
7.5 Experimental results . . . 96
7.5.1 Photonic heat transfer manipulation . . . 96
7.5.2 Influence of bath temperature . . . 99
7.6 Final considerations . . . 102

8 Conclusions and future perspectives 105

A Auxiliary JoFET characterization 109

B T^*_{bath} calculation 111

C Electron-phonon coupling measurements 113

Bibliography 115

Chapter 1

Introduction

In recent decades, the scientific results of superconducting electronics have been remarkable. Observation of complex quantum phenomena, such as quantum coherence or manipulation of electronic quantum states, is nowadays commonplace. The thermal counterpart of superconductive electronics is the field of *coherent caloritronics*, which is used to control and manage heat transfer in superconducting circuits. Micro- and nano-structured superconductors are excellent laboratories for investigating and implementing low-temperature thermal manipulation architectures, primarily due to their unique density-of-states and coherence properties. Although this topic has been extensively studied in recent decades and several experimental and theoretical results have been achieved, flexible, scalable architectures for thermal transport management systems and reliable platforms for thermal energy manipulation remain missing. The lack of practical implementation of coherent caloritronic devices is primarily due to the need to utilize magnetic fields in all proposed architectures. This makes the devices less scalable and more complex, as is usually the case with magnetic fields.
The purpose of our work is to pave the way for a real and scalable implementation of caloritronic architectures that leverage *electrical fields*. In fact, given the experience with CMOS transistors, it is evident that electrical fields are easier to generate and more scalable than magnetic fields, which require uncomfortable coils or flux

lines. The fundamental structure used throughout this thesis is the *top-gate* architecture, consisting of a metallic electrode separated from the portion of the device where we want to apply the electric field by an insulating layer.
This thesis consists of two main results: the first one refers to the generation of *thermoelectricity* with superconductors and its manipulation with the application of a gate potential; the second one refers to the *photonic heat transfer* due to electron-photon coupling in superconducting circuits, which we will show can be manipulated via a top gate. Both of these results had already been achieved using magnetic fields, rendering the proposed devices practically useless for real applications. We will show that to reach our results, we had to find new solutions and implement novel ideas to make the structures suitable for gate tuning.

The thesis is organized as follows.

Chapter 2 is a theoretical introduction and background of all the phenomena, which will serve for the analysis of the experimental results. We will start with the basics of the BCS theory of superconductors, then show the main properties of the weak links we will encounter. We will then provide details of the phenomena that will be crucial to the thesis's results, including superconducting bipolar thermoelectricity, sequential tunneling and Coulomb blockade, heat relaxation in mesoscopic circuits, and photonic heat transport.

Chapter 3 focuses on the practical details about the micro- and nano-fabrication of the devices and the experimental details of the measurement setups used for collecting the data shown.

Chapter 4 is a theoretical work on the possibility of allowing electrical tuning of superconductive bipolar thermoelectricity with a single electron transistor. We will present the theoretical model as a mean-field interpretation of bipolar thermoelectricity. We will then display the numerical results and differences with conventional thermoelectricity in quantum dots.

Chapter 5 provides the basics for the results in subsequent chapters, demonstrating the attractive thermal properties of InAs-on-Insulator, a novel semiconductor platform. We will present the experiment on electron-phonon coupling in InAs-on-Insulator and a theoretical model to interpret the results. Of particular interest will also be the comparison with other commonly used materials in caloritronics.

Chapter 6 explores the photonic heat transport field, with a brief state of the art and some considerations on what can be improved in the field. Moreover, we will discuss the characterisation of the building blocks (inductors and capacitors) of the superconducting photonic circuit, which we will use in the subsequent chapter.

Chapter 7 gives the final and most important results of this thesis on the electrostatic manipulation of photonic heat transfer. We will explain the experiment in detail and then provide the experimental results. We will show that InAs-on-Insulator yields results that are notably better than those reported in the literature. The experimental data will also be interpreted with the theoretical model shown in Chapter 1. Finally, we will consider these results and their potential impact on the field of caloritronics.

Chapter 8 concludes this thesis, offering final considerations on the results achieved and outlining future perspectives for gate-tunable caloritronics.

Chapter 2

Theoretical background

2.1 Fundamentals of BCS theory

The Bardeen-Cooper-Schrieffer (BCS) theory [9], formulated in 1957, provides the first successful microscopic explanation for conventional superconductivity. It describes superconductivity as a macroscopic quantum phenomenon in which two electrons in the Fermi sphere with opposite momenta and spins can form a singlet bound state called a Cooper pair (CP). This phenomenon is mediated by an attractive potential u that arises from a weak attractive interaction between electrons and lattice phonons [10]. Since this interaction between electrons is attractive, the Fermi sphere becomes unstable, and electrons (now Cooper pairs) can condense into a lower-energy ground state. Since CPs are bosons, the ground state of BCS theory is the same for all CPs. It can be described by a unique complex wavefunction $\psi \propto \Delta e^{\varphi_S}$, where Δ is the superconducting energy gap and φ_S is the phase of the ground state (a Bose-Einstein condensate). The energy gap $\Delta(T)$ is a function of temperature and has to vanish for $T > T_c$, where T_c is the critical temperature at which the superconductive-normal metal transition occurs. This energy gap indicates the separation in energy between the CPs and the non-condensed electrons, which we will call quasiparticles because of their excitation nature over the ground state condensate of CPs.

The fundamental equation that the BCS theory was able to predict

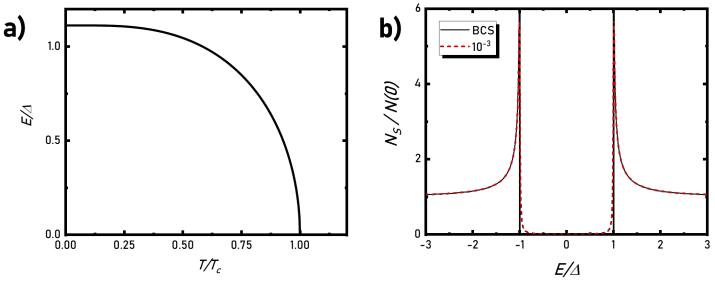


Figure 2.1: **(a)**: Calculated superconductive gap $\Delta(T)$ as a function of temperature. **(b)**: Calculated superconductive DOS as a function of energy. The solid line represents the BCS formula in Eq. 2.4 while the red dashed line includes the parameter $\gamma_D = 10^{-4}\Delta_0$ as in Eq. 2.5.

describes how $\Delta(T)$ varies with the pairing potential u [10]:

$$\frac{1}{N(0)u} = \int_{-\hbar\omega_D}^{\hbar\omega_D} \frac{d\epsilon}{\sqrt{\epsilon^2 + \Delta(T)^2}} \tanh\left(\frac{\sqrt{\epsilon^2 + \Delta(T)^2}}{2k_B T}\right), \tag{2.1}$$

where $\hbar$ is the reduced Planck constant, $N(0)$ is the electronic density of states (DOS) at the Fermi level at 0 temperature, ω_D is the Debye frequency, and k_B is the Boltzmann constant. Solving this self-consistent equation gives the value of $\Delta(T)$ for a specific material (u and ω_D are material-dependent quantities). A handy approximation for Eq. 2.1 to find $\Delta(T)$ can be found in [10] and will be used for future calculations in this thesis:

$$\Delta(T) \simeq \Delta_0 \tanh\left[1.74\sqrt{\left(\frac{T_c}{T}\right) - 1}\right], \tag{2.2}$$

Where Δ_0 is the value of $\Delta(T)$ for $T = 0$. The behavior of Eq. 2.2 can be observed in Fig. 2.1 (a). For elemental superconductors (i.e. Al, Pb, V, etc), the weak coupling approximation holds $N(0)u \ll 1$, and after some algebra, one can find the following

$$\Delta_0 = 1.764 k_B T_c. \tag{2.3}$$

Another crucial feature of superconductors that we will extensively use is their DOS. The energy of a quasiparticle not condensed in the ground state of BCS, with respect to the ground state, is $E = \sqrt{\epsilon^2 + \Delta(T)^2}$ where ϵ is the energy of a free electron in a conduction band of a normal metal with respect to the Fermi energy E_F. Considering the complete symmetry that exists between the quasiparticles with respect to the ground state of the BCS and the electrons with respect to the Fermi energy, one can equate $dEN_{BCS}(E) = d\epsilon N_N(\epsilon)$ where $N_{S,N}$ are the DOSs of the superconductor and the normal metal, respectively. Now, if we consider that for elemental superconductors $\Delta_0 \ll E_F$ we can neglect the weak dependence of $N_N(\epsilon)$ on ϵ and substitute $N_N(\epsilon) \simeq N(0)$, we find:

$$\frac{N_{BCS}(E,T)}{N(0)} = \frac{d\epsilon}{dE} = \frac{E}{\sqrt{E^2 - \Delta(T)^2}}\Theta(E^2 - \Delta(T)^2), \tag{2.4}$$

where Θ is the Heaviside function. It is worth noting that the DOS is 0 for $|E| < \Delta$, which means that the formation of a superconductive gap suppresses exponentially quasiparticle excitations having that energy range. Moreover, it is worth noting that the BCS DOS exhibits a divergence at $|E| = \Delta$. This kind of divergence can be smeared with the introduction of a phenomenological parameter γ_D [11]:

$$\frac{N_{BCS}(E,T)}{N(0)} = Re\left|\frac{E - i\gamma_D}{\sqrt{(E - i\gamma_D)^2 - \Delta(T)^2}}\right|. \tag{2.5}$$

The difference between smeared and non-smeared BCS DOS can be observed in Fig. 2.1 (b). This parameter γ_D takes into account physical processes that can make sub-gap energy states available for single electrons (quasiparticles), for example, phonon-assisted quasiparticle recombination [11]. In the following studies, we will make use of Eq. 2.5 when referring to the DOS of a superconductor, with values of $\gamma_D \sim 10^{-4}\Delta_0$.

To conclude this section, we present the key superconducting parameters for aluminum thin films, since it will be the only superconductor used throughout this thesis. Al has a superconductive gap Δ_0 that ranges from 160 μeV (bulk case [10]) to 230 μeV (for thin films [8]), and a consequent critical temperature T_c that is in the range $1.2 - 1.6$ K, depending on the film thickness.

2.2 Weak-links

In the broadest sense, superconductive weak links are those regions in space where superconductive circuits have *weaker* superconductivity. To be more specific, the latter sentence means that a weak link is a portion of a superconductor where, somehow, the critical current is reduced with respect to the neighboring regions. Usually, this feature is reached when two large superconductive leads are speared by a non-superconductive material or a much weaker superconductor, forming what we will call a *junction*. For example, a weak link can form with an insulating barrier, a normal metal, a semiconductor, a geometrical constriction, or even a ferromagnet. In this thesis, we will be interested in two types of weak-links, the superconductor-insulator-superconductor (SIS) junction and the superconductor-normal metal-superconductor (SNS) junction, whose details will be given in the next two sections.
The most important property of a weak-link is its current-phase relation (CPR), which is the functional that correlates the supercurrent flowing through a weak-link ($I(\varphi)$) with the phase difference across the structure (φ) [10, 12]. This function must satisfy the following conditions independently of its specific composition:

- **Periodicity** Since a rotation 2π of the phase of a superconductor does not change the quantum state of the condensate, the CPR must satisfy $I(\varphi) = I(\varphi + 2\pi)$
- **Time reversal symmetry** Since the time reversal symmetry holds (apart from systems which violate the time reversal

symmetry such as strong spin orbit coupling, ferromagnets, not treated in this work), a change in the current sign must be matched with a change in the phase sign, and hence the CPR has an odd dependence on the phase $I(-\varphi) = -I(\varphi)$

The combination of the two above properties also tells us that $I(n\pi) = 0$, where n is an integer. All these properties together can be summarized in a Fourier series, which tells us that

$$I(\varphi) = \sum_k I_k \sin(k\varphi), \tag{2.6}$$

which is the most general CPR for a weak-link that satisfies the above properties. Another general property of weak-links introduced by Josephson in 1962 [13] is the evolution of the voltage across the junction

$$V = \frac{\hbar}{2e}\frac{\partial\varphi}{\partial t}. \tag{2.7}$$

This property is even more general than the CPR in Eq. 2.6, which could depend on the specific features of the weak-link, and always applies to weak links. This property is useful to carry out one more relation, which will be useful in the following paragraphs, which relates the free energy $E(\varphi)$ of the weak-link to the phase. This relation can be obtained by the integration over time of the power generated by a weak-link:

$$E(\varphi) = \int IV dt = \frac{\hbar}{2e}\int I(\varphi)d\varphi \quad \Rightarrow \quad I(\varphi) = \frac{2e}{\hbar}\frac{\partial E(\varphi)}{\partial\varphi}. \tag{2.8}$$

From now on, since we will treat weak-links where Josephson physics applies, we will refer to the weak-links as *Josephson junctions* (JJs).

2.2.1 SIS junction

Josephson first studied the SIS junctions in 1962 [13], and he published the key prediction that two superconductors separated by a

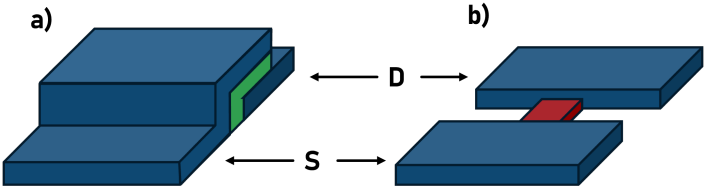


Figure 2.2: Schematics of the two types of junctions studied in this work. **(a)**: an SIS junction with blue superconductive electrodes and a green insulating barrier. **(b)**: an SNS junction with blue superconductive electrodes and in red the normal metal (or doped semiconductor). The source (S) and drain (D) electrodes are indicated for clarity.

tunnel barrier could support a supercurrent due to CP tunneling, with CPR and phase evolution:

$$\begin{aligned} I(\varphi) &= I_c \sin(\varphi), \\ \frac{\partial \varphi}{\partial t} &= \frac{2eV}{\hbar}, \end{aligned} \tag{2.9}$$

where I_c is the maximum supercurrent that the JJ can support in the non-dissipative state (this parameter will strongly depend on temperature, as we shall see). As already said, the second equation in Eq. 2.9 is very general and it applies to most weak links, while the purely sinusoidal CPR is a limit in the case of weak coupling of the more general case in Eq. 2.8 as we will see in the next section. The rules above for SIS tunnel junctions apply to CP tunneling, but this regime applies only when the resistance of the tunnel barrier R_T is low enough to make the Josephson energy $E_J = \hbar I_c/(2e) \propto 1/R_T$ (this will be clear in the next section) much higher than the typical thermal fluctuation energy $k_B T$. On the other hand, if the tunnel resistance is high enough to realize the condition $E_J \ll k_B T$, the Josephson effect will be negligible for a SIS junction and the main electronic transport channel will be due to *quasiparticle tunneling*[1].

[1]We note that in the case of SIS tunnel junctions, normal electronic conduction is considered forbidden due to the insulating nature.

To treat this phenomenon, we consider biasing the SIS junction in Fig. 2.2 (a) with an external voltage V, hence the two electrodes of the junction will be at different electrochemical potentials μ, namely for the S electrode $\mu_S = +eV/2$ and for the drain electrode $\mu_D = -eV/2$ (with respect to the Fermi energy). The general expression for the quasiparticle current, considering only single-electron tunneling, will be given at the first order perturbation theory by the Fermi golden rule [14]:

$$I_{qp} = \frac{1}{eR_T}\int_{-\infty}^{+\infty} dE N_D[1 - f_S D(E-\mu_D, T_D)]N_S f_S(E+\mu_S, T_S), \tag{2.10}$$

where in our case for SIS $N_{S,D} = N_{BCS}$ and $f_{S,D} = \frac{1}{\exp[(E-\mu_{S,D})/k_B T_{S,D}]+1}$ are the Fermi-Dirac equilibrium distributions at two different temperatures $T_{S,D}$. We note that Eq. 2.10 has to be considered valid only in *equilibrium* or *quasi-equilibrium* (stationary conditions) regime, so that the distributions of electrons in the leads can be described by Fermi-Dirac statistics. Moreover, we have to point out that we will neglect any superior perturbative order when considering quasiparticle transport through SIS structures, such as electron cotunneling.

2.2.2 SNS junction

The modern approach to treating JJs and, more generally, weak links is through Andreev bound states (ABS). This kind of state emerges from the Andreev reflection process at the interface between a normal metal and a superconductor, as depicted in Fig. 2.3.

An electron e^- is reflected as a hole h^+ with opposite quantum numbers (spin, momentum, and energy with respect to E_F) and a CP is transferred to the superconductor. This process leads to the formation of spatially localized electron-hole states, which allow a CP to pass through the SNS junction in Fig. 2.2 (b), in the form of a counter-propagating electron-hole pair [12, 15]. Since in principle many transport channels could be available, we will have n transport

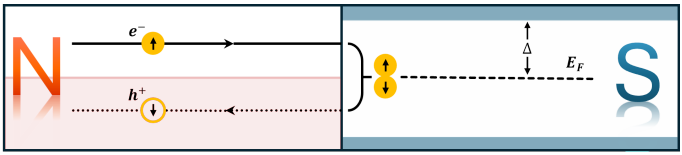


Figure 2.3: Schematics of an Andreev reflection process at the interface between a normal metal and a superconductor.

channels, and each of them will have a pair of states with opposite energy $E_n^{\pm}$ with respect to E_F due to electron-hole symmetry. We can rewrite Eq. 2.8 with the introduction of ABS:

$$I(\varphi) = \frac{2e}{\hbar} \sum_n f(E_n^{\pm}) \frac{\partial E_n^{\pm}(\varphi)}{\partial \varphi}, \tag{2.11}$$

where $f(E_n^{\pm})$ is the equilibrium Fermi-Dirac distribution.
The CPR due to ABS in an SNS junction can be influenced by several factors, such as the intrinsic material properties of the normal metal, the geometry, the quality of the contacts between the superconductor and the normal metal, and also external fields. We will give some insight into two interesting regimes which will be useful during the discussions in this thesis: the *short-* and *long-junction* regimes. However, before starting the discussion of these two regimes, we have to explain what *short* or *long* junction means in terms of the relevant energy scales in SNS systems. The two most important energy scales are the superconducting gap of the leads Δ and the Thouless energy E_{Th}, which is an energy scale related to the inverse of the time it takes for an electron to pass through the junction. E_{Th} has two different forms depending on the type of transport in the N-part of the junction: for ballistic transport $E_{Th} = \hbar v_F / L$ where v_F is the Fermi velocity and L is the length of the junction, and for diffusive transport $E_{Th} = \sqrt{\hbar D / L^2}$, where $D = v_F l_e / d$ is the diffusion coefficient, l_e is the electron mean free path of the N-part of

the junction and d is the dimensionality of the transport. The ratio between Δ and E_{Th} determines whether a SNS junction is in a short or long regime. If $\Delta/E_{Th} \ll 1$ we are in the short junction regime, conversely, for $\Delta/E_{Th} \gg 1$ we are in the long junction regime. Those inequalities can also be rearranged in length terms, which is maybe clearer, considering the coherence length $\xi = \hbar v_F/\Delta$ for ballistic transport and $\xi = \sqrt{\hbar D/\Delta}$ for diffusive transport. The coherence length is the scale that determines the typical spatial extension of a CP; the stronger the superconductive pairing potential, the smaller the CP. Finally, we can rewrite the above inequalities, such as $L \ll \xi$ for the short junction and $L \gg \xi$ for the long junction.

2.2.3 Short junction

To extract the relevant formulas for the short-junction limit, we must start from the spectrum of Andreev states. For $L \ll \xi$ those states have a known dispersion in the literature [16] $E_n^{\pm}(\varphi) = \pm\Delta\sqrt{1 - \tau_n \sin^2(\varphi/2)}$, where τ_n is the transmission probability coefficient for the n-*th* channel. Using the Fermi-Dirac equilibrium distribution for $f(E_n^{\pm})$ one obtains

$$\frac{e\Delta^2}{2\hbar} \sum_n \frac{\tau_n \sin(\varphi)}{E_n(\varphi)} \tanh\left[\frac{E_n(\varphi)}{2k_B T}\right]. \tag{2.12}$$

It is useful to study some limits of Eq. 2.12:

- *Perfect transparency, ballistic transport* $\tau_n = 1$. For a one-dimensional short junction in the ballistic transport regime ($L \ll l_e \ll \xi$) with $\tau_n = 1$ we can rewrite Eq. 2.12 in the Kulik-Omelyianchuk (KO-2) formula [12]

$$I(\varphi) = \frac{Ne\Delta}{\hbar} \sin(\varphi/2) \tanh\left[\frac{\Delta \cos(\varphi/2)}{2k_B T}\right]. \tag{2.13}$$

- *Diffusive regime*. For a one-dimensional diffusive short junction ($l_e \sim L \ll \xi$), the treatment is more complicated, involving the

use of Usadel equations. Following the results of Kulik and Omelyanchuk in [17] for CPR, we find

$$I(\varphi) = \frac{4\pi k_B T}{eR_S} \sum_{n=0}^{\infty} \frac{\Delta \cos(\varphi/2)}{\delta} \arctan\left[\frac{\Delta \sin(\varphi/2)}{\delta}\right], \quad (2.14)$$

where $\delta = \sqrt{\Delta^2 \cos^2(\varphi/2) + \omega^2}$ and $\omega = \pi k_B T(2n+1)$ are the Matsubara frequencies, and $R_S^{-1} = e^2 k_F^2 A/(4\pi^2\hbar)$ is the Sharvin resistance of the N-part of the junction, with k_F the Fermi wavevector and A the transpersal area of the weak-link.

- *Tunnel regime* $\tau_n \ll 1$. In this regime, it is straightforward to exploit the limit for $\tau_n \ll 1$ in Eq. 2.12 to extract

$$I(\varphi) = I_c \sin(\varphi), \quad (2.15)$$

where $I_c = \frac{e\Delta\tau}{2} \tanh \frac{\Delta}{2k_B T}$ is the Ambegaokar-Baratoff formula for the critical current $I_0(T)$. From Eq. 2.15 we can see that the Josephson prediction for tunnel junctions is also recovered in the ABS framework.

2.2.4 Long junction

The long-junction regime is valid for $L \gg \xi$ and is more complicated to treat because the ABS phase evolves during its travel time through the junction. The number of transport channels increases with the length of the junction in both the ballistic and diffusive regimes. Here we will cite only the behavior of the critical current $I_c(T)$ for $k_B T > 5E_{Th}$ whose solution is well known [18]:

$$I_c(T) = \frac{64\pi k_B T}{eR_N} \sum_{n=0}^{\infty} \frac{\sqrt{\frac{2\omega}{E_{Th}}}\Delta^2(T) \exp[-\sqrt{\frac{2\omega}{E_{Th}}}]}{[\omega + \delta + \sqrt{2(\delta^2 + \omega\delta)}]^2}, \quad (2.16)$$

where δ and ω are the Matsubara frequencies. The result in Eq. 2.16 will be useful for the SNS thermometry in the chapter 5.

2.3 Superconductive bipolar thermoelectricity

In this section, we will introduce a topic of interest of this thesis, which is *bipolar thermoelectricity*, a novel phenomenon that arises from thermally biased SIS' structures. We will explain the difference between bipolar thermoelectricity and "conventional" linear thermoelectricity and give an insight into how this effect arises.

When considering the linear regime in temperature gradients, conventional thermoelectricity requires breaking of the electron-hole (EH) symmetry at the scattering level, implying a non-reciprocal IV characteristic, i.e., $I(V, \Delta T) \neq -I(-V, \Delta T)$, where ΔT is the temperature difference. For this reason, metals that are almost spectrally EH symmetric show nearly negligible Seebeck coefficients [19] and present zero thermovoltages in the superconducting phase, which is by definition EH symmetric (see Eq. 2.4). However, in the non-linear temperature regime, it has been demonstrated both theoretically and experimentally [20–22], that an *SIS'* thermally-biased superconducting tunnel junction, when the Josephson coupling is sufficiently suppressed, spontaneously develops a voltage bias: a manifestation of spontaneous breaking of the EH symmetry of the *whole junction*. The system exhibits significant thermopower, producing an effective Seebeck coefficient ($\mathcal{S}$) as large as $\sim 10^5$ times its value in the normal state [22, 23]. Crucially, the spectral EH symmetry of each of the leads of the structure determines a full *bipolar* effect, i.e., reciprocal IV characteristics. We will call this effect *bipolar thermoelectricity*. Notably, the effect emerges in *SIS'* structures when the temperature difference is of the order of the gaps and it non-linearly depends on the gaps asymmetry. Moreover, two different energy-gap superconductors are required for the manifestation of this effect.
For the sake of clarity, we must say that when we refer to an EH spontaneous symmetry breaking of the whole system, we refer to a specific configuration of DOS, gaps, and thermal biases, and not to

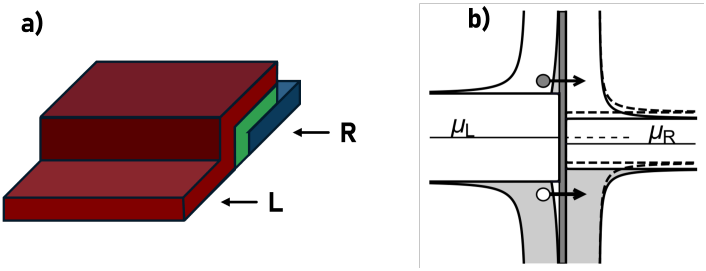


FIGURE 2.4: **(a)**: Example of a thermally biased SIS' structure with the hot left electrode L and the cold right electrode R. **(b)**: The combination of the gap in the hot electrode (left) and the monotonically decreasing DOS above the gap of the cold electrode (right) produces a particle current which flows in the opposite direction of the chemical potential gradient.

the altered DOS of a single superconducting contact with respect to the Fermi energy. Looking at Fig. 2.4 (a), we can see the configuration of the SIS' structure that we want to investigate, with a hot left electrode (in red) and a cold right electrode (in blue). In addition, the left electrode has a larger superconducting energy gap, $\Delta_L > \Delta_R$. What we mean by spontaneous symmetry breaking of the EH is that the DOSs profile of the *whole* junction is altered by the voltage generated inside the junction itself, as can be seen in Fig. 2.4 (b). When the temperature difference between the leads is sufficiently large (on the order of the gaps $k_B T \simeq \Delta_{L,R}$ but still in the superconducting regime), if we think of a positive voltage fluctuation across the thermally biased structure, the DOS shift in the way depicted in Fig. 2.4 (b), and hence holes in the left lead will find a higher DOS on the right lead, resulting in a higher tunneling rate of quasiparticles. This generates a current of opposite sign to the bias, and as a result, the bias is further increased (absolute negative conductance). This is due to the monotonically decreasing DOS for both positive and negative energies. This mechanism resembles what happens in other spontaneous broken-symmetry phenomena, where, at criticality, symmetry breaking emerges even from a small

fluctuation.
As discussed in chapter 4, assuming a fully particle-hole symmetric DOSs in the leads taken separately, the sufficient condition for the mentioned mechanism is a monotonic decreasing DOSs that rigidly shifts with the electrochemical potential (see again Fig. 2.4). The usual shape of the superconducting DOSs ensures the former property. At the same time, the latter is guaranteed by the interacting nature of superconductors, which is fully captured by the BCS theory (which, in the end, is a mean-field theory). Indeed, in chapter 4 we will clearly show that the role of interactions is a necessary condition for spontaneous EH symmetry breaking. This is fully revealed by investigating the quasiparticle tunneling rates and observing the "*strong detail balance violation*", as discussed in section 4.1.1.

2.4 Sequential tunneling and Coulomb blockade

In this section, we will provide basic information on two low-energy phenomena that may occur in the presence of a tunnel junction (either superconductive or metallic). Consider now a simple metal-insulator-metal junction, where an electron can pass from one side to the other. The resulting voltage change in the junction is $\Delta V \simeq e/C$ with C being the capacitance of the junction. For a junction of $100\mu\text{m}^2$, this value is $\Delta V \simeq 10^{-9}\text{V}$. Since at room temperature the voltage fluctuations due to thermal excitation are of the order $\Delta V_T \simeq k_B T/e \simeq 10^{-2}\text{V}$, any effect related to single electron tunneling is absolutely covered by thermal fluctuations. However, if the tunnel junction gets small enough and the temperature gets low enough to reach a regime where

$$E_C \equiv \frac{e^2}{2C} \gg k_B T, \tag{2.17}$$

Single-electron effects can play a crucial role in the physics of a tunnel junction. In addition, we must also have a very low tunnel

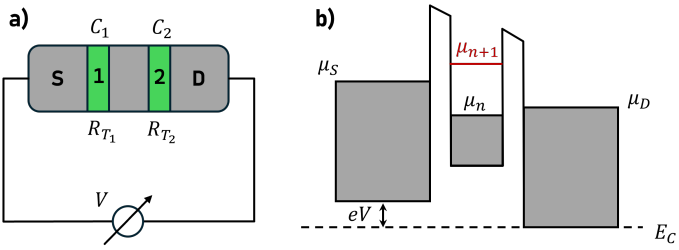


FIGURE 2.5: **(a)**: Circuital scheme of the type of structure studied. The central metallic island is separated from the source (S) and drain (D) electrodes by two tunnel barriers with resistances R_{T_i} and capacitances C_i. A bias voltage V is applied to the whole structure. **(b)**: Energy scheme of a Coulomb blockade configuration. The central island has the last occupied state at electro-chemical potential μ_n and the first free state at μ_{n+1}. The energetic configuration of the S and D electrodes does not allow electron tunneling (at least at first order). To pass into the regime of *single electron tunneling*, the source potential has to be increased.

conductance $G_T = 1/R_T$ with respect to the conductance quantum $G_0 = 2e^2/h$, so $R_T \gg h/2e^2$. This last condition, together with Eq. 2.17 states that the charging energy of an electron tunneling is much bigger than both the thermal fluctuation energy scale and the quantum fluctuation energy scale $\sim \hbar/\tau_T$ where $\tau_T \equiv C/G_T$. This regime is usually called *sequential tunneling*, which means that the tunneling of electrons through tunnel barriers cannot occur massively for a large number of electrons (usual resistive transport), but each tunneling of electrons produces a crucial effect on the whole system. In addition, we will also neglect the Josephson effects in the presence of superconductors since we will always be in the condition $E_J \propto 1/R_T \ll k_B T$, hence avoiding any effect of CP tunneling.

To understand the importance of charging phenomena and sequential tunneling, in Fig. 2.5 (a) we depicted the typical system which we will study in the sequential tunneling regime, the so called *single electron transistor* (SET): a voltage biased metallic island connected via two insulating barriers to a source (S) and drain (D) electrodes. In Fig. 2.5 (b), a situation that can occur under the conditions

explained above is shown, where the electrochemical potential μ_S of the source electrode is between the last electronic occupied state of the island μ_n and the first free electronic state μ_{n+1}. In this case, transport through the structure is blocked, and we refer to this regime as the *Coulomb blockade*. If we raise the Source potential in a way that it becomes higher than μ_{n+1}, we move onto the sequential tunneling regime, where *one* electron at a time can tunnel through the structure. Equivalently, suppose that the island is equipped with a capacitively coupled voltage generator (usually called a "gate voltage"). In that case, the energy levels μ_i of the electrons in the island can be changed by applying a gate voltage to it. In this way, we can reach a configuration where one level μ_i is between μ_S and μ_D and allow tunneling. However, we note that further shifting of the levels of the island causes the system to periodically return to the blockade regime when the island levels configuration is the one depicted in Fig. 2.5 (b) (this phenomenon will become clearer later in this section).
The theoretical treatment of the SET starts by considering the tunneling rates for the possible tunneling processes of electrons in the structure in Fig. 2.5 (a). In the sequential tunneling regime, where $E_C \gg k_B T$ and $G_T \ll G_0$, we can safely neglect the tunneling processes of multiple electrons and focus on single electron tunneling. We have four possible events with associated tunneling rates:

- An electron tunneling forward from the S electrode to the island through barrier 1 $\rightarrow$ we will call this tunneling rate Γ_1^+.
- An electron tunneling backward from the island to the S electrode through the barrier 1 $\rightarrow$ we call this tunneling rate Γ_1^-.
- An electron tunneling forward from the island to the D electrode through the barrier 2 $\rightarrow$ we call this tunneling rate Γ_2^+.
- An electron tunneling backward from the D electrode to the island through the barrier 2 $\rightarrow$ we call this tunneling rate Γ_2^-.

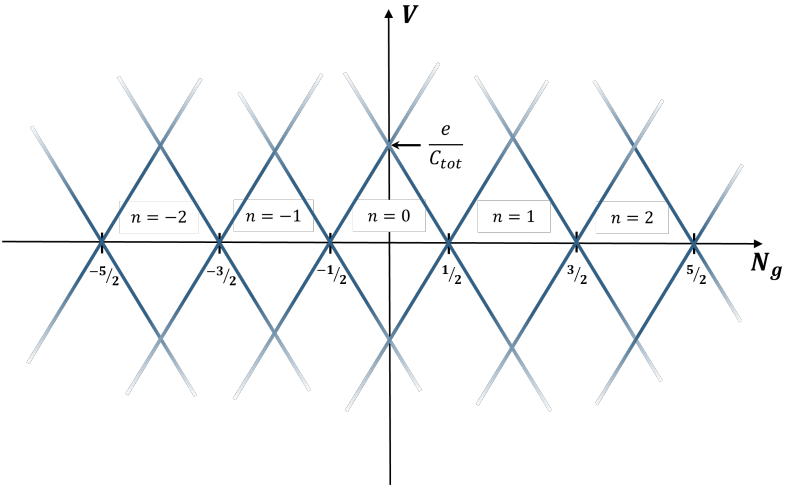


Figure 2.6: Phase diagram of the SET for single-electron tunneling (sequential tunneling regime). The rhomboids covering the N_g-axis represent the Coulomb blockade regime where the tunneling rates $\Gamma^{\pm}_{1,2}$ vanish and the electron transport is prohibited.

The $1, 2$ indices denote the different tunnel barrier, while the $+, -$ sign denotes the forward and backward tunneling, respectively.
Now that we have identified the processes in our structure, we need to calculate the tunnelling rates for each of them. To do this, we start by considering the energy change introduced by each process to our system. For completeness, we also assume that the central island is coupled to an external gate voltage V_g through a capacitance C_g. We obtain for the energy shifts:

$$\begin{aligned} \delta U_1^{\pm} &= \frac{e}{C_{tot}} \left(-\frac{e}{2} \mp (Ne - N_g e) \pm C_1 V \right), \\ \delta U_2^{\pm} &= \frac{e}{C_{tot}} \left(-\frac{e}{2} \pm (Ne - N_g e) \pm C_2 V \right), \end{aligned} \tag{2.18}$$

where $N_g = C_g V_g / e$ represents the offset charge of the island. It is useful to construct a phase diagram of the SET setting $\delta U^{\pm}_{1,2} = 0$.

To simplify the calculation, we set $C_1 = C_2 = C_g = C$, $C_{tot} = C_1 + C_2 + C_g$ and $R_{T_1} = R_{T_2} = R_T$. Figure 2.6 shows the phase diagram of the SET in the N_g-V plane, often also called *Coulomb diamonds* for the rhomboidal structure. The solid blue lines correspond to the equations $\delta U^{\pm}_{1,2} = 0$, while the rhomboids covering the N_g-axis represent the equilibrium condition ($\delta U^{\pm}_1 < 0$ and $\delta U^{\pm}_2 < 0$) of the SET where transport is prohibited. For each of those rhomboids, there exists a value of n that puts the SET in the condition depicted in Fig. 2.5 (b) where transport is prohibited (Coulomb blockade) and all tunneling rates $\Gamma^{\pm}_{1,2}$ disappear (see after) [14].
Tunneling rates $\Gamma^{\pm}_{1,2}$ are calculated in the first perturbative order using the Fermi golden rule [14, 24]:

$$\Gamma^{\pm}_i(\delta U, T_{is}, T_k) = \frac{1}{e^2 R_T} \int_{-\infty}^{+\infty} dE \mathcal{N}_{is}(E + \delta U^{\pm}_i, T_{is})[1 - f_{is}(E + \delta U^{\pm}_i, T_{is})] \times \mathcal{N}_k(E, T_k) f_k(E, T_k), \tag{2.19}$$

where $\mathcal{N}_j(E, T_j)$ are the DOSs in the islands (is), the sources (S) and drains (D) and f_j are the Fermi-Dirac distribution at equilibrium temperature T_j (with $j = is, S, D$) for each electrode. We stress again that this approach is a first perturbative order theory (i.e., we are using the Fermi golden rule), hence disregarding any higher order process like double electron tunneling (cotunneling), which would result in higher perturbative order terms, or CP tunneling (also possible in the case of superconducting structures).
The physical quantity we ultimately wish to extract is the current through the i-barrier, as it is experimentally straightforward to measure the current flowing through the structure as a function of the applied voltage. Following the derivation in [14], we have for the current through the i-th barrier as a function of time:

$$I_i(t) = \sum_{n=-\infty}^{n=\infty} \sigma(n, t)[\Gamma^{+}_i(n) - \Gamma^{-}_i(n)], \tag{2.20}$$

where $\sigma(n,t)$ is the probability that n electrons will be on the island at the time t. Equation 2.20 has an obvious physical meaning: it tells us that the current on the i-th barrier is equal to the probability of having n electrons on the island multiplied by the difference between forward and backward rates and summed over all possible electronic states n of the island. Since the current must be conserved in the SET structure depicted in Fig. 2.5 (a), the current through each barrier will be the same, so that we can compute it only through one of the tunnel barriers. We now miss only an expression for the probability $\sigma(n,t)$. We can write a so-called *master equation* for the probability $\sigma(n,t)$ considering the only four possible tunneling processes that we have in our system:

$$\frac{\partial\sigma(n,t)}{\partial t} = \sum_{i=1,2} \Gamma_i^+(n-1)\sigma(n-1,t) + \Gamma_i^-(n+1)\sigma(n+1,t) - [\Gamma_i^+(n) + \Gamma_i^-(n)]\sigma(n,t). \tag{2.21}$$

Again, the physical meaning of Eq. 2.21 is clear to understand: the evolution of the probability of having n electrons on the island at time t is equal to the probability of having $n-1$ electrons and one electron tunnels on the island ($\Gamma_i^+(n-1)$) plus the probability of having $n+1$ electrons and one tunnels away from the island $\Gamma_i^-(n+1)$, minus the probability of having exactly n electrons and one tunnels on ($\Gamma_i^+(n)$) or out ($\Gamma_i^-(n)$) the island. We will always be interested in the steady state solution of our systems, hence we can drop the t dependence of the above equations and write down an equation for the probability $\sigma(n)$:

$$\sum_{i=1,2} \Gamma_i^+(n-1)\sigma(n-1)+\Gamma_i^-(n+1)\sigma(n+1)-[\Gamma_i^+(n)+\Gamma_i^-(n)]\sigma(n) = 0, \tag{2.22}$$

which can be solved through a standard master equation approach as will be done in chapter 4.

2.5 Heat relaxation in mesoscopic circuits

In this section, we discuss thermal relaxation mechanisms in mesoscopic circuits, as heat transport is the primary focus of this thesis. The usual experimental configuration is depicted in Fig. 2.7. A heat current J_{inj} is injected into an electron gas (drawn in red). It can relax through coupling γ_{e-e} with other electrons or through coupling with lattice phonons (depicted in yellow) γ_{e-ph}, generating the heat current J_{e-ph} towards the lattice phonons. These phonons are coupled via the Kapitza resistance to the bath phonons with the heat current J_K. We note that the electron gas in Fig. 2.7 will always be experimentally realized through a thin layer of n++ InAs, which can effectively be treated as a normal metal for transport properties [2].

Since we will need to define the temperatures within each of these three main subsystems, we need to understand how each subsystem can be in an equilibrium state; otherwise, the thermodynamic definition of temperature has no meaning. If all three reservoirs have the same temperature, the system is considered in *equilibrium* and the temperature can be easily defined; however, this case is not experimentally interesting since we will always inject some heat current J_{inj} to measure different kinds of effects, and this brings the whole system out of equilibrium for sure. Now, let us consider a configuration in which the subsystems have different temperatures and each is in equilibrium because the internal relaxation rates are faster than the external energy injection/relaxation rates. In this configuration, the distribution probability for electrons is described by Fermi-Dirac statistics (or Bose-Einstein for phonons), and the temperature is well defined; we will call this configuration *quasi-equilibrium*. Finally, if each subsystem receives energy faster than it can relax, then the temperatures are not well defined. We will call this configuration *out of equilibrium*. The experimentally relevant configuration is the *quasi-equilibrium* one, and we now discuss how to achieve it with our experimental configurations.

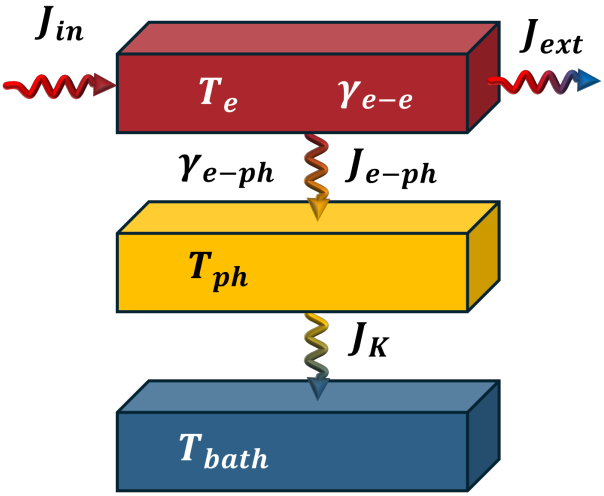


Figure 2.7: Scheme of the relevant thermal subsystems and heat currents considered in this work. In the experimental configuration we inject a heating current J_{inj} inside the electron gas (in red) which relaxes at the rate γ_{e-e} with other electrons and at the rate γ_{e-ph} with the lattice phonons (in yellow) generating the heat current J_{e-ph}. The lattice phonons are coupled via a Kapitza resistance to the bath phonons at temperature T_{bath} with the heat current J_K. To define the temperatures (and the distribution functions) of the different reservoirs, T_e for electrons, T_{ph} for phonons and T_{bath} for bath phonons, we need that each of them is in stationary conditions or *quasiequilibrium*. The direction of the heat currents is valid for the usual experimental configuration $T_e > T_{ph} = T_{bath}$.

First, we consider the Kapitza resistance. This coupling accounts for phonon scattering at the interface between a thin normal-metal film and the substrate. Since the typical phonon wavelength at sub-kelvin temperatures is $\lambda_{ph} = \hbar v_s/(2k_BT) \simeq 200 - 300$nm for GaAs (our most common substrate), and the thicknesses of the normal metal layers are about $80 - 100$nm, we can safely neglect the Kapitza resistance [25] and fix the lattice phonon temperature at bath temperature $T_{ph} = T_{bath}$.
We now have to consider the interaction γ_{e-e} and its ratio with

the injection rate of hot electrons η_{inj}. Typically for normal metals $\gamma_{e-e} \sim 10^9$ [26] at $T_{bath} = 25$mK and scales with temperature such as $\gamma_{e-e} \propto T^2$ for ballistic transport [27] and $\gamma_{e-e} \propto T^{2/3}$ for the quasi-classical diffusive limit [28]. The injection rate of hot electrons can be calculated with the formula $\eta_{inj} = (4e^2 N_0 R_T)$, where N_0 is the DOS at the Fermi level of the heated normal metal and R_T is the resistance between the injection electrode and the normal metal [29]. For our structures $\eta_{inj} \sim 10^5 - 10^6$, we can consider that the electron gas in Fig. 2.7 is in the *quasi-equilibrium* condition.
To finish this section, we have to treat the electron-phonon interaction γ_{e-ph} in Fig. 2.7. This interaction was measured to be $\gamma_{e-ph} \sim 10^5 - 10^6$ at 200mK [30] in Cu films, finally realizing the last condition for the *quasi-equilibrium* regime given above (we will demonstrate in chapter 5 that in our devices made by n-doped InAs, it will be even slower). The temperature behavior depends on the transport regime, $\gamma_{e-ph} \propto T^3$ for clean metals $l_e > \lambda_{ph}$ [27], and $\gamma_{e-ph} \propto T^2 - T^4$ for diffusive metals depending on the nature of the disorder [31].
In chapters 5,7, formulas for the e-ph heat current will be useful. From [32], we find:

$$J_{e-ph} = \Sigma V (T_e^n - T_{bath}^n), \tag{2.23}$$

where Σ is the e-ph coupling constant and n is the exponent of the power law. The usual values for Σ and n for normal metals are $\Sigma \simeq 3 \times 10^9 \mathrm{W}/(\mathrm{m}^3\mathrm{K}^n)$ and $n \sim 5$ [32], however, they are very material-dependent. In chapter 5 we show how these numbers are much different for our n-doped InAs.
For the sake of completeness, we conclude this section with the relations for e-ph coupling in superconductors. Since quasiparticles are exponentially suppressed at $T < T_c$, e-ph coupling in superconductors is much weaker than in normal metals. Moreover, the energy gap between the quasiparticles and the ground state (i.e., the CP condensate) makes the process of two combining quasiparticles with the emission of a phonon at energy 2Δ energetically unfavorable. This leads to an exponential depression of the e-ph coupling rate

$\gamma_{e-ph} \propto T^{1/2} e^{-\Delta/(2K_B T)}$. The heat current due to e-ph coupling in superconductors can be expressed with the formula [33]:

$$J^S_{e-ph} = \frac{\Sigma V}{96\zeta(5)k_B^2} \int_{-\infty}^{\infty} dE E \int_{-\infty}^{\infty} d\varepsilon \varepsilon^2 \mathrm{sgn}(\varepsilon) \mathcal{L}_{E,E+\varepsilon} \times \left[\coth\left(\frac{\varepsilon}{2k_B T_{bath}} \right) \times (f_E - f_{E+\varepsilon}) - f_E f_{E+\varepsilon} + 1 \right], \tag{2.24}$$

where $f_E = f(-E) - f(E)$, $f(E)$ is the Fermi-Dirac distribution for quasiparticles at temperature T_e, and the phonons are assumed to be in thermal equilibrium with the Bose-Einstein distribution at temperature T_{bath}. The term $\mathcal{L}_{E,E+\varepsilon} = N_{BCS}(E, T_e) N_{BCS}(E + \varepsilon, T_e)[1 - \frac{\Delta^2(T_e)}{E(E+\varepsilon)}]$. For temperatures $T < T_c/2$ this interaction produces a very weak heat current with respect to the other heat currents in play and can safely be neglected as we will do in chapters 5,7.

2.5.1 Energy balance

As already said, all the experiments in this thesis are done in the quasi-equilibrium regime. This means that, after a transient, the system has reached *stationary conditions*. From a physical point of view, this means that for a single electrode, the sum of the incoming and outgoing heat currents, with the correct sign, must be 0. Let us take, for example, the red electronic reservoir in Fig. 2.7, the thermal balance equation is:

$$J_{inj} - J_{e-ph} - J_{ext} = 0. \tag{2.25}$$

Here J_{inj} is the incoming power that we supply to the reservoir to raise its temperature, J_{e-ph} is the outgoing e-ph heat current, and J_{ext} summarizes all the energy loss processes not considered in the above section. One of those processes can be electron-photon coupling, an energy-loss channel that can be activated when the heated electrode has good impedance matching with another resistive

electrode. This heat transport channel will be one of the main topics of this thesis.

2.6 Photonic heat transport

The phenomenon of photonic heat transport will be central to this thesis. This phenomenon arises due to the correspondence of Johnson-Nyquist noise and black body radiation when two resistive reservoirs at different temperatures are coupled with an electrical circuit [34–36]. To understand this phenomenon, we start from a theoretical perspective, outlining the rules and formulas that we will extensively use in chapters 6 and 7.

2.6.1 Theoretical circuital approach

The theoretical circuit approach extensively discussed in [36] can be worked out starting from the consideration that in the absence of voltage or current generators, the thermal transport between two generic impedances Z_1 and Z_2 kept at different temperatures $T_{1,2}$ is due to current and voltage fluctuations. Following the analysis in [36] we can decompose the current fluctuation on the *i-th* element in:

$$\Delta I_i = \delta I_i + (\frac{1}{Z_i})\Delta V_i, \tag{2.26}$$

where ΔV_i is the voltage fluctuation in the *i-th* element and δI_i is the current fluctuation due to Johnson-Nyquist noise. This quantity can be further exploited by making use of the fluctuation-dissipation theorem:

$$\langle \delta I_i(\omega)\delta I_i(\omega')\rangle = 2\pi\delta(\omega-\omega')C_i^{(2)}, \tag{2.27}$$

where $\langle ...\rangle$ denotes a thermal average and $C_i^{(2)} = \hbar\omega Re[1/Z_i]\coth(\beta_i\hbar\omega/2)$, where $\beta_i = 1/k_BT_i$ is the inverse temperature of each impedance. We are interested in the power exchanged between the two reservoirs $\dot{Q}_i(t)$, which can be worked out

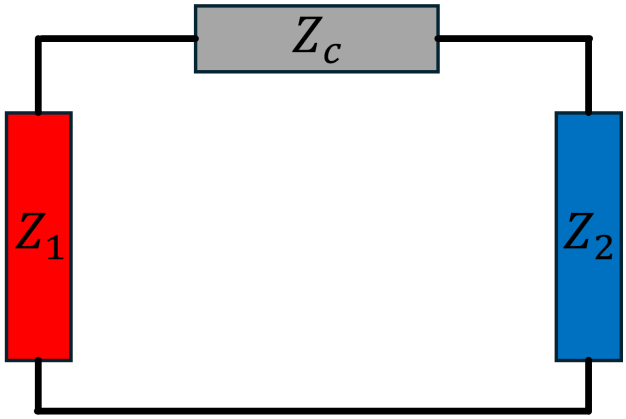


FIGURE 2.8: Two generic impedances Z_1 and Z_2 kept at different temperatures T_1 and T_2 are connected with a superconductive circuit and coupled via a third impedance Z_c.

from the frequency-dependent correlation function $\langle \Delta I(\omega) \Delta V(\omega') \rangle$ by the inverse Fourier transformation:

$$\dot{Q}_i(t) = \int \frac{d\omega}{2\pi} \int \frac{d\omega'}{2\pi} e^{-i\omega t} e^{-i\omega' t} \langle \Delta I(\omega) \Delta V(\omega') \rangle. \tag{2.28}$$

For the case of our interest depicted in Fig. 2.8, considering that Z_c is purely reactive, we can simplify Eq.2.28. Using Eq.2.27, the fact that $\langle \delta I_1 \delta I_2 \rangle = 0$, and the two identities $Z(-\omega) = Z^*(\omega)$ and $\coth(x) = 1 + 2nx$ where $n = (e^x - 1)^{-1}$, we can write:

$$\dot{Q}_1(t) = -\dot{Q}_2(t) = \int_{-\infty}^{\infty} \frac{d\omega}{2\pi} \frac{2\hbar\omega Re[Z_1(\omega)] Re[Z_2(\omega)]}{|Z_{tot}(\omega)|^2} [n_1(\omega) - n_2(\omega)]. \tag{2.29}$$

This expression can be further simplified if we define the photonic thermal transmission coefficient τ

$$\tau(\omega) = \frac{4Re[Z_1(\omega)] Re[Z_2(\omega)]}{|Z_{tot}(\omega)|^2}, \tag{2.30}$$

and we note that the integrand in Eq.2.29 is an even function of ω we can write:

$$\dot{Q}_1(t) = -\dot{Q}_2(t) = \int_{-\infty}^{\infty} \frac{d\omega}{2\pi} \hbar\omega\tau(\omega)[n_1(\omega) - n_2(\omega)]. \tag{2.31}$$

We must note that all these calculations are valid in the lumped element approximation for the circuit in Fig. 2.8, meaning that the electromagnetic waves generated by the fluctuations must have a wavelength $\lambda_\omega \propto 1/\omega$ shorter than the typical dimension of the circuit.

Chapter 3

Experimental methods

In this chapter, we will provide details on the nanofabrication methods and the cryogenic measurement setups that will be used throughout the rest of this thesis.

3.1 Nanofabrication techniques

The samples fabricated in this thesis were made starting from the *heterostructure of InAs on Insulator* (InAsOI), which consists of a 100-nm-thick epitaxial layer of InAs doped with Si n^{++} grown on top of a metamorphic buffer layer of InAlAs, having a graded In concentration to reduce the strain between the GaAs insulating handling substrate and the InAs layer[37, 38].
The fabrication process involved several steps: positive and negative electron-beam lithography (EBL), e-beam and thermal evaporation, wet etching, and ALD growth. We can summarize the complete process in the following steps:

1. Cleaning in ACE and IPA for $5'$ each inside the sonicator, and cleaving of the InAsOI substrate.

2. Verification of the InAsOI cryogenic properties: The InAlAs buffer layer needs to be a cryogenic insulator, which means that below a specific temperature (usually 70K), the buffer

layer becomes an insulator. This test was performed before the start of any fabrication process to avoid using substrates that would introduce undesired leakage currents between the patterned pins.

3. Positive EBL and evaporation to pattern an array of markers, which will be used for future re-alignments of lithographies.

    - Spin coating of a PolyMethylMetacrylate PMMA positive resist (AR-P 679.04) at 4000rpm for $1'$
    - Baking of the resist at 160°C for $1'$
    - Positive EBL with dose $330\mu C/cm^2$ to define the markers at the four edges of the sample
    - Mask developing in MIBK:IPA - 1:3 for 90s
    - Oxygen plasma ashing of the mask at 20W power for $2'$ to avoid PMMA residues after the developing and enhance the adhesion of the evaporated metals.
    - Thermal evaporation of Ti/Au markers with thickness 10/40nm and rates 0.1/0.2nm/s. The Ti serves as a sticker layer to enhance Au adhesion and make the markers as solid as possible.
    - Lift-off of the mask in ACE

4. Patterning of the InAs mesas via negative EBL and wet etching

    - Spin coat of negative resist (AR-n 4340) at 3000rpm for 30s
    - Baking of the resist at 90°C for $1'$
    - Negative EBL aligned with the markers, with dose $130\mu C/cm^2$ to define the InAs mesas. During this EBL, the markers' areas were also exposed to leave a resist patch on them. This was done to prevent the wet etching solution from etching beneath the markers, which would cause them to be removed.

- Developing in MF-319 for $45 - 50$s
- Wet etching in the etching solution $H_2O/C_6H_8O_7/H_2O_2/H_3PO_4$: 21/5/0.5/0.25 vol ($C_6H_8O_7$ 1M, H_2O_2 30% in mass and H_3PO_4 85% in mass, etching rate $\sim$ 50 nm/min). More on the wet etching solution and details in the next subsection
- Resist removal in AR 600.71 at 80°C for $5'$

5. Now we realize a UV-positive lithographic mask only on the marker frame to be able to lift this mask and have clearly visible markers after the passivation and evaporation process.
   - Spin coat of UV positive resist S1805 at 5000rpm for $1'$
   - Baking of the mask at 115°C for $1'$
   - UV positive lithography aligned with the markers, with dose $60\mu J/cm^2$
   - Development of the mask in MF-319
6. InAs surface passivation and consecutive Al evaporation to create a clean Andreev contact.
   - The sample with the etched mesas and the mask on the markers is dipped for 45s into a $(NH_4)_2S_2$ solution that is supersaturated with additional S and heated to 45°C. This solution etches the oxides on the InAs surface and saturates the InAs dangling bonds with S.
   - After a fast DIW rinsing, the sample is inserted inside the vacuum chamber of an e-beam evaporator to avoid the re-oxidation of the surface.
   - Inside ultra-high vacuum S atoms are desorbed from the sample surface, and we have a clean InAs surface where we can deposit by e-beam evaporation 100nm of Al at the rate of 0.2nm/s.

7. Lift-off of the UV mask in ACE to have clear sight on the markers

8. Negative EBL to define the Al contacts on InAs and InAlAs

   - Spin coat of negative resist (AR-n 4340) at 3000rpm for 30s
   - Baking of the resist at 90°C for $1'$
   - Negative EBL aligned using the markers with dose $130\mu C/cm^2$ to define the Al wires and contacts
   - Developing the negative mask in MF-319 for $50 - 60$s
   - Al contacts are finally defined via wet etching inside Al-etchant type-D (Transene company) at 40°C for $\sim$ 30s (this time was very variable).
   - Resist removal in AR 600.71 for $5'$

   Up to this point, we described the full fabrication process for samples without top-gating structures. The next steps are necessary only for top-gate fabrication.

9. ALD growth of 30nm of HfO_2 done in a controlled atmosphere of HfO_2 precursor and water at 130°C for $\sim$ 16h

10. Positive EBL lithography to define the top-gate contacts

    - Spin coating of a PolyMethylMetacrylate PMMA positive resist (AR-P 679.04) at 4000rpm for $1'$
    - Baking of the resist at 160°C for $1'$
    - Positive EBL aligned on the markers with dose $330\mu C/cm^2$ to define the top gates
    - Mask developing in MIBK:IPA - 1:3 for 90s
    - Thermal evaporation of Ti/Au with thickness 10/100nm and rates 0.1/0.2nm/s.
    - Lift-off of the mask in ACE

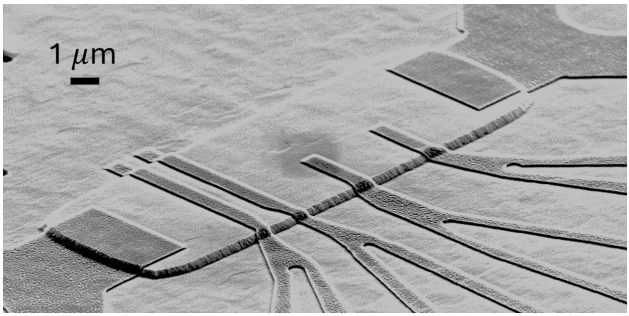


Figure 3.1: Example of a well-contacted InAs mesa. We can see how the Al transmission lines mount over the InAs mesa without interruptions.

At this point, we realised that the Al contacts over the InAlAs were too weak for the wire-bonding process, so we will need to measure the samples. To overcome this issue, we decided to evaporate a *sim*200 nm Ti/Au patch over all the Al bonding pads to make them more resistant to wire bonding.

11. Positive EBL lithography for strengthening the bonding pads[1].

    - Spin coating of a PolyMethylMetacrylate PMMA positive resist (AR-P 679.04) at 4000rpm for $1'$
    - Baking of the resist at 160°C for $1'$
    - Positive EBL aligned on the markers with dose $330\mu C/cm^2$ to define the bonding pads
    - Mask developing in MIBK:IPA - 1:3 for 90s
    - Thermal evaporation of Ti/Au with thickness 10/200nm and rates 0.1/0.2nm/s.
    - Lift-off of the mask in ACE

[1]Independently from the fact that the resolution needed for patterning those bonding pads was safely reachable with an UV lithography, we note that we could not do this step with it because the developer (MF-319) of optical resists is quite a strong etchant for Al.

12. Wire bonding of the sample on a 24-pin DIL chip carrier to measure it in a dilution cryostat

3.1.1 Wet etching

The definition of InAs mesas via wet etching was a crucial step in our fabrication process. What we needed was a wide open obtuse angle formed between our mesas and the rest of the substrate, to have a safe and straightforward way of contacting the InAs mesa with Al, as we can see in Fig. 3.1. Unfortunately, this property was not easy to reproduce, and several tests had to be performed.
The first solution tested was made by $H_2O/H_2O_2/H_3PO_4$: 20/1/1 vol (H_2O_2 30% in mass and H_3PO_4 85% in mass, etching rate $\sim$ 100 nm/min). We found that etching the InAs with an Al layer already on top produced acute mesa angles, as shown in Fig. 3.2. So we tried etching the InAs mesas before Al deposition, as explained in the above section. This partially solved the issue, but the angles were still not as comfortable.

Here, the problem concerns the contacts that will be evaporated after defining this mesa. This mesa edge shape is not compatible with standard perpendicular evaporation, so we will need to complicate the process by adding two tilted evaporation steps (one for each mesa side). This would also imply that we should find a way to determine the sample's direction with certainty, and would force all the mesas to be in the same direction. It is clear that finding the way to have an open angle is the right path to have a nice and safe fabrication process.

The issue was solved completely by adding citric acid ($C_6H_8O_7$) within the etching solution and a consequent different tuning of the rest of the solution. The optimal one is, as mentioned above, in the fabrication process:

- $H_2O/C_6H_8O_7/H_2O_2/H_3PO_4$: 21/5/0.5/0.25 vol ($C_6H_8O_7$ 1M, H_2O_2 30% in mass and H_3PO_4 85% in mass, etching rate $\sim$ 50 nm/min)

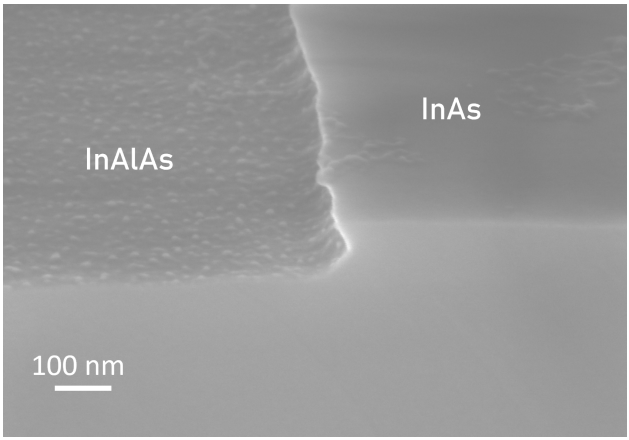


Figure 3.2: Tilted SEM micrograph of a cleaved InAs mesa. This image was taken to see the angle formed with the rest of the substrate.

As we can see in Fig. 3.3, the angle between the InAs mesa and the etched InAlAs metamorphic buffer layer is obtuse as we wanted, making it more straightforward to step on the InAs mesa with the Al contacts.

3.2 Low temperature measurement setup

All measurements that will be shown in this thesis were performed in a filtered cryo-free dilution refrigerator (Triton 200 by Oxford Instruments). The base temperature of this cryostat was around 25 mK.
The electrical scheme used to characterize the samples presented in the thesis is shown in Fig. 3.4. Multiple electrical DC lines connect the external room-temperature instruments to the cryostat sample holder, which is thermally anchored to the mixing chamber (MC) plate at the base temperature. Mounted on the sample holder of the fridge is the 24-pin DIL with the sample.

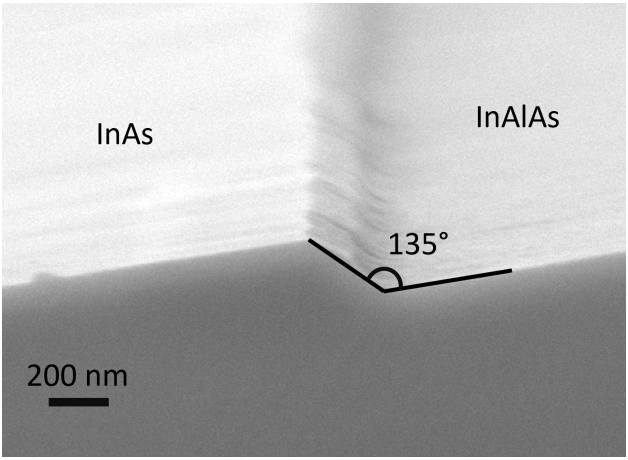


Figure 3.3: SEM image of a cleaved InAs etched mesa. The angle formed between the InAs mesa and the InAlAs wet-etched metamorphic buffer layer is visible. The value of $\sim 135\circ$ suggests that the etching rate in the vertical and horizontal directions is the same.

To reduce room temperature noise, each line is filtered with two series low-pass RC filters, with resistances and capacitances $R = 1\text{k}\Omega$ and $C = 47\text{nF}$, two LC π-filters, and another low-pass coaxial filter (VLFX-80 by Mini-circuits) with a cut-off frequency of 80MHz. As we can see in Fig. 3.4, one of the π-filters is placed outside the cryostat at room temperature, the coaxial filter is placed inside the cryostat but outside the MC, and the last two RC and π filtering stages are inside the MC. In addition to frequency filtering, multiple cold-filtering stages along the DC line are necessary to thermalize the signal and reduce noise from room temperature. The total in-series resistance of the filters is $\sim 2.11\text{k}\Omega$ and the resulting cutoff frequency is $\sim 1\text{kHz}$.
The sample holder is placed at the center of a superconducting coil,

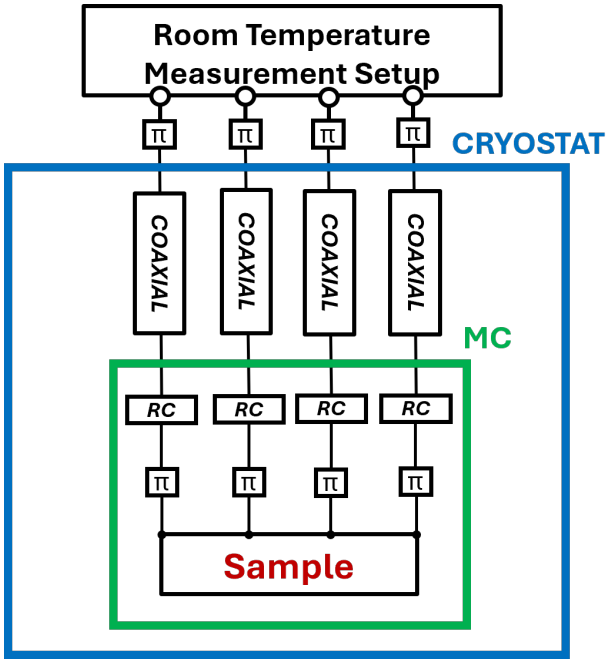


Figure 3.4: Electrical scheme used for the measurements. The elements inside and outside the cryostat are shown, as long as the elements inside the MC plate.

which can generate magnetic fields orthogonal[2] to the sample surface. The field/current ratio is 0.1663T/A, and the maximum field that can be generated is 0.4T. The magnet is driven by a Keithley 2602 power supply, which is used as a current source.
All the room temperature instrumentation is handled by a PC (with LabVIEW software) and connected to it via a General Purpose Interface Bus (GPIB, IEEE 488).

[2]; also parallel magnetic fields are available if a suitable sample holder is mounted, but we will never use them and so this feature will not be mentioned anymore

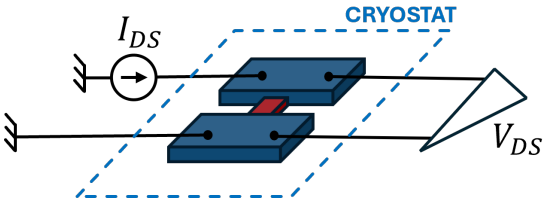


Figure 3.5: Logical scheme of a 4-wire switching current measurement, where a current source (I_{DS}), a voltage drop measure V_{DS} at room temperature, and a superconductive structure with switching current I_S inside the dilution cryostat are shown.

3.2.1 Switching current measurements

The most recurring measurement throughout this work will be about switching currents. This measure is taken through a standard 4-wire measurement setup where a current I_{DS} is injected from the source electrode (S) to the drain electrode (D), and at the same time, the voltage drop V_{DS} is recorded across the structure studied. Although the structure is superconducting V_{DS} is 0[3] but when the current injected exceeds the maximum value supported, the structure becomes resistive and a non-0 V_{DS} is measured. The current source shown in Fig. 3.5 is generated by a voltage source (Yokogawa GS200) with a series load resistor. This setup creates an ideal current generator if the load resistor is much larger than the series resistance of the DC line and the sample. The usual values for this load resistor are 100 kΩ-1 MΩ. The voltage is measured with a voltage amplifier (DL Instruments 1201), which has a variable amplification factor of 1 to 10000 and an input impedance of 5 GΩ. The output signal from the voltage amplifier is finally measured via a multimeter (HP/Agilent 34410a).

[3]From the experimental point of view, the measured voltage cannot be identically 0, more precisely, our 0 V will be represented by the noise bandwidth of the measurement setup.

Chapter 4

Bipolar thermoelectric single-electron transistor

This chapter describes a theoretical work on bipolar thermoelectricity on a single-electron transistor. In line with the aim of this thesis as a whole, the main feature analyzed is the possibility of tuning thermoelectricity via electrostatic gating.
In this theoretical work, we consider an *SIS'IS* structure where a central superconducting (SC) island featuring strong Coulomb interaction is sandwiched between two SC leads via tunnel barriers. In such a system, the origin of the bipolar thermoelectric properties differs significantly from that of the standard thermoelectricity in quantum dots. The reason lies in the *substantial* violation of the detailed balance induced by the temperature difference in the junction and the interacting nature of the BCS theory. Furthermore, we exploited the Coulombic island's gating properties to control the engine's thermoelectric performance. This unique electrical tunability differs from other platforms [39], and can be relevant for on-chip energy harvesting and other energy management purposes in superconducting quantum processors and radiation sensors [40].

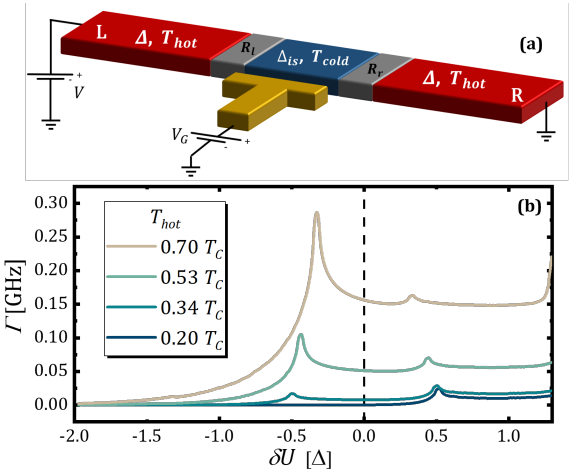


FIGURE 4.1: **(a)**: Scheme of the *SIS'IS* transistor. The red-coloured parts show the hot superconductors and the blue-coloured part shows the cold ones. V and V_G denote respectively the source-drain and gate voltages. **(b)**: Sequential tunneling rates versus energy for different values of T_{hot} at $T_{cold} = 0.2\ T_C$. Here we set $\Delta = 220\ \mu$eV (corresponding to Al, aluminum), $\Delta_{is} = \Delta/2$, which can be obtained using a normal metal-superconducting bilayer [22], and all identical barrier resistances $R = 1\text{M}\Omega$.

4.1 Theoretical model

The *SIS'IS* structure under investigation is shown in Fig. 4.1(a), and consists of two superconducting (SC) leads (L,R, red part in Fig. 4.1(a)) with an SC gap Δ put in tunnel contact with a Coulombic island (central blue part in Fig. 4.1(a)) with a different SC gap Δ_{is}, through two identical barriers of resistance $R_{L/R}$. To observe bipolar thermoelectricity, the leads are chosen to have a larger gap than the island, $\Delta > \Delta_{is}$. They are kept at a temperature $T_{hot} > T_{cold}$ greater than the island temperature, $T_{is} \equiv T_{cold} = 0.2\ T_C$, where T_C is the critical temperature of the superconducting leads. Tunnel barriers are assumed to be resistive enough to make Josephson energy negligible with respect to thermal energy, allowing Josephson coupling to be

neglected [41]. However, to observe the Coulomb blockade, we assume the charging energy of the central island, $E_C = e^2/2C_{tot}$, with C_{tot} the total capacitance of the island, large enough for $E_C \gg k_B T_l$ with $l = is, L, R$ and $E_C \gtrsim \Delta$.

As already analyzed in section 2.4, for sufficiently resistive barriers we are in the sequential tunneling regime and the full transport properties of the system can be described through the rates $\Gamma_j(\delta U)$, with $j = R, L$, which describe the tunneling probability through the j-th barrier by the Fermi golden rule [14, 24]

$$\Gamma_j = \frac{1}{e^2 R_j} \int_{-\infty}^{\infty} dE \; n_{is}(E + \delta U)[1 - f_{is}(E + \delta U)] n_j(E) f_j(E), \quad (4.1)$$

where e is the electron charge, δU is the electrostatic energy acquired ($\delta U > 0$) or lost ($\delta U < 0$) during the tunneling process [14], $n_l(E) = \left| Re[(E + i\gamma)/\sqrt{(E + i\gamma)^2 - \Delta_l^2(T_l)}] \right|$ is the (smeared by non-zero $\gamma \ll \Delta_l$) BCS density of states (DOS) of the $l = is, L, R$ element [11], and $f_l(E)$ the Fermi-Dirac distribution function at equilibrium temperature T_l. We assumed that the SC island was fully in equilibrium at its temperature T_{is}.

4.1.1 Strong violation of detail balance

The electron tunneling rate from the lead to the island as a function of the electrostatic energy difference δU contains crucial physics for the bipolar thermoelectric effect, and it is shown in Fig. 4.1(b) for different temperatures T_{hot}. At equilibrium, $T_{hot} = T_{cold}$ (dark blue line), we notice a small peak at $\delta U^* = \Delta - \Delta_{is} > 0$, which corresponds to the matching of the DOS divergences of the two different superconductors and is activated by temperature, since at zero temperature it is completely Pauli blocked. At finite temperature in equilibrium, the rates satisfy the detail balance $\Gamma(-\delta U) = e^{-\delta U/k_B T}\Gamma(\delta U)$, so correspondingly we expect a small peak [although not visible in Fig. 4.1(b)] to exist at negative energies $\delta U = -\delta U^*$ as well. More

intriguing physics arises in out-of-equilibrium conditions. By increasing the lead temperature, $T_{hot} > T_{cold}$, the peak at negative energy emerges and becomes much stronger than its counterpart at positive energy (brown line). This is an unusual situation in which $\Gamma(-|\delta U|) > \Gamma(|\delta U|)$, and we identify it as a *strong violation of the detailed balance*. This arises from a finite temperature difference, which populates more states at higher energy in the hot leads. From Eq. (4.1) a strong violation is possible *only if* for some energy $\epsilon, \delta U > 0$ we have

$$n_{is}(\epsilon - \delta U)[1 - f_{is}(\epsilon - \delta U)] > n_{is}(\epsilon + \delta U)[1 - f_{is}(\epsilon + \delta U)]. \quad (4.2)$$

This inequality constitutes a *necessary* condition and depends only on the island DOS and on its Fermi function. It can be shown that Eq. (4.2) is meaningful *only if* there is a gap asymmetry between the hot and cold sides, and the superconducting DOS features a monotonically decreasing energy dependence for $|E| > \Delta$ [20]. Furthermore, to be satisfied, Eq. (4.2) *implicitly* requires that the BCS island DOS shifts with the electrochemical potential (the electrostatic energy difference δU in the rate). Indeed, if the DOS does not depend on δU (i.e., substituting $n_{is}(\epsilon \pm \delta U) \to n_{is}(\epsilon)$ as in a semiconductor) Eq. (4.2) cannot be satisfied since $n_{is} > 0$. Thus, the substantial violation stems essentially from the interacting character captured by the BCS mean-field theory, and, as we are going to show, it is the essential precursor of the bipolar thermoelectric phenomena. The fundamental role of the interaction also clarifies well why this effect can be associated with spontaneous symmetry breaking of the PH symmetry induced by the out-of-equilibrium condition [20, 22, 23].

4.1.2 Sufficient conditions for the strong violation of the detailed balance

It is interesting to discuss which are the conditions to observe the strong violation of the detailed balance reported before for the golden

rule rate of Eq. (4.1). For a Coulomb island, at equilibrium in the temperatures, the rates usually satisfy the detailed balance

$$\Gamma(-\delta U) = e^{-\beta\delta U}\Gamma(\delta U), \tag{4.3}$$

with the inverse temperature $\beta = 1/k_B T$. This property guarantees that the final distribution of the quantum dot states follows the standard Boltzmann distribution, so that the n charge states of the island have an occupation probability $p(n) \propto e^{-\beta E_c(n)}$, with $E_c(n)$ the energy of the state [42]. However, it is clear that when the island and the leads have different temperatures $\beta_j \neq \beta_{is}$, the detailed balance is necessarily violated. We showed a case where the violation is extreme: when the "backward" rate (which promotes electron tunneling in an energetically unfavorable state) is favored in comparison to the "forward" rate, i.e.

$$\Gamma(-\delta U) > \Gamma(\delta U), \tag{4.4}$$

with $\delta U > 0$. Observing that the functions determining the rate are all positive, $0 \leq f_j, n_j$, and the Fermi distribution satisfies $f_l \leq 1$, and assuming the EH symmetry for the leads, one can easily see that Eq. (4.4) can be satisfied (as seen in the previous section) *only if* for some energy $\delta U > 0$ we have

$$n_{is}(\epsilon - \delta U)[1 - f_{is}(\epsilon - \delta U)] > n_{is}(\epsilon + \delta U)[1 - f_{is}(\epsilon + \delta U)]. \tag{4.5}$$

Since this is a necessary condition, it is instructive to examine the requirements the island DOS must meet to promote the strong violation. We see immediately that for an energy independent DOS of the island $n_{is}(\epsilon) = const$ (non superconducting metallic island), the inequality cannot be satisfied since the Fermi function is a monotonously decreasing function of the energy, i.e. $f_j(E) \geq f_j(E')$ for $E \leq E'$. Without any other assumptions about the DOS, it immediately follows that an NIN junction cannot ever exhibit a strong violation of detailed balance. This argument also implies that an SIN junction cannot show any strong violation of the detailed balance. In turn, for an SIS junction, inequality Eq. 4.4) can

be potentially satisfied because, for a standard BCS DOS, it can happen that $n_{is}(\epsilon - \delta U) > n_{is}(\epsilon + \delta U)$ for $\epsilon > \Delta_{is}$, compensating the natural opposite behavior induced by the term $1 - f$ not to violate the inequality. This demonstrates the importance of the DOS's energy dependence at least for some energies. However, one needs to exclude the case of two identical superconductors. Indeed, for a pure SIS case, i.e. $n_{is}(\epsilon) = n_j(\epsilon)$, an exchange in the roles of the DOS between the lead and the island is fully equivalent to a change in sign of the temperature difference, with a consequent temperature-independent violation of the detailed balance, which implies the violation of the second principle of thermodynamics. Thus, the condition of strong violation of the detailed balance identifies a physical mechanism in which, for some states in a certain range of energies, it is convenient to go against the electrostatic energy. It is important to stress again that the inequality Eq. (4.5) is a *necessary* condition but *not a sufficient* one to realize the reported strong violation (notice that the inequality Eq. (4.5) depends only on the island temperature and, obviously at equilibrium, the detailed balance must be satisfied, implying the necessary character of Eq. (4.5) but not the sufficient one). As discussed also in [20, 43] the temperature difference must be operated in such a way that the large gap is kept at a temperature higher than the small gap. Furthermore, the condition of the monotonously decreasing density of states for $\epsilon > 0$ does not necessarily imply superconductivity as a requirement. This was discussed in the supplementary material of Ref. [20], for example a Lorentzian density of state $n_{is}(\epsilon) \propto \gamma/(\gamma^2 + \epsilon^2)$, if always centered on the chemical potential, can also determine the violation of the inequality, thus enlarging the range of cases where the strong violation of the detail balance can be indeed similarly reported beyond BCS superconductivity. Finally, we wish to note, importantly, another requirement that needs to be satisfied in order to make possible the strong violation of the detail balance. By inspection of Eq. (4.5), it follows that the argument of the island DOS must shift with the energy δU, i.e., $n_{is}(\epsilon \pm \delta U)$. Indeed, the DOS shifts with δU because the SC gap opens at the Fermi energy as a result

of the *intrinsic* interacting nature of the Cooper instability. Notably, this complexity is elegantly accounted for by BCS mean-field theory, whose simplicity, in turn, may mask its profound origin. For example, in a semiconductor with a similar band gap, the chemical potential is determined by the electron density. It is not fixed to reside in the gap. It follows that the DOS does not shift with the electrostatic energy. In turn, in a superconductor, when the electrochemical potential is changed, such as by a bias is applied to a junction, the DOS shifts with it. In the Coulomb island we are considering, the role of the bias is essentially played by the electrostatic energy difference δU. The importance of the interaction was never particularly stressed before. Still, the rate analysis discussed here shows it in a crystal clear way and also sheds light on the physics of bipolar thermoelectricity in the whole sense [20, 43]. In that case, we can also state that the mean-field nature of the BCS theory, which properly takes into account the important part of the interaction, is a crucial ingredient behind the bipolar thermoelectricity in the tunneling limit. This conclusion can also be inferred from the experimental observation that bipolar thermoelectricity is associated with a spontaneous breaking of the EH symmetry. In the experimental demonstration of the bipolar thermoelectric effect, we also observed a current-controlled hysteretic cycle of the junction, clearly demonstrating the reality of spontaneous symmetry breaking of EH symmetry. The analysis presented so far assumed a finite δU, thereby implying nonlinearity in the electrostatic energy difference. This is meaningful since the maximum violation of the detail balance appears in the match-peak conditions $\delta U = \pm(\Delta(T) - \Delta_{is}(T))$. However, it is interesting to look at what happens at very low energies $\delta U \to 0$. By expanding the rate, we find that

$$\left.\frac{\partial \Gamma_j}{\partial \delta U}\right|_{\delta U=0} = \frac{1}{e^2 R_j}\int_{-\infty}^{\infty} d\epsilon \left(\frac{\partial n_{is}(\epsilon)}{\partial \epsilon}[1 - f_{is}(\epsilon)] - n_{is}(\epsilon)\frac{\partial f_{is}(\epsilon)}{\partial \epsilon}\right) n_j(\epsilon) f_j(\epsilon). \tag{4.6}$$

Clearly, the first term is not present if the DOS of the island n_{is} is not affected by the energy δU, and we are left with only the second term that is always positive. So *only if* the island DOS is monotonously

decreasing, i.e. $\partial_\epsilon n_{is} < 0$ for $\epsilon > 0$, one could even have a negative $\partial\Gamma_j/\partial\delta U < 0$ which strongly violates the detailed balance. So, the arguments that we have made before in nonlinear cases ($\delta U \neq 0$) can be repeated in the linear case. In particular, the presence of a negative $\partial\Gamma_j/\partial\delta U$ in the linear regime of δU is necessarily associated with the interaction effects included by the island DOS by the BCS theory. A similar phenomenology is also observed at the current level of the SIS' junction, where at low bias a negative differential conductance is reported [20]. This is again connected to the SSB of the EH symmetry, which creates an unstable situation, as shown by the substantial violation of detailed balance, where the system tries to push particles against the natural direction dictated by the electrostatic energy. This intrinsic instability constitutes, at the same time, an arbitrarily substantial violation of the non-equilibrium fluctuation-dissipation theorem, which is nevertheless valid at thermal equilibrium due to detailed balance.

4.1.3 Quasiparticle current

In the sequential tunneling approximation we get the electric current already shown in Eq. 2.20 through a standard master equation approach [42, 44–46], in which the time-evolution of the population $\sigma(n)$ of the island charge state n is determined by $\dot{\sigma}(n) = \sum_{n'} \mathbf{W}_{nn'}\sigma(n')$. The kernel $\mathbf{W}_{nn'} = \sum_{j=R,L} \Gamma_j^{nn'}$ with the diagonal terms $\mathbf{W}_{nn}$ fixed by the conservation of probability, $\sum_n \sigma(n) = 1$ implies $\sum_n \mathbf{W}_{nn'} = 0$. The rates $\Gamma_j^{n,n\pm1} = \Gamma_j(\delta U_{n,n\pm1})$ correspond only to the transitions $n = n' \pm 1$ described by the rates of Eq. (4.1). The electrostatic energy difference is $\delta U_{n,n\pm1} = U(n\pm1) - U(n) \pm eV/2$ [14, 42, 47], with $V = V_L - V_R$ the source-drain bias, and $U(n) = E_C(n - q_{is}/e)^2/2$ the electrostatic energy, which depends on the offset charge on the island $q_{is} = C_g V_g + \sum_j C_j V_j$, with C_g the gate capacitance and C_j the j-th barrier capacitance (for which $C_{tot} = C_g + C_L + C_R$). In the stationary limit [47], the current can be calculated simply in the right lead $I = I_R = -I_L = e\sum_n [\Gamma_R^{n,n+1} - \Gamma_R^{n,n-1}]\sigma^0(n)$ where $\sigma^0(n)$ is the stationary probability of the island charge states. This general

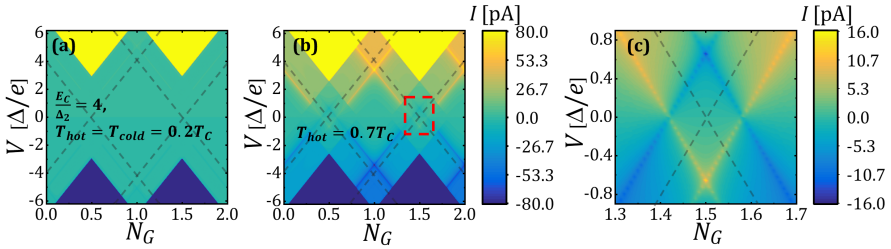


Figure 4.2: **(a)**,**(b)**: Charge current flowing through the *SIS'IS* structure at thermal equilibrium (**a**) and in the non-linear regime (**b**) versus V and $N_G = C_G V_G/e$. The color scale is the same for both graphs. **(c)**: Blow-up of the red-dashed region shown in panel (**b**) where the onset of the thermoelectric behaviour is clearly visible. The calculation parameters are as in Fig. 4.1.

numerical approach can be further simplified in the Coulomb blockade regime $k_B T \ll E_C$ by noting that the dominant contribution to transport at one resonance is associated only with tunneling rates involving neighboring charge states $n-1 \rightleftharpoons n$. The current in such a case can be written as

$$I_n = e\frac{\Gamma_L^f(n-1)\Gamma_R^f(n) - \Gamma_L^b(n)\Gamma_R^b(n-1)}{\Gamma_L^f(n-1) + \Gamma_R^f(n) + \Gamma_L^b(n) + \Gamma_R^b(n-1)}, \tag{4.7}$$

where we use a shortened notation for the rates $\Gamma_j^{f/b}(n) = \Gamma_j(\pm\delta U_{n,n\pm1})$. Since we are mainly interested in the deep subgap regime in the bias range $|eV| < 2\Delta$ with $E_C = 4\Delta$, we approximate the current considering the dominant contribution of two neighboring Coulomb resonances, i.e., $I = I_n + I_{n+1} + \mathcal{O}(e^{-E_c/2k_B T_{hot}})$.

4.2 Results

4.2.1 Coulomb diamonds

Figures 4.2(a),(b) show the current I as a function of the source-drain bias V and the gate-tunable offset charge $N_G = C_g V_g/e$.

Typical Coulomb diamonds appear, which display periodicity in the offset charge N_G in units of the electron charge e. The system does not present any even-odd effect since the average Cooper pair recombination rate in our system $\Gamma_r \simeq 16$kHz [48] is much smaller than the tunneling rates $\Gamma_j \sim I/e$ (inverse average electron dwelling time on the island). Coulomb diamonds in equilibrium are shown in Fig. 4.2(a). As a guide for the eye, we show with black dashed lines the boundaries of the Coulomb diamonds for $\Delta = 0$ (see also Fig. 2.6), where the electrostatic energies vanish, $\delta U_{n,n\pm1}(N_G, V) \equiv 0$. As expected, the SC gap shifts the boundaries of the Coulomb diamonds to higher energies. The charge transport is suppressed in the (N_G, V) plane domains satisfying $(eV < 2\Delta + 2\Delta_{is} \approx 3\Delta)$ due to the vanishing DOS for quasiparticles in this range[1].

In Fig. 4.2(b) we show the results for the non-equilibrium case, $T_{hot} = 0.7\ T_C > T_{cold}$. Subgap conduction channels become clearly visible, as thermally excited states promote the stronger emergence of the matching peak resonances. At integer N_G and $|eV| \sim 3\Delta$, where transport is dissipative $(IV > 0)$ even if it is entirely within the Coulomb blockade diamond, we clearly see the appearance of yellow (blue) crosses at positive (negative) V. These features stem from the enhancement of the *negative energy* peak in the tunneling rate for electrostatic energy $\delta U \approx -\delta U^*$ [see Fig. 4.1(b)], and are also a direct consequence of the substantial violation of the detailed balance, even if their nature is still dissipative. More intriguingly, for half-integer N_G and $eV \sim \Delta/2$, the sign of the current becomes opposite to the bias $IV < 0$, as shown in the blow-up of Fig. 4.2(c). This behavior is a signature of thermoelectricity, and appears *only* when a finite temperature difference is applied between the island and the hot leads. These subgap structures are present at both positive and negative biases for the *same* temperature difference, showing the full *bipolar* character enforced by the EH symmetry of

[1]We remember that, as previously said in section 2.4, we are considering only quasiparticle transport because of the ratio between the Josephson energy $E_J = \hbar I_c/(2e) \propto 1/R_T$ and the thermal fluctuations, $E_J \ll k_B T$ which suppresses all the Josephson effects.

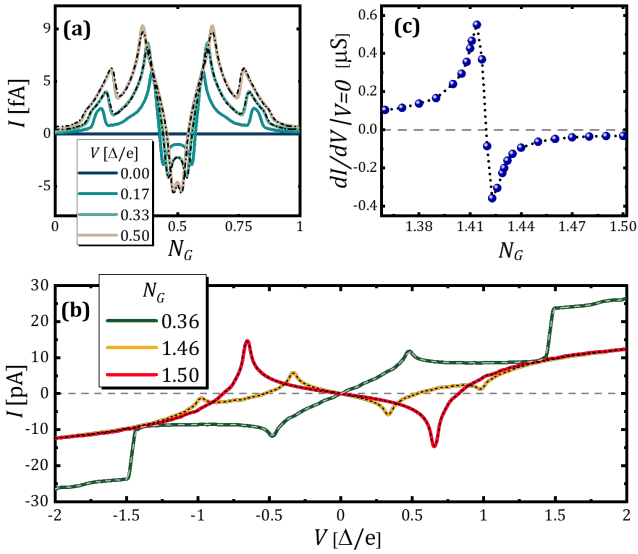


FIGURE 4.3: Out-of-equilibrium ($T_{hot} = 0.7T_C$) current I as a function of: (**a**) N_G for different values of V, and (**b**) V for different values of N_G (respectively horizontal and vertical cuts of Fig. 4.2(**b**)). The dashed lines correspond to the prediction of the simplified model Eq. (4.7), showing its validity in the case of $E_C \gg eV$. **(c)**: Out-of-equilibrium zero-bias conductance as a function of N_G calculated for the curves in (**b**).

the unbiased system. The emerging bipolar thermoelectric effect is similar to SIS' systems [43]. Furthermore, our bipolar thermoelectric superconducting transistor offers the possibility of being manipulated via Coulomb interactions and associated gating effects. We also notice that, unlike a conventional quantum-dot thermoelectric effect [49, 50] that is activated by a temperature gradient *between* the leads, the present effect appears when the leads have the *same* temperature, higher than the Coulomb island

Figure 4.3(a) displays cuts of Fig. 4.2(b) at different V. In a region around half-integer gate charge N_G, we clearly see a change of

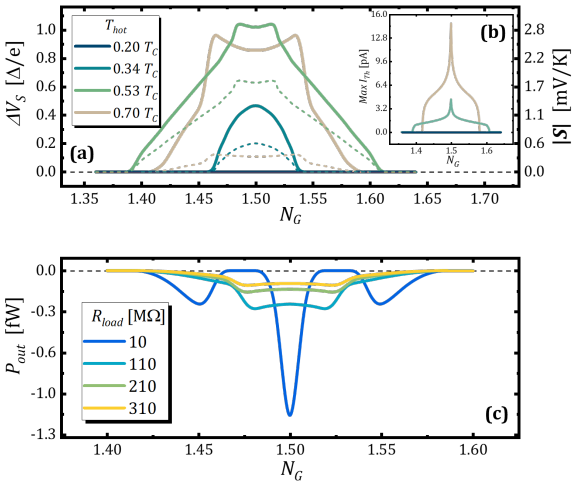


FIGURE 4.4: **a**: Seebeck voltage (left y-axis) and nonlinear Seebeck coefficient $|\mathcal{S}|$ (right y-axis) versus N_G for different values of T_{hot}. **b**: Maximum thermocurrent versus N_G for different values of T_{hot}. **c**: Power output $P_{out} = -\widetilde{I}\,\widetilde{V}$ versus N_G for different values of the load resistor. $\widetilde{I}$ and $\widetilde{V}$ are the solutions of the intersection of the IV characteristics with the load line of the resistor. Note that among all possible solutions, only the electrically stable one, i.e., that with $dI/dV > 0$, can be operated by the engine [20, 41].

the sign of the current around the Coulomb resonance in opposition to the bias (thermoelectric effect). In particular, the sign of the thermoelectric current does not change passing through the resonant value due to the unique bipolar nature, unlike the conventional (unipolar) thermoelectric effect on a quantum dot [51].

In Fig. 4.3(b) we show cuts of Fig. 4.2(b) at fixed N_G. We first focus on the zero-bias behavior: as we vary N_G towards half-integer values, the zero-bias conductance (ZBC) $G_0 = dI/dV|_{V=0}$ becomes negative at the critical value $N_G^* \approx 4.42$ [see Fig. 4.3(c)]. This behaviour blatantly suggests the spontaneous breaking of the EH symmetry of the system [20, 43], and highlights the unique capability

of gate control in our system, which, unlike other platforms [39], allows us to tune the emergent bipolar thermoelectric properties continuously. A negative ZBC, together with the condition $I(0, \Delta T) = 0$ dictated by the EH symmetry, implies the existence of thermoelectricity ($IV < 0$) and the existence of a Seebeck voltage V_S, since at high biases $eV \gg 3\Delta$ the system necessarily becomes dissipative again, $IV > 0$. Interestingly, this implies that the Seebeck voltage (i.e., the open-circuit voltage defined by $I(V_S) = 0$) is expected to depend on the gate voltage, $V_S(N_G)$, with clear consequences for the gate-tunability of the thermoelectric performance. At finite values of V, the current exhibits a peak change in sign (thermoelectricity) when N_G approaches half-integer values. The system shows an absolute negative conductance and thereby thermopower, $\dot{W} = -IV > 0$. Furthermore, for some values of N_G, the IV curve presents more than one resonant peak (see yellow line): this is a consequence of the Coulomb blockade, since the island electrostatic energy differences δU for different rates depend on the gate N_G and bias V, and correspondingly, the matching peaks resonance of the dominant rates appear split for non-resonant values $N_G \neq 1/2+n$ of the IV curve. Note that a similar double-peak structure can also be observed as a function of N_G, as shown in Fig. 4.3(b).

4.2.2 Thermoelectric figures of merit

The intrinsic nonlinear nature of this effect does not allow us to describe the thermoelectric figures of merit of our system using a linear thermoelectric approach [52]. However, we can still define a Seebeck voltage V_S and a nonlinear Seebeck coefficient $\mathcal{S} = V_S/\Delta T$ with $\Delta T = T_{hot} - T_{cold}$. We stress that EH symmetry implies two Seeback voltages, $\pm V_S$, and a *bipolar* $\mathcal{S}$ [20]. Figure 4.4(a) shows V_S (solid line, left scale) and $|\mathcal{S}|$ (dashed line, right scale) as a function of N_G for different temperatures of the leads. By changing T_{hot}, the Seebeck voltage shows horn-like nonlinear features that are even higher at a slightly lower value of T_{hot}.

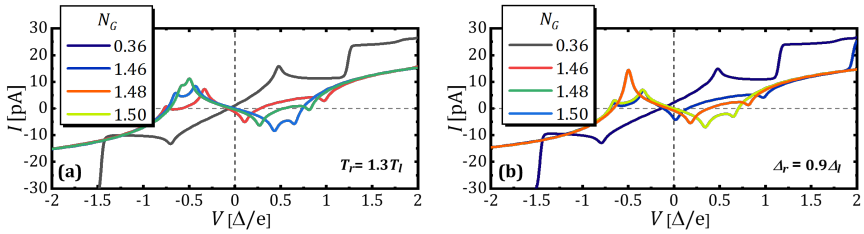


FIGURE 4.5: **(a)**:Source grain current I as a function of source drain bias V with $T_{cold} = T_{is} = 0.2T_C$, $T_l = 0.7T_C$ and $T_r = 1.3T_l$, for different values of N_G.**(b)**:Source grain current I as a function of source drain bias V with $\Delta_{is} = \Delta/2$, $\Delta_l = \Delta$ and $\Delta_r = 0.9\Delta$, for different values of N_G.

Inspecting Fig. 4.3(b), we recognize that the yellow curve has two peaks and for specific values of ΔT the second peak can even cross the $I = 0$ axis, returning a higher open circuit (Seebeck) voltage. Analogously, $\mathcal{S}$ is also similarly affected and its maximum value is not necessarily associated with the maximal thermovoltage (due to the nonlinearities, it is not even necessarily associated with the highest temperature difference ΔT). In Fig. 4.4(b) the maximum thermocurrent $I_{max}(N_G) = \max_{0<V<2\Delta/e}[|I(V, N_G)|]$ as a function of N_G is shown to gradually decrease while lowering T_{hot}, as expected, since the temperature difference is not enough to trigger bipolar thermoelectricity [22, 23]. The character of a transistor thermoelectric generator appears when the circuit is closed on a load resistor. Figure 4.4(c) displays the output power of the structure as a function of N_G for different values of the load resistor, demonstrating the ability to fine-tune the gating control of the output power. The maximum achievable output power is typically associated with the smallest possible load resistance and is dependent on several parameters.

4.3 Differences with the conventional thermoelectricity in quantum dots

In this section, we discuss the crucial differences between the bipolar thermoelectric effects of the system studied in this work and the unipolar thermoelectricity that usually appears in conventional quantum dots [49, 50]. Quantum dots can be tuned via an external gating to be *non* EH symmetric [14], thus generating a thermoelectric effect. It is well known that quantum dots can exhibit a gate-dependent linear thermoelectric effect when a thermal gradient is applied across the system, i.e., when the temperatures of the source and drain leads differ. In particular, the sign of the Seebeck coefficient can be reversed by appropriately applying a gate. The gate is indeed capable of moving the system from an electron-like to a hole-like character. However, we term this effect unipolar since once the gating condition is fixed, a change in the thermal gradient causes a sign change in the thermoelectrical response. Furthermore, the presence of a thermal gradient between the leads makes, in general, the structure also non-symmetric by inversion, so in the case of a unipolar thermoelectric effect, a non-reciprocal IV characteristic $I(V, \Delta T) \neq -I(-V, \Delta T)$ also appears. This situation differs significantly from the *bipolar* thermoelectric effect reported in this work, where the temperature difference between the island and the leads does not determine the sign of the thermoelectricity; instead, it is determined solely by spontaneous symmetry breaking. This is a real crucial difference between the two effects. Indeed, in the system we discuss in this work, it is essential to apply a thermal gradient between the central island and the two external leads (kept at the same temperature). This configuration is not expected to generate any net thermoelectric effect classifiable as a standard *unipolar* thermoelectrical contribution. Indeed, the thermal gradients at the two junctions have opposite signs relative to the current flow through the system, and, for identical left/right tunnel barriers, we consider that no net unipolar thermoelectric contribution is generated. Notice that this thermal configuration is well known not to create a net

(unipolar) thermoelectric effect. For comparison, thermoelectric cells usually combine materials with p- and n-type characteristics, with opposite signs of the thermoelectric coefficient (thermocouple configuration). In conclusion, the temperature configuration considered in the system uniquely proves the bipolar nature of the effect. This has also been discussed elsewhere [43], but here we demonstrated that the same arguments also apply substantially in the presence of Coulombic effects.

At the same time, one can speculate that if the right/left barrier symmetry is broken, a net linear thermoelectrical effect may eventually emerge. General considerations arising from the EH symmetry of the system [53] suggest that, at the linear level, this configuration would not generate any linear thermoelectric effect. However, the bipolar effect is nonlinear, requiring a finite temperature difference and sometimes a finite bias, so those general linear arguments do not apply. It is interesting to explore how different conditions for the system (and its parameters) affect the reported evidence. We tested a different set of cases, changing the structure in Fig. 4.1(a), keeping the exact configuration of temperatures (cold island and with hot leads at the same temperatures). In particular, we tested all the following configurations:

- Full metallic structure (no superconductors) with equal tunnel barriers ($R_l = R_r$),
- Full metallic structure with different tunnel barriers ($R_l \neq R_r$),
- Metallic dot with superconductive leads with equal tunnel barriers ($R_l = R_r$),
- Metallic dot with superconductive leads with different tunnel barriers ($R_l \neq R_r$),
- Superconductive dot with metallic leads with equal tunnel barriers ($R_l = R_r$),
- Superconductive dot with metallic leads with different tunnel barriers ($R_l \neq R_r$).

None of these configurations showed any thermoelectricity. This result can be seen as a consequence of the fact that thermoelectricity in our system is strongly correlated with the nature of the BCS DOS of the island and, as pointed out in the previous discussion, leads to the necessary conditions for bipolar thermoelectricity.

4.4 Robustness of the effect

However, if the temperatures of the external right/left superconducting leads differ, one can expect a contribution from the standard unipolar thermoelectric effect. So, even in the case of a non-perfect temperature profile, an experiment can address the signature of the reported effect. Similarly, one could speculate about what happens if the gaps in the superconducting leads are not identical, as we assumed before. In other words, hereafter we want to discuss the robustness of the effect with respect to changes in the temperatures or gap profiles assumed before. We will separately consider the two most interesting cases: *i)* the temperature of the leads is not perfectly equal and *ii)* the SC gap of the leads is not perfectly equal.

Taking into account the first case, in Fig. 4.5(a), it can be observed that the IV characteristic is higher than the temperature of the right lead than the temperature of the left lead. Here we have $T_{is} = 0.2T_C$, $T_l = 0.7T_C$, $T_r = 0.8T_C$, where T_{is} is the temperature of the island and T_l, T_r are the temperatures of the left and right leads, respectively. These curves are still reminiscent of the bipolar thermoelectric effect discussed earlier in Fig. 4.3(b). However, on top of that, we can recognise the contribution of the *unipolar* thermoelectric effect that mainly shifts the intercept of the curves to zero bias. Indeed, these IV curves lose reciprocity $I(V, \Delta T) = -I(-V, \Delta T)$, as a direct consequence of the emerging unipolar thermoelectricity that the non-symmetric temperature configuration of the external leads will determine, being associated with the *conventional* thermoelectrical behavior of the quantum dots. However, if the quantum dot is gated exactly at the Coulomb resonance, such as $N_G = 4.5$, the

EH symmetry of the symmetry is again restored: there are no linear unipolar thermoelectric effects and the reciprocity of the IV curves is fully restored. However, in that case, intriguing differences can also be seen with respect to the result reported in Fig. 4.3(b). In particular, the difference between the IV curves where two thermoelectric peaks appear at the Coulomb resonance is shown, whereas in Fig. 4.3(b) we have only a peak matching one-peak for that gate value. Indeed, the temperature difference of the leads also determines a different value for the superconducting gaps in the leads, i.e. $\Delta_r(T_r) \neq \Delta_l(T_l)$, as predicted by BCS [10]. So, correspondingly, two different matching peak values depend on which barriers the tunnelling takes place. This results in a double-peak structure also at the resonance. However, even if some of the peculiarities of the bipolar thermoelectric effect are lost, at least comparing Fig. 4.5(a) with Fig. 4.3(b), we can still conclude the existence of *the bipolar* thermoelectric effect component. Many of the figures of merit discussed in this chapter remain roughly valid and are not substantially affected by a moderate temperature gradient across the leads.

Finally, we wish to show the possible consequences of the fact that two external leads have slightly different zero-temperature gaps. However, for simplicity, the temperature configuration is taken to be the same as before. In this case, it can be seen from Fig. 4.5(b) that the situation reminds one of aspects of the previous case. Anyway, the right/left symmetry is also broken here. In this case, too, we can conclude that the effect previously described is sufficiently robust and does not need fine-tuning of the parameters to be observable.

Chapter 5

e-ph coupling in InAs on insulator (InAsOI)

In this chapter, we aim to lay the groundwork for the caloritronic experimental work presented in Chapter 3. Here, we aim to demonstrate the promising properties of the InAs-on-insulator (InAsOI) platform for caloritronic applications. In particular, we will explain why we chose this semiconductive platform and why it is crucial for the implementation of performing and electrostatically gateable caloritronic architectures.
The central figure of merit to be discussed is the *electron-phonon interaction*, as it is one of the main energy-loss processes in heat-transport and energy-management experiments.

5.1 Aim of the work

Past research has explored hot-electron effects and the electron-phonon (e-ph) interaction in semiconductors [54–56]. It is known that semiconductors have a weaker e-ph interaction compared to metals. However, a significant drawback for coherent caloritronics and Josephson physics applications is the non-Ohmic barrier that they typically create in superconducting metals. In this study, we focus on investigating a recently proposed superconductor-semiconductor

hybrid platform based on an InAs heterostructure grown on an insulating buffer of InAlAs, known as InAs On Insulator (InAsOI) [1] [57], which, as we will show, has an extremely weak e-ph interaction. This can be demonstrated by the minimal power required to raise the electronic temperature above the phonon bath temperature by a significant amount. Additionally, our platform forms a clean, Ohmic contact with metals, resulting in a robust proximity effect [57]. This enables the incorporation of superconductive Josephson physics within the caloritronic framework with relative ease.
To measure the electron-phonon interaction, we use a superconductor-normal metal-superconductor (S-N-S)[2] Josephson junction (JJ) as an electronic thermometer to monitor the equilibrium electron temperature. Similarly, we apply constant heating power to the structure. By repeating this measurement at different temperatures of the phonon bath, we can determine the electron-phonon interaction using a power law fit of T^n as described in Wellstood et al. [25].

5.2 Device layout

The device fabrication followed the details given in chapter 3, using an InAsOI with a two-dimensional charge carrier concentration (extracted by room-temperature Hall measurements) of $n_{2D} = (1.20 \pm 0.02) \times 10^{12}$ cm^{-2}. The result of the fabrication process is shown in Fig. 5.1(a), where the Joule heaters (in red) and the JJ leads (in blue) are visible.
The InAs mesa (in yellow) is ~ 20 μm long and ~ 6 μm wide. The distance between the Joule heaters (in red) is ~ 17 μm, and the separation between the leads of the JJ is ~ 550 nm (in blue). The grey contacts were used to attempt another type of thermometry

[1] F. Giazotto, G. De Simoni, L. Sorba, A. Paghi, O. Arif, and C. Puglia, "Josephson Junction and superconductor field effect transistor", Filling number: 102024000008983 (19/04/2024)

[2] As shown in [58], the behavior of the n-doped InAs layer in the InAsOI heterostructure is effectively that of a normal metal with respect to Josephson physics; however, its semiconductive nature preserves the gating capabilities.

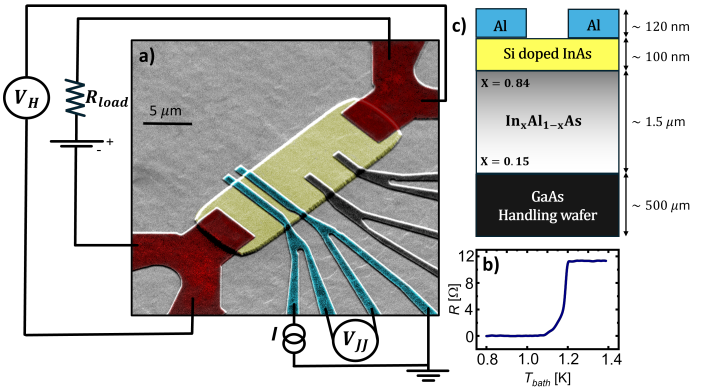


Figure 5.1: **(a)**: Scanning electron micrograph of a representative sample from this study showing the wiring used for measurements. The red contacts represent the Joule heaters; the blue contacts are the leads of the Josephson junction, separated by approximately 550 nm; and the yellow area indicates the InAs mesa. **(b)**: Resistance as a function of the temperature of the Josephson junction in device 1. **(c)**: Diagram of the InAsOI heterostructure used, with the thickness of each layer shown on the right.

technique based on the zero-bias anomaly at the contact between a superconductor and a disordered semiconductor [59, 60]. However, this thermometer was overly sensitive to even minor magnetic field fluctuations, making this approach unstable and impractical. As a result, these contacts are not used in the results presented in this work.

5.3 Thermometers calibration

The devices were wired as shown in Fig. 5.1(a) and cooled in a cryogen-free dilution refrigerator to reach the superconducting temperature for Al. Figure 5.1(b) shows the resistance of JJ (R) as a function of the bath temperature (T_{bath}). It can be seen that the critical temperature of the JJ is $T_c \simeq 1.2$ K, which is approximately equal to the Al one $T_c^{Al} = 1.196$ K [57, 61]. This originates from

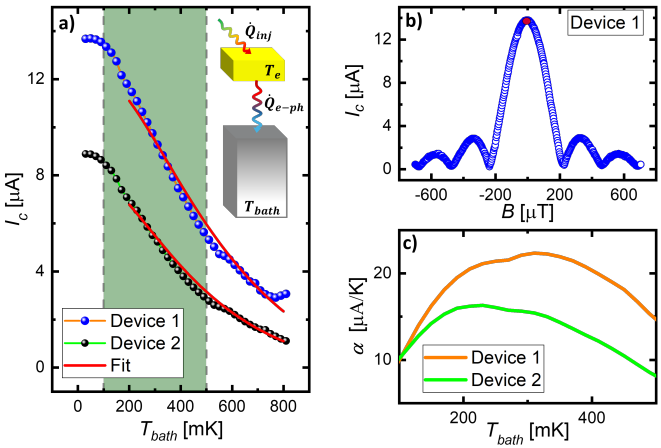


FIGURE 5.2: **(a)**: Critical current (I_c) of the Josephson junction as a function of bath temperature T_{bath} for both devices. The red lines best fit Eq.5.1 for both devices. The green-shaded area highlights the region used for the thermometer calibration. The inset shows a scheme of the predominant heat currents flowing through the InAsOI system: $\dot{Q}_{inj}$ is the injected power from the Joule heaters, whereas $\dot{Q}_{e-ph}$ represents the power dissipated to the substrate lattice phonons residing at the temperature of the cryostat. **(b)**: I_c as a function of the out-of-plane magnetic field (Fraunhofer-like pattern) of device 1 taken at $T_{bath} = 30$mK. The red dot in the panel indicates the critical current value used for the temperature calibration curves of the thermometer in panel **(a)**. **(c)**: Temperature responsivity $\alpha = |\partial I_C/\partial T_{bath}|$ (absolute value of the first derivative of the curves in **(a)**) of the Josephson thermometers, as a function of T_{bath} for both devices.

a very good proximitization stemming from the InAs Fermi level pinning above the conduction band when interfaced with a metal [62, 63] and from the high doping of InAs, which makes it a degenerate semiconductor.

Figure 5.2(a) shows the measured critical current I_c as a function of T_{bath} for the two samples considered in this study. These measurements are taken with the heaters off (so we assume that $T_{bath} = T_e$), and while T_{bath} is changed, the critical current of the JJ is measured.

These represent the cornerstone characteristics of this work, as they provide the calibration curves for the thermometers used to probe the InAs electronic temperature T_e locally. To gain some insight into the effective length of the junctions, the curves in Fig. 5.2(a) were fitted using the model for the critical current of a long diffusive JJ in the high-temperature regime, so considering only the experimental data that satisfy the condition $k_B T \gtrsim 5E_{Th}$ [18]:

$$I_c(T) = \frac{64\pi k_B T}{eR_N} \sum_{n=0}^{\infty} \frac{\sqrt{\frac{2\omega_n}{E_{Th}}}\Delta^2(T)\exp[-\sqrt{\frac{2\omega_n}{E_{Th}}}]}{[\omega_n + \Omega_n + \sqrt{2(\Omega_n^2 + \omega_n\Omega_n)}]^2}, \tag{5.1}$$

where E_{Th} is the junction Thouless energy left as the only fitting parameter, k_B the Boltzmann constant, R_N the normal-state resistance of the JJ, $\Delta(T) = 1.764 k_B T_c \tanh[1.74\sqrt{(T_c/T)-1}]$ is the temperature-dependent superconducting energy gap, $\omega_n = (2n+1)\pi k_B T$, and $\Omega_n = \sqrt{\omega_n^2 + \Delta^2(T)}$ are the Matsubara frequencies. The result of the fit is $E_{th_1} = 4.7 \cdot 10^{-24}$J and $E_{th_2} = 3.5 \cdot 10^{-24}$J for device 1 and 2, respectively. On the other hand, $E_{Th} = \hbar D/L^2$ [64], where L is the length of the JJ, $D = l_e v_F/3$ is the 3-dimensional diffusion coefficient, l_e is the electron mean free path, and v_F is the Fermi velocity. So, one can find the effective lengths of the JJs via the fitted $E_{th_{1,2}}$, obtaining $L_1 \simeq 1.43$ μm and $L_2 \simeq 1.71$ μm for devices 1 and 2, respectively. The discrepancy with the nominal length of the JJs, which is ~ 550 nm, has to be ascribed to the diffusive behavior of the InAsOI platform. Indeed, the length extracted by the fits might be taken as an effective length over which the correlated electrons forming Cooper pairs can travel from one lead to another. Moreover, note that the critical current values and the quality of the fitting curves for device 2 and device 1 differ significantly. This can be attributed to the imperfect equality of the JJs due to the small differences that may arise during fabrication. In particular, the passivation step and the contact definition via EBL may not yield identical results, leading to devices with slightly different properties.

The optimal operating region for the thermometer is the green-shaded area in Fig. 5.2(a), ranging from 100 mK to 500 mK. This region is optimal because the curve has a quasi-linear slope, enabling a reliable numerical conversion between I_c and T_e. In other regions, the curve flattens, making it less suitable for defining the conversion from I_c to T_e.

5.3.1 Behavior of the thermometers in a magnetic field and temperature sensitivity

Figure 5.2(b) shows the Fraunhofer-like interference pattern of one of the JJs, which is constructed by measuring the I_c of the JJ vs the out-of-plane magnetic field (B). This pattern demonstrates the coherence of the Josephson effect [65, 66] and the ability to adjust the JJ's critical supercurrent with an external magnetic field. The red spot in Fig. 5.2(b) indicates the optimal magnetic field working point, around $B \sim 0$ T, for the calibration curves shown in Fig. 5.2(a). This specific magnetic field value was selected to achieve a higher I_c, resulting in a more significant response from the Josephson thermometer.

Figure 5.2(c) shows the computed thermometer responsivity $\alpha = |\partial I_C/\partial T_{bath}|$ as a function of T_{bath}. This parameter represents the slope of the curves in Fig. 5.2(a), measuring the degree of sensitivity of the thermometer to temperature variations. We can evaluate the Noise Equivalent Temperature (NET) (i.e., temperature sensitivity) of our thermometers as $NET = \sqrt{S_I}/\alpha$ [67] where the noise spectral density of the detected switching current I_C can be evaluated as $S_I = (\delta I_C)^2/Bw$ with $\delta I_C \simeq 30$ nA being the experimental uncertainty of the switching current and $Bw \simeq 300$ Hz being the bandwidth of our setup. Using this estimation, one finds $NET \simeq 100 - 200\ \mu\text{K}/\sqrt{\text{Hz}}$ throughout the temperature range studied. This NET is comparable with state-of-the-art devices [32, 67], making this platform attractive as a building block for

calorimetric measurements and single photon detection [68–71].

5.4 Energy relaxation experiment

In this section, we present the results of the experiment and the theoretical phenomenological model used to interpret the data.

5.4.1 Phenomenological model

The inset displayed in Fig. 5.2(a) shows the scheme of the predominant incoming and outgoing heat currents for the InAs mesa. The input power $\dot{Q}_{inj}$ is supplied by the Joule heaters, and the outgoing heat current $\dot{Q}_{e-ph}$ represents the power relaxing in the InAlAs insulating buffer layer due to the electron-phonon interaction. We assume that the power leakage through the contacts (i.e., the Joule heaters, the JJ, and the other two unused contacts) on the InAs mesa is negligible because all those contacts are superconductors that behave, at low energy, as almost ideal Andreev mirrors. This is valid since the electron temperatures explored throughout all measurements are in the limit $k_B T_e \ll \Delta_{Al}$, where k_B is the Boltzmann constant and $\Delta_{Al} \simeq 180$ μeV [10]. In our analysis, we also assume that there is negligible electronic heat loss through the electrically insulating InAslAs buffer (with substrate resistance > 10 TΩ) and that the InAs lattice phonons are thermalized at the cryostat bath temperature T_{bath} as well as the rest of the heterostructure due to the vanishing Kapitza resistance. Under these assumptions, we can write down the power balance equation for the InAs mesa in the stationary regime:

$$\dot{Q}_{inj} - \dot{Q}_{e-ph} = 0, \tag{5.2}$$

where $Q_{inj} = I_H V_H$, and I_H and V_H are the current and voltage drop across the Joule heaters in the InAs mesa. The dissipated power due to the e-ph interaction can be written as [25, 56, 72, 73]:

$$\dot{Q}_{e-ph} = \Sigma V (T_e^n - T_{bath}^n), \tag{5.3}$$

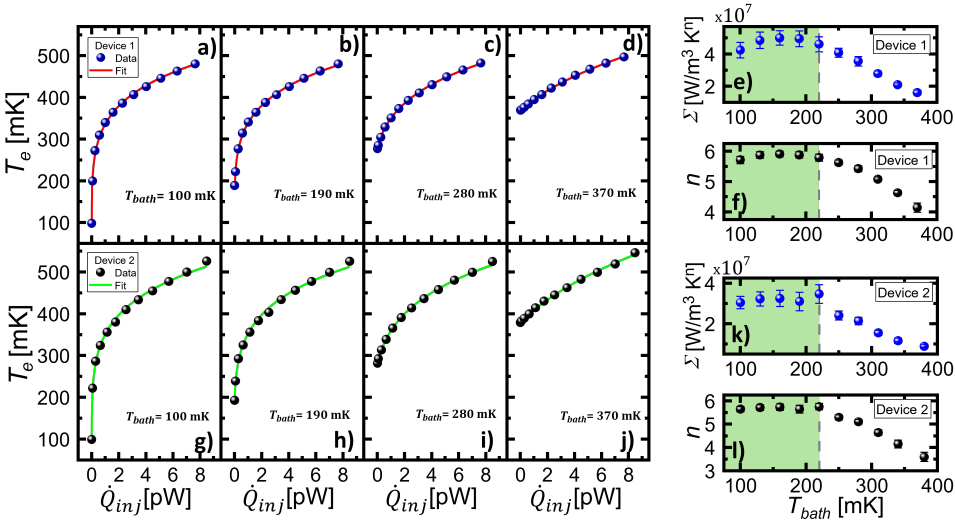


FIGURE 5.3: **(a)-(d)**: Experimental data and the fit using Eq.5.4 are shown at selected bath temperatures (indicated in each panel) for the electronic temperature T_e as a function of the injected power $\dot{Q}_{inj}$ for device 1. **(e)**,**(f)**: The value of Σ and n extracted from the fitting procedure as a function of T_{bath} for device 1. **(g)-(j)**: Experimental data and the fit using Eq.5.4 are shown at selected bath temperatures (indicated in each panel) for the electronic temperature T_e as a function of the injected power $\dot{Q}_{inj}$ for device 2. **(k)**,**(l)**: The value of Σ and n extracted from the fitting procedure as a function of T_{bath} for device 2.

where V represents the geometric volume of the InAs mesa, assumed to be uniformly thermalized, Σ is the electron-phonon coupling constant that we aim to derive, and n is the exponent of this power law. Typically, $n = 5$ for thin metallic films [25]. However, both experimental evidence [72] and theoretical predictions [31, 32] indicate that this value can vary depending on the specific material and the regime, such as ballistic or diffusive. The electron-phonon heat losses of highly doped InAs have been studied since the 1970s [54]. Initially, it was predicted that the couplings would be very

low. Early estimations predicted that at extremely low temperatures (sub-Kelvin), the temperature dependencies would be very low and quasi-linear, approximately $n \approx 1$. However, a later study [55] found different values of n, specifically $n = 5$ and $n = 7$, for highly doped GaAs, related to piezoelectric coupling and the deformation potential, respectively. The disorder can lead to changes in the power-law behavior in metals, with values of n ranging from 4 to 6 [31]. For these reasons, we opted to treat n as a free-fitting parameter for the variability. Using Eqs.5.2 and 5.3, we can express:

$$T_e = \sqrt[n]{\frac{\dot{Q}_{inj}}{\Sigma V} + T_{bath}^n}, \tag{5.4}$$

where Σ and n are fitting parameters of the dependence on $\dot{Q}_{inj}$ and T_{bath}.
By keeping the bath temperature T_{bath} constant and adjusting the injected heat flux $\dot{Q}_{inj}$, we can measure the electronic temperature T_e in the InAs mesa to extract the energy relaxation curve inside the InAs.

5.4.2 Experimental results

Figures 5.3(a-d) and (g-j) show selected curves for different bath temperatures for the two samples studied. These curves were then fitted with Eq.5.4, and the results for the fitting parameters Σ and n are resumed in Figs.5.3(e,f) and (k,l). The agreement between theory and experiment is evident through the reduced chi-square χ^2_{red}, with the worst value approximately $\chi^2_{red} \simeq 1.1 \cdot 10^{-4}$.
In Fig. 5.3(e,k), the electron-phonon coupling constant Σ, similarly to the exponent n, is shown to be almost constant in the green shaded region, ranging from 100mK to 220mK. The values are $\Sigma = (4.2 \pm 0.4) \cdot 10^7$ W/(m^{3}K^n) and $\Sigma = (3.0 \pm 0.3) \cdot 10^7$ W/(m^{3}K^n) for devices 1 and 2, respectively. These values are notably low compared to those of other common metals [32] such as copper

[Cu, $\Sigma_{Cu} \simeq 2 \cdot 10^9$ W/(m^{3}K^5)] [74], aluminum [Al, $\Sigma_{Al} \simeq 0.2 \cdot 10^9$ W/(m^{3}K^5)] [74], aluminum manganese [AlMn, $\Sigma_{AlMn} \simeq 4.5 \cdot 10^9$ W/(m^{3}K^6)] [75–77], doped silicon on insulator [SOI, $\Sigma_{SOI} \simeq 0.1 \cdot 10^9$ W/(m^{3}K^5)] [78], and InAs nano-wires [$\Sigma_{InAsNW} \simeq 4.7 \cdot 10^9$ W/(m^{3}K^5)] [79].
Looking at Figs.5.3(f,l), we can see that the value of the exponent n in the green shaded region from 100mK to 220mK remains almost constant ($n = 5.84 \pm 0.14$ for device 1, $n = 5.72 \pm 0.12$ for device 2). Once again, having a value of n greater than 5 means that phonon losses are even smaller at low temperatures, indicating that the InAsOI platform is well-suited for coherent caloritronics.
The properties mentioned above of InAsOI make it an excellent choice for caloritronic applications because of the minimal interaction between electrons and lattice phonons. The low electron-phonon coupling allows the electronic temperature to be significantly altered with minimal power input, resulting in a more stable and controllable caloritronic technology with reduced phonon losses. The low values of the parameter Σ compared to those in metals may be due to the lower electron carrier density. However, it is important to note that the main physical mechanism responsible for these properties has not been definitively identified. This is largely due to the limited knowledge of other physical parameters required to calculate the electron-phonon coupling for this specific layered material.

5.5 Comparison with other commonly used materials

It is important to note that the electron-phonon coupling constants Σ of different materials have different physical dimensions due to the different power law exponent n. In Fig. 5.4, we compare the electronic temperature as a function of the injected power for different materials. The curve for our InAsOI device 1 is shown at a

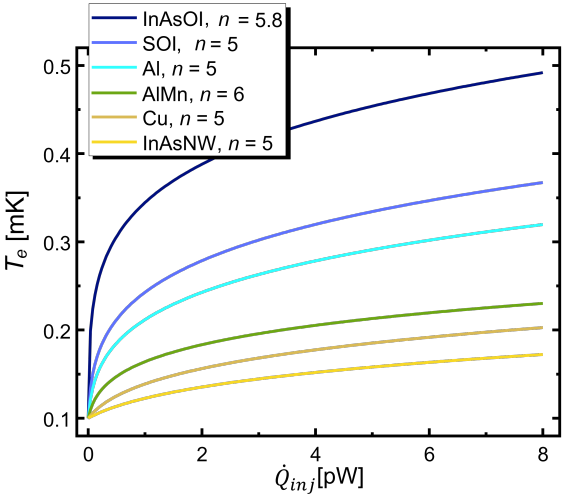


Figure 5.4: Comparison of the electronic temperature as a function of the injected power for different materials (as indicated in the legend) at a bath temperature of $T_{bath} = 100$mK. The curve for InAsOI represents the fitted data obtained for device 1. In contrast, the curves for the other materials were calculated using literature values for Σ and n (SOI [78], Al [74], AlMn [76], Cu [74], and InAsNW [79]), applying Eq.5.4 with the same volume as our InAs mesa.

bath temperature of 100 mK. For other materials, we calculated theoretical curves using Eq.5.4, with the same volume for the InAs mesa and $T_{bath} = 100$ mK. This approach eliminates variations in the physical dimensions for Σ and n. It allows us to observe that the increase of T_e in our InAsOI is significantly greater compared to other common materials when the same power is applied to the structure. Although the change in electron temperature may seem small in absolute value, due to the power-law scaling, it corresponds to differences in Σ of orders of magnitude. For example, comparing the lines for Al (cyan) with Cu (light brown), there is a difference of more than an order of magnitude in Σ. The expected electronic

temperature variation for InAsOI is much higher than that of all other metallic materials. This supports our conclusion that there is a very weak electron-phonon coupling, maintaining good quality of the Josephson junction [57].

5.6 Further considerations on the model

In the study of III-V materials at low temperatures (i.e., $T < 1$ K), it was initially expected that the power exponent n would be 5 due to piezoelectric coupling [55]. However, our research found that for $T_{bath} < 220$ mK, n exceeded 5, approaching 6. This observation deviates from the predicted value due to certain conditions, specifically in the dirty limit, where the mean free path of the electron l_e is much smaller than the wavelength of the phonon λ_{ph}, and power dependencies such as T^6 are predicted to occur [31]. For our specific case, we calculated l_e to be approximately 178 nm using equation $l_e = \mu v_F m^*/e$, where v_F is the Fermi velocity, $m^* = 0.023$ is the effective mass of InAs, $\mu = 4970$ cm^2/(V·s) is the mobility of electrons and e is the charge of electrons. Additionally, we determined that the phonon wavelength is $\lambda_{ph} = hv_S/(k_B T_{bath}) \simeq 1$ μm for $T_{bath} = 200$ mK, where h is the Planck constant, k_B is the Boltzmann constant and $v_S \simeq 4.2 \cdot 10^3$ m/s is the sound velocity in InAs [80]. These calculations indicate that our devices operate in the dirty limit, where $l_e \ll \lambda_{ph}$, potentially contributing to the observed value of n exceeding 5. Nevertheless, the underlined reasons for the small Σ and high n values remain unclear.

The values of Σ and n show another unexpected feature: in Fig. 5.3(e,f)-(k,l), it is evident that both parameters start to decay for $T_{bath} > 220$ mK. This behavior can be explained by considering the length of the electron-phonon scattering, L_{e-ph}. This length can be estimated as $L_{e-ph} = \sqrt{D\tau_{e-ph}}$, where τ_{e-ph} is the electron-phonon scattering time calculated using the relation $\tau_{e-ph} = C/G_{th}$. Here, $C = \gamma V T_e$ is the thermal capacitance of the electron gas, γ is the

Sommerfeld constant, where $\gamma = \pi^2 n_{3D} k_B / 2T_F$, $T_F = E_F/k_B$ is the Fermi temperature, $E_F = (\hbar^2/2m^*)(3\pi^2 n_{3D})^{2/3}$ is the Fermi energy and $G_{th} = \partial \dot{Q}_{e-ph}/\partial T_e = n\Sigma V T_e^{n-1}$ is the thermal conductance of the electron gas. When we calculate L_{e-ph} using these parameters, we find:

$$L_{e-ph} = \sqrt{\frac{\pi^2 k_B^2}{\hbar^2} \frac{m^* n_{3D}^{1/3}}{(3\pi^2)^{2/3}} \frac{v_F l_e}{3n\Sigma T_e^{n-2}}}. \tag{5.5}$$

The value L_{e-ph} measures the distance over which one can assume a constant electronic temperature. When using the values of Σ and n found in the 100-220 mK region, this distance becomes shorter than 20μm (which is the longitudinal dimension of the InAs mesa) when $T_e \simeq 380$ mK. This could make our model unreliable for fitting the data at higher temperatures, and the decay of Σ and n could be ascribed to this.

5.7 Final consideration on InAsOI

The performance of electron-phonon coupling, compared to metals such as chromium (Cr) [72], copper (Cu) [81] or gold-palladium (AuPd) [82], is remarkably good with values of $\Sigma \simeq 3 \cdot 10^7$ W/(m^{3}K^n) and $n \simeq 5.8$. Looking at other semiconductors [55, 79] the comparison is encouraging because of the low electron-phonon interaction of the platform and the potential to implement effects such as superconducting proximitization and Josephson coupling, which are hardly feasible in materials such as Si [73, 83]. This makes the platform an ideal candidate for all coherent caloritronics experiments [72, 84–86], as well as single-photon detection and bolometry [68–71, 87]. Furthermore, the semiconductive nature of InAsOI allows for modifying its properties, such as charge density, through external electrostatic gating. This ability, not possible with conventional superconducting metals, presents further opportunities for coherent caloritronics and gateable superconductivity.

Chapter 6

Photonic heat transport

In this chapter, we provide an overview of what has been done so far in photonic heat transport and what we can improve with our InAsOI platform. Moreover, we will give the details of the building blocks of the coupling circuit for photonic heat transport, which we will use in the next chapter.

6.1 Photonic heat transport

Photonic heat transport in superconducting circuits is a well-studied phenomenon that has been investigated in numerous works over the past few decades [72, 82, 88–91]. This phenomenon arises due to the correspondence of Johnson-Nyquist noise and black body radiation when two resistive reservoirs at different temperatures are coupled with an electrical circuit [34, 35].

6.1.1 Brief state of the art

So far, the photonic thermal transport has been investigated in different forms. In particular, the possibility of tuning the heat flow was studied both theoretically [92–96] and experimentally [72, 82, 88]. This feature is implemented by introducing a coupling

inductor $Z_c(\omega)$ that depends on an external controllable parameter, such as a magnetic or electric field. For example in [82] this possibility was exploited via the introduction of a superconducting quantum interference device (SQUID) which can change with an external magnetic field its inductive impedance $Z_c = L_J \simeq \hbar/(2eI_S)$ where $I_S \simeq I_{S0}|\cos(\pi\phi/\phi_0)|$ is the critical current of the SQUID, I_{S0} is the critical current in absence of magnetic field and ϕ is the magnetic flux piercing the SQUID loop. In this work, the authors experimentally demonstrated that introducing a tunable impedance enables manipulation of radiative heat transfer processes, confirming theoretical predictions. As a figure of merit for heat transfer manipulation, the authors monitored the temperature of the cold reservoir as the magnetic field varied. They recorded variations of up to ~ 5 mK. Subsequent works again demonstrated the possibility of exploiting heat transfer manipulation via an external magnetic field [72, 90, 97]; however, [88] demonstrated for the first time that an electrostatic field could also be used to manipulate radiative heat transfer processes. This was achieved by introducing a coulombic metallic island, whose impedance can be periodically altered via an external electrostatic gate. The authors showed that they could change the temperature of the cold reservoir by up to ~ 2 mK.

6.1.2 What can we improve?

Our idea is to exploit the properties of the InAsOI platform to improve the performance of this class of devices. Basically, this platform has two main and obvious advantages over what was tried in the literature:

- The e-ph coupling is very low compared to that of the metallic materials often used in caloritronics. This provides a clear advantage in the realisation of the reservoirs, as the heated electrons will lose less energy to the phononic bath. In principle, this can lead to better temperature modulations and will enhance the thermal signal-to-noise ratio.

- The semiconductive nature of InAsOI guarantees the possibility of introducing an electric field-dependent Z_c that can be tuned with a scalable and straightforward top-gate architecture.

The first advantage mentioned can be realised by fabricating InAs mesas that will serve as resistive reservoirs. Compared with the metallic resistive reservoirs used in previous experiments, our reservoirs will have a significantly lower e-ph coupling as pointed out in section 5.5 the low e-ph coupling comes with no effort as a property of the platform, avoiding energy losses of the electrons through the lattice phonons, hence enhancing the resulting electronic temperature when a power is injected.
The second advantage can be exploited by introducing a circuit element whose impedance is affected by an external electric field. A clear candidate with these properties is the Josephson field-effect transistor (JoFET), which, in our case, is made from a semiconductive JJ with a top gate over the semiconductive weak link. Following the results in [5], these structures have the property to change their critical current I_c with the electric field applied, and, thanks to the relation $L_J = \hbar/(2eI_S)$ it turns out that the impedance of this architecture will result in a function of the gate voltage applied (The JoFET details and properties will be treated in the next section).
Together, these advantages may lead to a structure with better temperature modulation and simpler and more scalable control. The top-gate architecture is indeed much simpler than introducing a Coulomb island, as done in previous work, and is clearly more scalable than using external magnetic fields.
Another unexploited possibility of photonic transport is the non-galvanic coupling between reservoirs. All previous work included a coupling circuit that establishes galvanic contact between the two reservoirs. If we think that photonic heat transport has a precise application in on-chip energy harvesting and manipulation, this galvanic contact may, on occasion, lead to undesired quasiparticle transport. This can be avoided by interrupting the coupling circuit with capacitors. Photonic transport does not need galvanic contact and therefore, the introduction of capacitors in the coupling circuit,

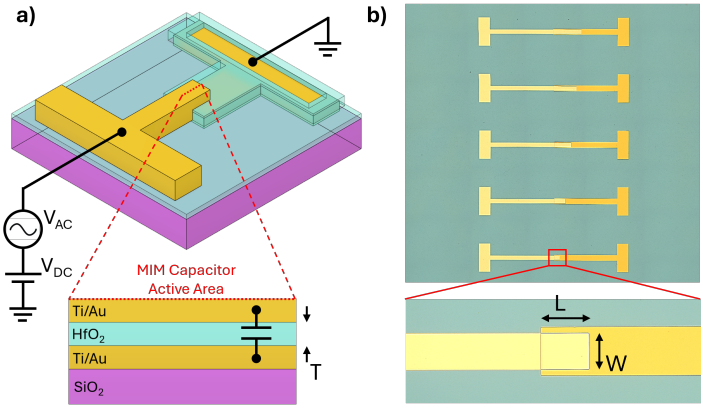


Figure 6.1: **(a)**: 3D sketch of a MIM capacitor with. The inset shows a section of the capacitor's active area. **(b)**: Optical microscope image of one of the measured chips featuring capacitors with different areas.

in principle, will not affect heat transport once they are included in the calculation of the coupling coefficient $\tau(\omega)$.

6.2 Field effect control of photonic heat transport: building blocks

In this section, we will provide details on the building blocks of our coupling circuit. As mentioned before, we will exploit the non-galvanic contact between the reservoirs; hence, the realization of capacitors will be fundamental. Moreover, the gate dielectric for the top-gate architecture and the JoFET element will be discussed, as they will be crucial to our experiment.

6.2.1 Gate dielectric characterization and planar capacitors

Here, we provide useful parameters for HfO_2, which will be used both as the top-gate insulating layer and as the dielectric layer ofcapacitors', as mentioned before in chapter 3.
To characterize the performance of HfO_2, we start by creating planar *metal-insulator-metal* (MIM) capacitors as shown in Fig. 6.1 (a). The capacitors are made of two metallic Ti/Au layers with thicknesses of 10/40 nm, separated by a 30 nm-thick HfO_2 insulating layer grown by ALD at 130°C. As is visible in Fig. 6.1 (b), the area of the capacitors can be decided depending on the superposition of the top and bottom metallic layers. Once the capacitors are wired, we can measure their impedance (magnitude and phase) in the frequency range from 100Hz to 100kHz using an LCR meter (Precision LCR meter HP 4284A), which applies a sinusoidal voltage signal with 250 mV_{rms} amplitude. This was done in an experimental setup where the cold coaxial, RC and π filters were removed to avoid cutoffs below 100 kHz. From the impedance characteristics, we will infer the relevant parameters of HfO_2, taking measurements at both room and cryogenic temperatures for completeness. Using a lumped element model where the impedance is purely capacitive $Z = 1/(2\pi fC)$ where f is the frequency of the AC oscillation of the probe, we can obtain the capacitance values from the Bode diagrams in Fig. 6.2 (a) and then fit them to obtain the relative permittivity with the model:

$$C = \epsilon_0 k \frac{A}{t}, \tag{6.1}$$

where ϵ_0 is the vacuum permittivity, k is the relative permittivity, A is the capacitor area, and t is the dielectric thickness. The results are shown in Fig. 6.2 (b) for both room temperature and cryogenic temperature, and the extracted relative permittivity k is 17.9 and 16.5, respectively, for 300 K and 3 K. This data allows us to efficiently design the capacitance of the coupling capacitors that we will use in our coupling circuit for the realization of non-galvanic photonic heat transport.

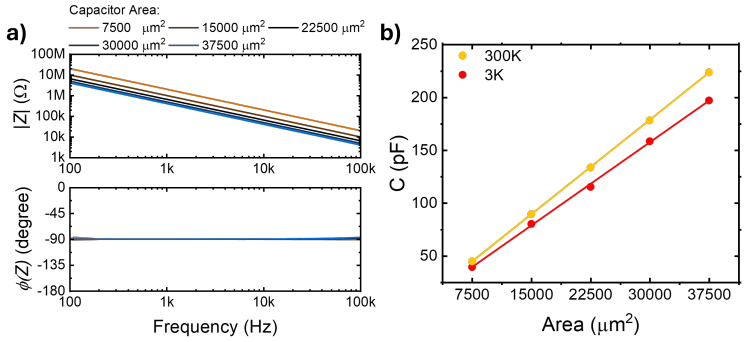


Figure 6.2: **(a)**: Bode diagram with magnitude $|Z|$ and phase $\phi(Z)$ of the impedance of the capacitors as a function of the frequency measured at room temperature. **(b)**: Data points and linear fit of capacitance C as a function of the area of the capacitor measured at room temperature (300K) and at cryogenic temperature (3K).

Since, for simplicity, the same dielectric will also be used for the insulating layer of the top gate structure, another crucial feature of our HfO_2 is its breakdown field E_{BD}. This field corresponds to the maximum sustainable electric field before the onset of an undesired avalanche breakdown, which would cause a significant current leak from the gate to the JoFET channel [4]. To determine this number, we measured the current through the test capacitors as a function of the applied voltage ($I - V$ curves) and identified the voltage V_{BD} at which the capacitors exhibit avalanche breakdown. This voltage value is clear to determine because of the abrupt change in the increase in leakage current, from linear growth before the breakdown to exponential dependence afterwards. Using the formula $E_{BD} = -V_{BD}/t$, we finally could extract that our HfO_2 has a breakdown field of ~ 330 MV/m. Knowing this number allows us to determine the voltage values that can be applied to the top gates of our JoFETs without causing undesired changes in leakage current. For example, if we have a thickness of ~ 30 nm, we know that it will be safe to reach -5 V with the gate voltage without worrying about

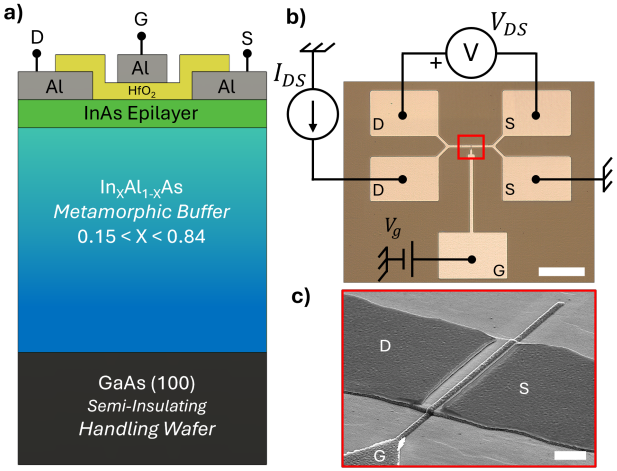


FIGURE 6.3: **(a)**: Sketch of the cross-section structure of a JoFET built on InAsOI. **(b)**: Optical microscope image of the 4-terminal JoFET architecture. The electrical measurement configuration is also shown, with I_{DS} the drain-source current, V_{DS} the voltage drop across the drain-source terminals, and V_g the gate voltage; the scalebar is 100 μm. (c) Tilted-view SEM micrograph of the red inset in panel (b) showing a representative JoFET; the scalebar is 1 μm.

leakage currents or breakdown.

6.2.2 Tunable impedance: JoFETs with InAsOI

Here we will introduce the JoFET element that will be used as electrically tunable impedances $Z_c(\omega, E)$.
As we can see in Fig. 6.3 (a), JoFETs are built using the InAsOI heterostructure previously discussed. The device consists of an SNS JJ, as previously mentioned, with a top-gate structure to apply an electrical field directly to the semiconductive channel. The top gate is implemented by ALD growth of 30 nm of HfO_2 as a dielectric layer, followed by e-beam deposition of 10/100 nm of Ti/Al. A top view of a representative device with the electrical measurement scheme can

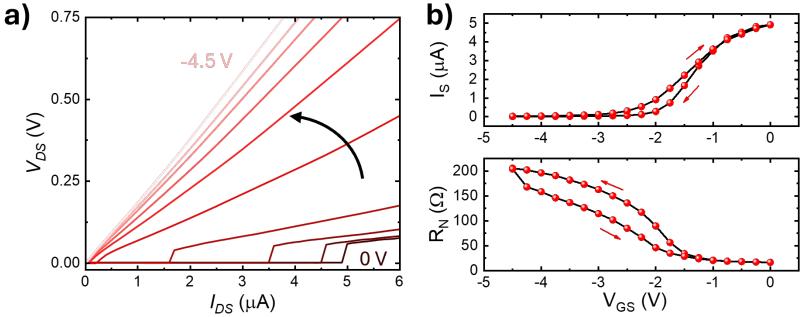


Figure 6.4: **(a)**: V_{DS} vs I_{DS} curves of a representative device measured while lowering the value of V_g from 0 to -4.5 V **(b)**: Switching current I_S as a function of ascending and descending V_g indicated by the arrows. **(c)**: Normal state resistance R_N as a function of ascending and descending V_g indicated by the arrows.

be seen in Fig. 6.3 (b), while a close-up image showing the active part of the JoFET can be seen in Fig. 6.3 (c).

The devices were then measured in the previously described cryogenic measurement setup to evaluate their features and performance. Figure 6.4 (a) shows the $I_{DS} - V_{DS}$ characteristics of a JoFET with an increasing value of $|V_g|$. This measure is taken by injecting an I_{DS} into the JoFET from 0 to 6 and back to 0 μA while recording the voltage drop across the structure. Panels (b) and (c) of this figure show the two main features that we care about when using this kind of structure. Panel (b) shows the dependence of the switching current I_S on V_g. To take this measure, we record the bias current when the voltage drop across the structure deviates from 0, indicating that the JoFET is no longer superconducting and has switched to a normal conducting state (switching current). Figure 6.4 (b) shows that the switching current decreases when lowering the value of V_g and has a hysteretic behavior. This hysteresis is due to the ferroelectric behavior of HfO_2 [4]. The lowering of the critical current follows the depletion of the semiconductive channel

under negative voltage: the charge density within the InAs decreases and the proximity effect, which is responsible for superconductive transport in SNS junctions, becomes progressively weaker. Considering the dependence of Josephson inductance on switching current $L_J = \hbar/2eI_S(V_g)$, we have found an element whose impedance can be efficiently tuned with an external electric field. Due to its scalability, this kind of element can be introduced inside the coupling circuit between the resistive reservoirs as a coupling impedance $Z_C(\omega, E)$ in Fig. 2.8. Moreover, we can see that, independently of the direction of V_g, there always exists a regime where $I_S = 0$ and therefore the JoFET is not superconductive. This gate-driven transition is of fundamental relevance to our purposes as it allows us to significantly alter the inductance of our JoFET with an external electric field. Figure 6.4 (c) shows how gate voltage affects the normal state resistance R_N of JoFET. Each data point is the result of a linear fit of the normal conductive branch of the $I - V$ curves in panel (a) with Ohm's law. We can see that reducing V_g generally increases R_N due to the depletion of the semiconductive InAs channel. A hysteretic trend persists due to the same ferroelectric behavior of the dielectric layer described above.

Chapter 7

Field effect tunable photonic heat transfer

In this chapter, we examine the photonic heat transport between two resistive reservoirs separated by a distance of ~ 1 mm. This macroscopic distance was chosen to highlight the robustness of the platform at macroscopic scales and to avoid spurious substrate-phonon-mediated thermal coupling between the reservoirs. For the first time, we couple two terminals via a non-galvanic electrical circuit, employing a gate-tunable JoFET to manipulate photonic heat transfer. Our results on temperature modulation significantly surpass the current state of the art by more than an order of magnitude [88]. Our device represents a significant advancement for fields such as caloritronics [32, 86, 98–100], thermal and energy manipulation [76, 101], bolometric radiation detection [68–70], and thermal logic gates and memory systems [102–104].

7.1 Explanation of the experiment

The conceptual experimental scheme is illustrated in Fig. 7.1 (a). Two different resistive reservoirs R_{hot}, R_{cold} at different temperatures T_{hot}, T_{cold} are in thermal contact with the phonon bath, which we consider fixed at temperature T_{bath}. If resistors are enclosed in

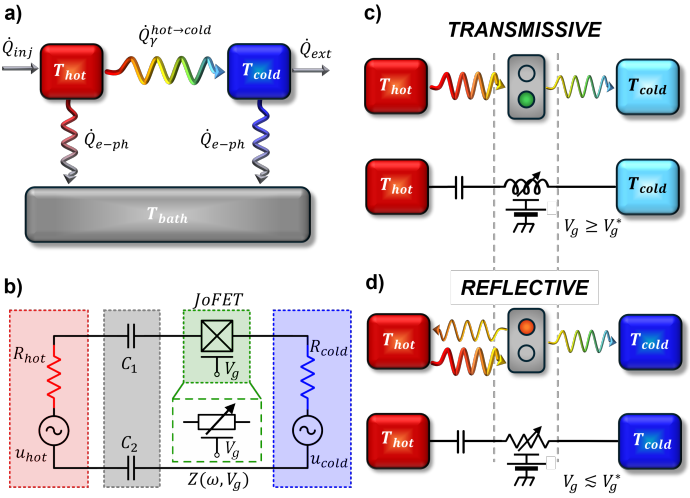


FIGURE 7.1: Schematic representation of the experiment. (a): The following describes the heat balance scheme of the system: $\dot{Q}_{inj}$ represents the injected power into the hot resistor, $\dot{Q}_{e-ph}$ denotes the electron-phonon heat exchange towards the thermal bath, $\dot{Q}_{\gamma}$ indicates the photonic heat current, and $\dot{Q}_{ext}$ refers to other incoming or outgoing parasitic heat currents in the cold resistor. **(b)**: This illustrates a lumped element model of the reservoirs, with the hot one shown in red and the cold one in blue. The coupling circuit includes capacitors $C_{1,2}$, a gate voltage V_g, and the resistances of the two reservoirs, denoted as R_{hot} and R_{cold}. Additionally, $Z(\omega, V_g)$ represents the frequency- and voltage-dependent impedance of the JoFET, while $u_{hot,cold}$ are the two effective Johnson-Nyquist AC voltage sources. **(c,d)**: These panels illustrate the functioning principle of the experiment. The two reservoirs are interconnected by a circuit whose total complex impedance can be adjusted via an external gate voltage V_g. Applying this gate voltage suppresses the superconductivity of the JoFET, leading to a resistive state. When the JoFET is in a superconducting state (c), the impedance is purely *inductive*, allowing for maximum photonic heat transfer through the system (green semaphore). Conversely, when the JoFET transitions to a *resistive* state (d), it creates an impedance mismatch in the coupling circuit, resulting in backreflection of some of the radiation flowing from the hot reservoir (red sempahore).

an electrical circuit, as shown in Fig. 7.1 (b), black-body radiation arising from Johnson-Nyquist thermal noise [34, 35] causes voltage

fluctuations $u_{hot,cold}$ to take place between the *hot* and *cold* sections of the circuit. The introduction of a gate-tunable impedance $Z(\omega, V_g)$, where V_g is the external gate voltage, enables the manipulation of photonic heat conduction. This $Z(\omega, V_g)$ was implemented via a JoFET, which was modeled using the resistively and capacitively shunted Josephson junction model (RCSJ) [105], where Josephson junctions are characterized by an inductance, a resistance, and a capacitance arranged in parallel. The latter can be safely neglected in SSmS junctions. In particular, $Z(\omega, V_g)$ shows two mutually exclusive behaviors: it could act as a resistance $R_J(V_g)$ or as a Josephson inductance $L_J(V_g)$. In fact, when $V_g > V_g^*$, the SSmS element is superconductive with negligible resistance, presenting mainly an inductive component, and when $V_g < V_g^*$, the element is no longer superconductive, presenting mainly a dissipative component.
At low temperatures, since the typical thermal photon wavelength is ($\lambda_\gamma = hc/n_0 k_B T \simeq 3$ cm at $T = 100$ mK, where h is the Planck constant, c the speed of light and $n_{InAs} \sim 4$ the effective refractive index of our heterostructure [106]) is much longer than the characteristic size of the electrical elements, we can neglect their precise geometric design using the standard lumped element approximation. In such a limit, the thermal transport $\dot{Q}_\gamma^{i\to k}$ between two generic reservoirs can be calculated using the scattering formula [36] as seen in chapter 2:

$$\dot{Q}_\gamma^{i\to k} = \int_0^\infty \tau_{ik}(\omega)\hbar\omega[n_i(\omega) - n_k(\omega)]\frac{d\omega}{2\pi}, \tag{7.1}$$

where $n_{i,k}(\omega) = 1/[\exp(\hbar\omega/k_B T_{i,k}) - 1]$ are the Bose-Einstein distributions for the thermal photon population in the reservoirs. Here, the power transmission coefficient $\tau_{ik}(\omega)$ is obtained within the standard circuit approach previously described (see chapter 2). For the two terminal configuration represented in Fig. 7.1 (b), in particular, $\tau_{ik}(\omega) = \frac{4R_i R_k}{|Z_{tot}(\omega)|^2}$, where $Z_{tot}(\omega, V_g)$ is the total series impedance of the circuit and $R_{i,k}$ are the resistances of the reservoirs [36]. By assuming $C_1 = C_2 = C$, it can be approximated with:

$$\tau_{ik}(\omega) \approx \begin{cases} \frac{4R_iR_k}{[R_{hot}+R_{cold}]^2+[\omega L_J(V_g)-\frac{4}{\omega C}]^2} & \text{for} \quad V_g \geq V_g^*, \\ \\ \frac{4R_iR_k}{[R_{hot}+R_{cold}+R_J(V_g)]^2+[-\frac{4}{\omega C}]^2} & \text{for} \quad V_g \lesssim V_g^*, \end{cases} \tag{7.2}$$

The expected behavior of the proposed setup is illustrated in Figs. 7.1 (c,d), where two distinct regimes are depicted for $\dot{Q}_{\gamma}^{hot\rightarrow cold}$. The case of the *transmissive* photonic channel (Fig. 7.1 (c)) is realized when the JoFET shows an inductive behavior: the impedance matching of the coupling circuit is optimal and the heat transfer due to the photonic current is maximum. The coupling circuit is conceptually depicted as a green semaphore in this case. By contrast, the *reflective* photonic channel case (Fig. 7.1 (d)) is realized when the JoFET acts as a resistor, the impedance mismatch worsens, and the coupling circuit reduces radiative heat transfer. The coupling circuit is therefore conceptually depicted as a red semaphore.

7.2 Device and experimental setup

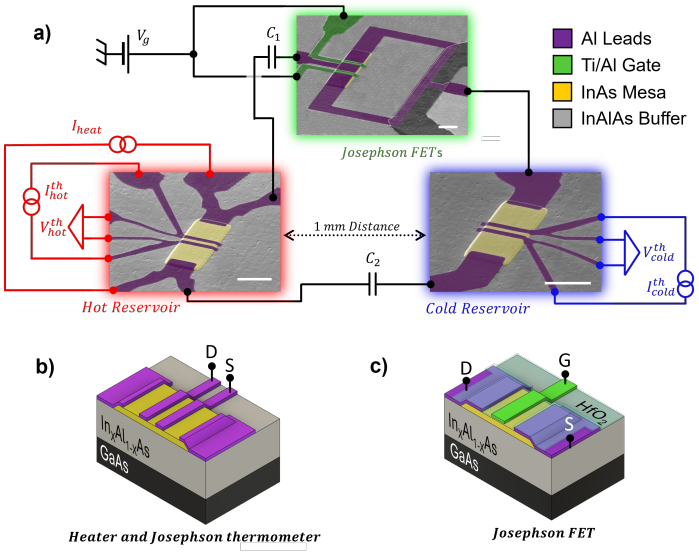


FIGURE 7.2: Structure and wiring of the gate-tunable photonic heat transfer experiment. (a): Schematic circuit including SEM photographs (the white scale bars in those photos are 5 μm) of the devices integrated on the InAsOI platform, wiring, and supply/measurement setup. Red- and blue-shaded SEM images show the hot and cold resistors, respectively, equipped with JJ thermometers. The green-shaded SEM image shows the gate-tunable photonic heat modulator, achieved by using two JoFETs connected in parallel and driven simultaneously. The ring-like configuration realizes a superconducting interferometer (SQUID). The hot and cold resistors are non-galvanically connected via the two capacitors. Red and blue wiring and schematics refer to the supply/measurement setups of the hot and cold reservoirs, respectively. **(b)**: 3D representation of the hot and cold resistors equipped with the Josephson thermometer. The two Al fingers in the middle define the SSmS JJ used to measure the electronic temperature. At the same time, the lateral Al leads connect the InAs mesa to the rest of the circuit and also provide the heating current. **(c)**: 3D representation of a single JoFET. The superconducting source and drain leads on the side define the SSmS junction, with the InAs mesa patterned on the electrical insulating substrate. The gate finger in the middle is non-galvanically connected to the InAs channel via the HfO_2 insulating layer. It is used to tune the electron density of the InAs channel, thereby affecting the photonic heat transfer.

The device fabrication followed the details given in chapter 3, using an InAsOI with a two-dimensional charge carrier concentration (extracted by room-temperature Hall measurements) of $n_{2D} = (1.20 \pm 0.02) \times 10^{12}$ cm^{-2}. The metamorphic InAlAs buffer behaves as an electrical insulator at cryogenic temperatures. InAsOI interfaces very well with superconductors due to the lack of a Schottky barrier at contact with the metal, allowing us to create SSmS JJs and JoFETs [5, 58].

Figure 7.2 (a) illustrates the structure and wiring of the fabricated circuit, accompanied by scanning electron microscopy photographs of the fabricated devices. The chip employs three InAs mesas, highlighted in yellow. The InAs mesas were defined via selective wet etching of the excess InAs epilayer and electrically decoupled by the electrical insulating behavior of the InAlAs metamorphic buffer at cryogenic temperatures, here depicted in gray. The superconducting Al leads, along with the signal lines, are delineated in violet, whereas the Ti/Al gate lines are distinguished by green coloring. Gate lines are electrically isolated from signal traces by a 31-nm-thick HfO_2 insulating layer deposited by ALD.

The InAs mesas were configured in two different arrangements: hot and cold resistive thermal reservoirs equipped with heaters and Josephson thermometers (red and blue photographs in Fig. 7.2 (a), schematized in Fig. 7.2 (b)) and a voltage-controlled JoFET used as a thermal current modulator (green photograph in Fig. 7.2 (a), schematized in Fig. 7.2 (c)). The resistive reservoirs (10 μm long, 5 μm wide) are macroscopically spaced 1 mm apart on the chip. The value of their resistances was measured to be $R_{hot} = R_{cold} = 360 \pm 10$ Ω. Both reservoirs were equipped with Josephson thermometers (violet source (S) and drain (D) contacts in Fig. 7.2 (b)) for the purpose of monitoring their electronic temperature, evaluated by measuring the temperature-sensitive switching supercurrent of the SSmS JJs defined between the Al superconducting fingers positioned in the middle of the InAs mesas. The inter-finger distances defining the JJ lengths are 450 nm and 550 nm for the hot and cold reservoirs, respectively, to get different sensitivity ranges in the electronic temperature

(see section 7.4 for more information on thermometric calibrations).

The temperature measurement is performed by supplying a current $I^{th}_{hot,cold}$ to drive the JJ junction, while the voltage drop across it $V^{th}_{hot,cold}$ was measured to identify the switching current and convert it by calibration to the JJ electron temperatures. It is essential to note that the temperature measurements on the mesas were conducted non-simultaneously to mitigate potential thermal disturbances to the system arising from switching Josephson thermometers.

The external control of the electronic temperature of the heated hot resistor is obtained by providing an additional external current I_{heat} directly injected from two additional Al lines, inducing Joule heating $\dot{Q}_{inj} = R_{hot} I^2_{heat}$ directly within the InAs mesa. This current is supplied by an externally floating current generator that is electrically isolated from other sources to prevent the occurrence of unintended ground loops.

Incorporation of components C_1 and C_2 is essential to achieve direct current (DC) isolation between the heating circuit and the cold reservoir. Indeed, they ensure galvanic isolation between the two reservoirs. These components have been strategically integrated between the hot and cold resistive reservoirs, as well as between the hot resistive reservoir and the JoFET, to complete the circuit configuration. Each capacitor consists of a series configuration of two identical metal-insulator-metal parallel-plate capacitors, with Al electrodes (area of 130 μm^2) separated by the HfO_2 insulator, resulting in an inter-electrode distance of 31 nm. The design anticipates a capacitance $C_1 = C_2 = C$ of $\simeq 70$ pF [4].

In contrast to the simplified scheme illustrated in Fig. 7.1 (b), in the actual setup, the voltage-tunable electrical impedance used as the thermal transport modulator is realized using two nominally identical JoFETs implementing an SSmS superconducting quantum interference device (SQUID) equipped with a superconducting flux line. However, it was determined that the magnetic field-induced inductance variation exhibited an insignificant effect on the transmission coefficient τ_{ik} (refer to the discussion in appendix A) as a result

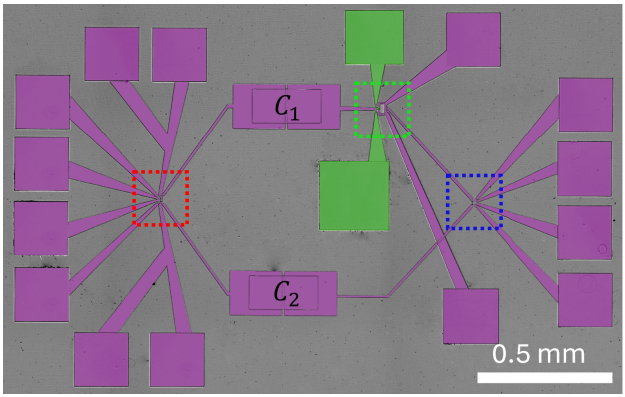


FIGURE 7.3: Top view of a representative sample. False color optical microscope top view of the device. In purple, the superconducting Al structures, in green, the top gate structures, and in grey, the InAlAs metamorphic layer. The two capacitors used $C_{1,2}$ are also visible. Each of those capacitors is the resultant of a series of two planar metal-insulator-metal (Al-HfO_2-Al) capacitors.

of the excessively large screening parameter of the SQUID. Consequently, a common gate voltage V_g was applied to both JoFETs, which operate practically as a single JoFET element, having the sole mechanism of regulating photonic heat transport. The adopted InAs mesa is 15 μm long, 5 μm wide, with a 4 μm separation between the two JoFETs. The interelectrode distance of the gate-tuned JJs is $\sim$ 450 nm. The Ti/Al gate fingers of 1.5 μm in width are centered on the fabricated JJs and separated from the SSmS channel by the HfO_2 layer described above. Details on the electrical properties of the JoFETs are reported in the following section.

A representative top-view of one sample can be seen in Fig. 7.3

7.3 JoFET characterization

To identify the actual value of the threshold gate voltage V_g^* of our system and extract the crucial parameters, in Fig. 7.4 (a),

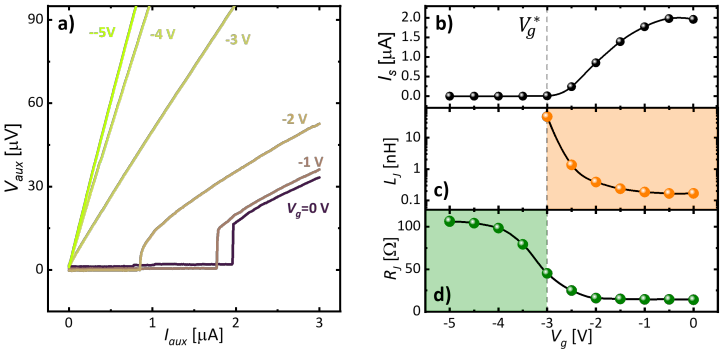


FIGURE 7.4: JoFET characterization. **(a)**: $I - V$ curves taken for an auxiliary JoFET at different gate voltages. **(b)**: The critical current I_s for the auxiliary JoFET as a function of the applied gate voltage. **(c)**: Characterization of the inductance $L_J(V_g)$ curve of the auxiliary JoFET. This curve was calculated from the critical current data via the formula $L_J(V_g) = \phi_0/2\pi I_s(V_g)$ at $T_{bath} = 30$ mK. **(d)**: Normal state resistance R_J as a function of the V_g at $T_{bath} = 30$ mK. The normal-state resistance was extracted from a linear fit in the region where the JoFET exhibits Ohmic behavior in the I-V curves, as shown in panel (a). The curves in panels (b), (c), and (d) were used both to determine V_g^* and to extract the parameters for theoretical simulations.

we show the measured I-V curves of the two JoFETs by injecting a current bias and measuring the voltage drop across the JoFET structure. Those measurements were performed on a nominally identical JoFET structure to the one embedded in the photonic circuit and manufactured on the same chip, because of the impossibility of measuring the full JoFET properties in the circuit coupled with resistors (a detailed discussion of this point can be found in the appendix A).

Figure 7.4 (b) reports the gate dependence of I_s. At a voltage of $V_g \lesssim V_g^* = -3$ V, the switching current reaches a value of zero, thereby eliminating the non-dissipative characteristics of the JoFET. Assuming that the JoFET operates in the linear response regime, its Josephson inductance in the superconducting state can be evaluated

using the relation $L_J(V_g) = \hbar/2eI_s(V_g)$ (e is the elementary charge) and plotted as a function of V_g in Fig. 7.4 (c) on a logarithmic scale. Inductance L_J increases with decreasing V_g, in agreement with the suppression of the switching current, eventually diverging to $+\infty$ for $V_g \to V_g^*$ since $I_s \to 0$.

The normal state resistance of JoFET $R_J(V_g)$ is a crucial parameter for our study and was determined by a linear fit of the Ohmic region of the I-V curves in panel (a) of this figure. The results of $R_J(V_g)$ are shown in Fig. 7.4 (d). In Fig. 7.4 (c,d), the two shaded regions corresponding to the resistive and inductive voltage ranges are shaded, respectively, in green ($V_g \lesssim V_g^*$) and orange ($V_g \geq V_g^*$). The boundary between these regions is at $V_g^* = -3$ V, which is the voltage threshold at which the JoFET switches from superconducting to fully normal.

7.3.1 Operation regimes

To better understand the operation of the device, a numerical calculation of the photonic heat current from the hot to the cold reservoir $\dot{Q}_\gamma^{hot\to cold}(T_{hot}, T_{cold}, V_g)$ was performed in Fig. 7.5, making use of Eqs. (1) and (2), for a fixed temperature of the two reservoirs ($T_{hot} = 350$mK and $T_{cold} = 30$mK) and for three different circuit configurations. Our experimental situation is represented by the orange and green curves in Fig. 7.5, which show the two distinct regimes of $Z(\omega, V_g)$. The orange part of the curve represents the heat current when the inductive nature dominates the impedance for $V_g \geq V^*$ where, instead, the green section shows the resistive-dominated regime when $V_g \lesssim V^*$. Photonic heat transport $\dot{Q}_\gamma^{hot\to cold}(T_{hot}, T_{cold}, V_g)$ decreases monotonically with decreasing gate voltage, with a steep reduction for $V_g < -2.5$ V. This explains the two regimes shown in Fig. 7.1 (c,d), the *transmissive* one where the heat transfer is maximum (orange plateau for $0\text{V} < V_g < 2\text{V}$) and the *reflective* one where the heat transfer is minimum (green plateau for $4.5\text{ V} < V_g < 5$ V). However, the superior response of the JoFET due to its superposition of inductive and resistive responses

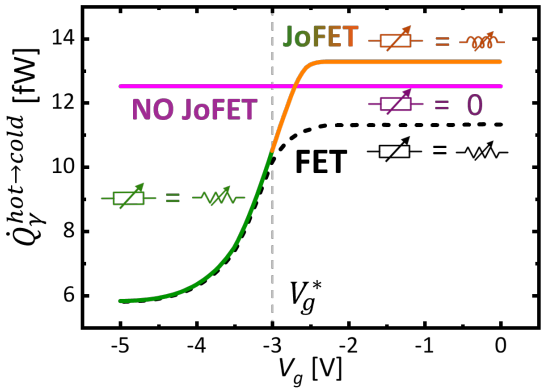


FIGURE 7.5: Numerical calculation of the photonic heat current from the hot to the cold reservoir $\dot{Q}_\gamma^{hot\to cold}(T_{hot}, T_{cold}, V_g)$ as a function of V_g for three different hypothetical configurations. The black curve is calculated as if the coupling circuit were embedded with a conventional field-effect transistor (FET) with resistance parameters equal to those of our JoFET; the black labels for the impedance indicate the configuration's exclusively resistive nature. The orange and green curves are computed for our JoFET in the coupling circuit, showing the two regimes: the inductive one in orange (both the curve and the impedance labels) and the resistive one in green (both the curve and the impedance labels). The purple curve was calculated in the absence of any variable inductors in the coupling circuit; hence, it is independent of V_g.

is clarified by the comparison with the dashed black curve in Fig. 7.5 where instead we computed the same heat current but assuming only the resistive response. This corresponds to the case where the modulating element of the circuit is a standard field-effect transistor (FET), whose only dissipative component is assumed to be equal to the one measured in Fig. 7.4 (d). The comparison between the two situations shows that, for $V_g \lesssim V^*$, the two configurations produce a similar curve; however, the inductive component of the JoFET shows greater heat transfer, resulting in a better contrast between the *transmissive* and *reflective* regimes. In other words, the presence

of an inductive component in a JoFET optimizes impedance matching. For the sake of completeness, in the magenta curve, we also computed the case where no modulating elements are included in the circuit. This curve shows no dependence on the gate voltage, as expected, but reveals an interesting feature of our configuration. The heat transfer in the first plateau is higher in the presence of a JoFET than it would be in the absence of whatever impedance. This behavior is due to a better impedance match throughout the circuit with the inclusion of an inductor. This is mathematically confirmed by examining the denominator of $\tau_{ik}(\omega, V_g)$ in Eq. 7.2 for $V_g \geq V^*$. The presence of an inductive component that contributes in the opposite phase with respect to the capacitative terms reduces the imaginary component of the total impedance $Z_{tot}(\omega)$ at the denominator, increasing the value of τ_{ik} in the gate voltage regime. So we can conclude that the introduction of a JoFET is not only better than the presence of a normal FET but also more convenient, enabling compensation of unavoidable capacitive terms that outperform even the case of complete absence of impedance. This unique gate-tunable impedance matching engineering improves the performance compared to all other configurations.

7.4 Thermometry

The JJs were connected with a standard 4-wire measurement setup (see Fig. 7.2 (c)) where a current is injected $I^{th}_{hot,cold}$ and the voltage drop across the structure $V^{th}_{hot,cold}$ is simultaneously detected to extract the switching current $I_s^{hot,cold}$. Since I_s has a monotonic temperature dependence, we can first measure I_s versus T_{bath} of each junction to calibrate the thermometers and then use the measurement of I_s to infer the electronic temperature of the InAs mesas when the hot reservoir is heated. Radiative thermal transport heats the cold reservoir. The calibration measurements for the thermometer of the cold (hot) reservoir are shown in Fig. 7.6 (a) ((c)). The shaded

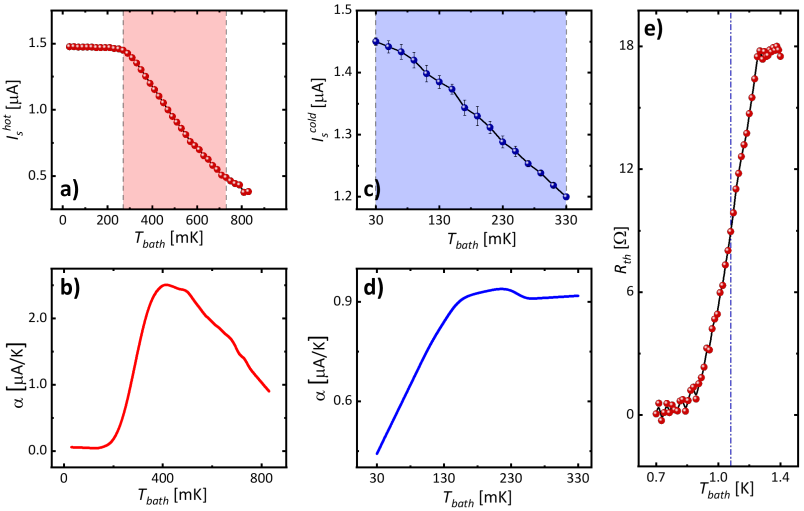


FIGURE 7.6: Calibration of the thermometers and critical temperature. (a), [(c)]: Switching current I_s^{cold} [I_s^{hot}] of the thermometer on the cold [hot] reservoir as a function of T_{bath}. The shaded region shows that this thermometer is operational across the entire range of required temperatures. The experimental data and error bars are the mean and standard deviation of 6 switching current measurements. The solid curve is the result of polynomial interpolation and serves as the calibration curve for inferring the electronic temperature T_{cold} [T_{hot}] from measured switching current. **(b), [(d)]**: Sensitivity $\alpha = \partial I_s^{cold[hot]}/\partial T_{bath}$ as a function of T_{bath}. **(e)**: Resistance of the JJ on the hot reservoir R_{JJ} as a function of T_{bath}. Each point and error bar (not visible since smaller than the point size) in this graph is the result of the mean and standard deviation of 5 resistance measurements.

region in those panels displays the suitable regime of operation of each thermometer, showing that for the cold reservoir detectable temperatures start from 30 mK and go up to 330 mK (there was no need to calibrate the thermometer for higher temperatures), while for the hot reservoir the range of operation of the thermometer is between 260 mK and 730 mK. Those ranges correspond to non-negligible values of the sensitivity $\alpha = \partial I_s/\partial T_{bath}$, as shown in Fig.

7.6 (b,d). The critical temperature T_c of the JJ in the hot reservoir (Fig. 7.2 (c), red shaded panel) was also measured, the results are shown in Fig. 7.6 (e), and we obtained $T_c = 1.12$K. This result is in agreement with the values in the literature of Al-InAs-Al JJs [5, 58], which shows the sound quality of the proximization effect and the interface between Al and InAs.

7.5 Experimental results

In this section, we present experimental results on manipulating heat transfer from the hot to the cold reservoir, as well as the impact of the bath temperature on the phenomenon.

7.5.1 Photonic heat transfer manipulation

The samples were measured inside a dilution refrigerator equipped with filtered electrical lines to minimize external noise. We start by injecting a current into the hot resistor, which raises its temperature, T_{hot}. Measurement T_{cold} enables us to monitor the temperature variation in the cold resistor caused by radiative heat transfer. During this process, we also attempted to manipulate the heat transfer through V_g by using the radiative transport properties of the coupling circuit in Fig. 7.1(b) and Eqs. 7.1, 7.2.

Figure 7.7 (a) shows the results of the radiative heat transport experiment, specifically T_{cold} as a function of V_g for various temperatures of the hot reservoir, T_{hot}, at a bath temperature of $T_{bath} = 30$ mK. From Fig. 7.7 (a), looking at the values of $V_g = 0$, it is visible that the higher T_{hot}, the higher T_{cold} due to the *open* photonic heat channel which can transfer heat from the hot reservoir to the cold one. More importantly, it is shown that for $V_g \leq -2.5$ V all the T_{cold} curves taken for different T_{hot}, start to decrease (except for the one for $T_{hot} = 470$ mK). This behavior is due to the progressive change in photonic transport due to the impedance mismatch created by the gate voltage that causes the JoFETs in Fig. 7.2 (b) to increase their inductance $L_J(V_g)$ first, and then overcome a transition to the

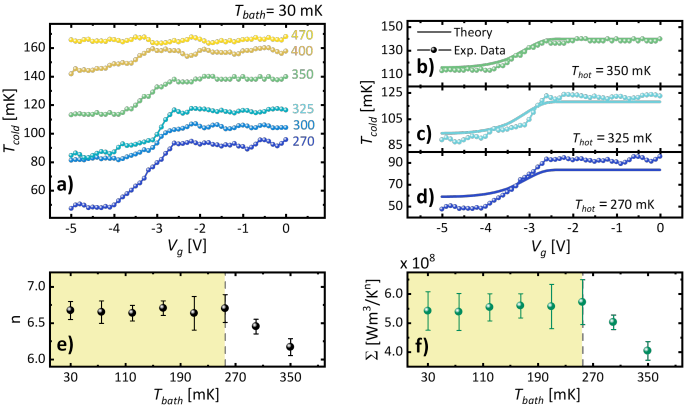


FIGURE 7.7: Photonic heat transport experimental data. (a): T_{cold} as a function of V_g for different T_{hot} in legend at $T_{bath} = 30$ mK. This panel illustrates how the photonic heat transfer channel can be opened for $V_g \geq -3$ V or closed for $V_g \leq -3$ V, demonstrating control over the radiative heat processes. Each point in this figure represents the mean of six critical current measurements of the thermometer on the cold reservoir; the error bars are smaller than the point size. **(b,c,d)**: Comparison of the theoretical model for $T_{cold}(V_g)$ with the experimental data for three different chosen T_{hot} at $T_{bath} = 30$ mK. **(e,f)**: Results of the analysis on the exponent of the power law n and the e-ph coupling constant Σ as a function of T_{bath}. The yellow shaded region represents the range of validity of the analysis (see appendix C and [2]).

normal state with a progressive increase in their resistance $R_J(V_g)$, as shown schematically in Fig. 7.5 (c). This is the *closed* configuration shown in Fig. 7.1 (d), which features the minimum photonic heat transport between the reservoirs. The observation that the curve corresponding to $T_{hot} = 400$ mK exhibits minimal influence from V_g, while the curve for $T_{hot} = 470$ mK remains completely unaffected, can be ascribed to the impact of increasing T_{hot}. This increment extends the dominant frequency range determined by the Bose-Einstein distribution, surpassing the tunable operating cut-off of the JoFET, which is typically on the order of a few tens of GHz,

due to gate residual capacitance shunting [57].
To better understand the behavior of the system up to $T_{hot} = 350$ mK (where the system shows considerable modulation and where the lumped element approximation is still valid), numerical simulations for $T_{cold}(V_g)$ were performed. To perform these simulations, it is essential to note that for $V_g < -3$ V, JoFETs become fully resistive, serving as a third reservoir in our system. However, the fact that $R_J(V_g) \leq 100\ \Omega \ll R_{hot}, R_{cold}$ causes this third reservoir to be severely mismatched with the other two. Hence, we can consider that the photon heat current from the hot and cold reservoirs is much smaller than that from the hot to the cold reservoir $\dot{Q}_\gamma^{hot,cold \to JoFET} \ll \dot{Q}_\gamma^{hot \to cold}$. Considering now that the three reservoirs are made of the same material and have the same volume, and therefore the strength of the e-ph coupling will be the same for all three reservoirs, we can conclude that the temperature variation in the JoFETs is negligible, and we can set it to T_{bath}. These assumptions enable us to set the temperature of R_J to the bath temperature. At equilibrium, all the incoming and outgoing heat currents must sum to 0, and hence the thermal balance on the cold resistor can be calculated as:

$$\begin{aligned} &\dot{Q}_\gamma^{hot \to cold}(T_{hot}, T_{cold}, V_g) - \dot{Q}_\gamma^{cold \to JoFET}(T_{cold}, T_{bath}, V_g) \\ &- \dot{Q}_{e-ph}(T_{cold}, T_{bath}) - \dot{Q}_{ext} = 0, \end{aligned} \tag{7.3}$$

where $\dot{Q}_\gamma^{i \to k}$ and τ_{ik} are calculated using Eqs. 7.1 and 7.2 respectively using resistance and inductance parameters for JoFETs in Fig. 7.5 (c,d), and using for the e-ph coupling $\dot{Q}_{e-ph} = \Sigma V(T_{cold}^n - T_{bath}^n)$, where V is the InAs volume of the cold resistor, $\Sigma = 5.4 \cdot 10^8$ $\mathrm{Wm^3/K^n}$ is the e-ph coupling constant for this specific material and $n = 6.7$ is the exponent of the power law (a further explanation of how Σ and n were extracted will be given below). We arbitrarily added the term $\dot{Q}_{ext}$ to account for unknown power losses in our coupling circuit. We solve Eq. 7.3 for T_{cold} as a function of V_g and compare these results with the experimental data shown in Fig. 7.7 (b,c,d), where the comparison is made for three different values of T_{hot}. What is evident is that the theoretical model reproduces the

shape and dependence of $T_{cold}(V_g)$ very well. In addition, the reason for the high and low plateaus in the T_{cold} vs. V_g curves is now more apparent. The first (high) plateau arises from the fact that the change in L_J with V_g produces a negligible change in $\tau(\omega, V_g)$ up to V_g $simeq -2$ V, and hence in the temperature modulation. The second (low) plateau is instead due to a flat $R_J(V_g)$ characteristic of $V_g < -4.5$ V that causes $\tau(\omega, V_g)$ to be independent of th; without its introduction, we would not have achieved such gth of the term $\dot{Q}_{ext}$ was adjusted to align the simulations with the experimental data, and without its introduction, we would not have achieved such an agreement. In particular, we estimate $\dot{Q}_{ext} = 8$, 5, and 2 fW for the curve at 270, 300, and 350, respectively. This term accounts for power dissipation processes in our coupling circuit, which are currently unknown but certainly present.
To extract Σ and n to perform the calculations in Fig. 7.7 (b,c,d), an extensive characterization of the e-ph coupling on this heterostructure was made in a similar way to what has been shown in chapter 5 (for more information on this characterization, see Appendices C and [2]).

7.5.2 Influence of bath temperature

To assess the robustness of the effect of modulation on photonic transport in relation to bath temperature, measurements analogous to those presented in Fig. 7.7 (a) were carried out, by which $\dot{Q}_{inj} \simeq$ 2.6 pW was kept constant while T_{bath} varied. The injected power corresponded to that utilized for the light green curve in Fig. 7.7 (a) at $T_{hot} = 350$ mK and $T_{bath} = 30$ mK. The results are depicted in Fig. 7.8 (a), demonstrating that up to $T_{bath} = 150$ mK, a modulation in T_{cold} remains discernible; conversely, at higher bath temperatures, the effect disappears due to the augmented e-ph interaction on the InAsOI platform. This finding corroborates our experimental results, theoretically predicted in Fig. 7.8 (b), when we reported the curve $\eta_T = (T_{cold} - T_{bath})/(T_{bath})$ vs. T_{bath}, which denotes the relative difference between T_{cold} and T_{bath} varying bath

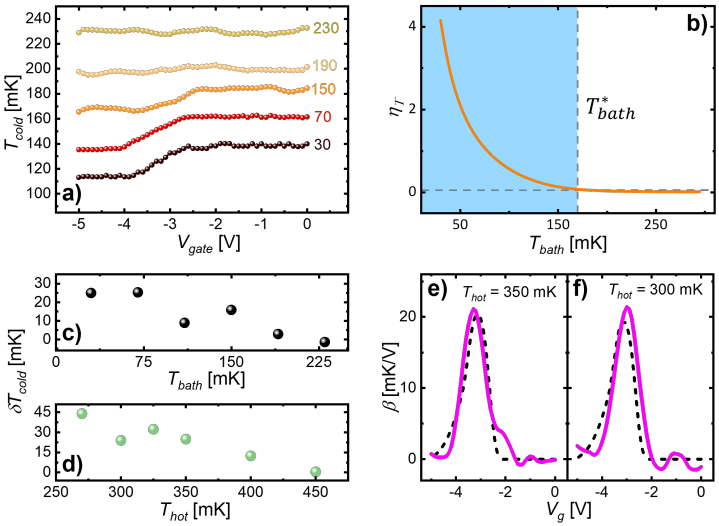


FIGURE 7.8: Influence of the bath temperature on the gate-tunable photonic heat transport modulation (a): Experimental gate-dependent T_{cold} for different T_{bath} (reported in the legend) at $T_{hot} = 350$ mK. Each point represents the mean of six switching current measurements taken on the thermometer at the cold reservoir; error bars are smaller than the point size. **(b)**: Numerical simulation of $\eta_T = (T_{cold} - T_{bath})/(T_{bath})$. The horizontal gray dashed line corresponds to $\eta_T^* = 0.1$, where the relative difference between T_{cold} and T_{bath} is negligible. The vertical gray dashed line indicates $T^*_{bath} = 170$ mK associated with $\eta_T^* = 0.1$. The blue-shaded region represents the bath temperature range in which the cold reservoir operates properly. **(c)-(d)**: Temperature difference δT_{cold} of the cold reservoir between the JoFET operating in the superconducting state ($V_g > -2V$) and the resistive state ($V_g < -4V$). Black points in panel **c** report data versus T_{bath} while green points in panel **d** report data versus T_{hot}. **(e)-(f)**: Gate-dependent thermal transimpedance $\beta = \partial T_{cold}/\partial V_g$ for two different selected T_{hot} at $T_{bath} = 30$ mK. The magenta curve refers to experimental data, while the black dashed curve indicates theoretical results obtained with the model.

temperature (a comprehensive discussion of the methodology of this simulation is provided within appendix B). As the photonic heat

current $\dot{Q}_{\gamma}^{hot \to cold}$, at a constant injected power $\dot{Q}_{inj}$, depends on the temperature differential between the reservoirs, an increase in the bath temperature evidently results in a decrease in the relative variation of T_{cold}. For a plausible representative value of $\dot{Q}_{inj} = 2.6$ pW, the relative difference between T_{cold} and T_{bath} is not negligible ($\eta_T > 0.1$) only if $T_{bath} < T^*_{bath} = 170$ mK. This interval of values of T_{bath}, which is expected to be the optimal regime for observing thermal modulation, is highlighted as a blue-shaded area in Fig. 7.8 (b). For $T_{bath} > T^*_{bath}$, the electron-phonon (e-ph) coupling becomes predominant, thus entirely overshadowing the influence of the photonic heat current $\dot{Q}_{\gamma}^{hot \to cold}$.

To comprehensively assess the performance of our device, we have derived the maximum temperature variation δT_{cold}, calculated as the difference between the upper and lower temperature plateaus of the T_{cold} versus V_g curves of Fig. 7.7 (a) and 7.8 (a). Figures 7.8 (c) and (d) report δT_{cold} as a function of T_{bath} and T_{hot}, respectively. Analyzing δT_{cold} against T_{hot}, the presence of JoFET allows the modulation of the cold-resistor temperature of ~ 45 mK for $T_{hot} = 270$ mK, setting the record value of the state of the art ($\gtrsim 20$ times) for the modulation of temperature achieved through electrostatic control [88]. This breakthrough temperature modulation is attributed to the implementation of JoFET on the InAsOI platform, which has been recognized as an optimal candidate for gate-tunable heat transport architectures due to its reduced electron-phonon coupling, compared to traditionally used metals [2, 5] and, at the same time, for the better impedance matching determined by the JoFET inductive component.

The δT_{cold} vs. T_{hot} shows a monotonic decrease with increasing T_{hot}, becoming negligible at $T_{hot} \sim 470$ mK, where the effect vanishes. An analogous decrease is observed for δT_{cold} vs. T_{bath}, reaching negligible levels for $T_{bath} \gtrsim 170$ mK. These trends are due to two different phenomena, as explained above, and confirm what was already mentioned. In the first case, an increase in T_{hot} produces a higher-frequency spectrum of thermal radiation, which is more strongly affected by capacitive shunting of the modulating impedance

of the JoFET due to gate capacitances. In the latter, the increase of T_{bath} reduces the relative significance of the contribution of the photonic heat current to the definition of T_{cold} (see Fig. 7.8 (b)).

Figures 7.8 (e) and (f) illustrate the impact of V_g on T_{cold}, calculating the thermal transfer function $\beta = \partial T_{cold}/\partial V_g$ as a function of V_g for $T_{hot} = 350$ mK and $T_{hot} = 300$ mK, respectively, at $T_{bath} = 30$ mK. In particular, for both curves, V_g exerts minimal influence from -5 V to -4.5 V, then significantly affects T_{cold}, achieving values of 20 mK/V for $V_g \sim V^*$, followed by negligible effects between -2 V and 0 V, in alignment with the properties of the JoFET. The black-dashed lines depict the results of the theoretical model. The comparative analysis demonstrates that the model accurately predicts gate dependence, as previously described. This observation highlights the model's ability to precisely characterize the dynamic behavior of T_{cold} as a function of gate voltage, thereby resolving uncertainties associated with unavoidable gate-independent terms.

7.6 Final considerations

In summary, we have presented a hybrid semiconductor-superconductor device that demonstrates giant thermal modulation of up to $\delta T_{cold} \simeq 45$ mK in a fully wireless, non-galvanic environment at a remarkable distance of ~ 1 mm. This was achieved by utilizing the gating properties of two JoFETs embedded in a lumped-element circuit, which enabled us to modify the photonic heat transfer from a hot reservoir to a cold reservoir as a result of blackbody radiation. Our work sets a new record in the electrostatic control of radiative heat transfer, outperforming the values in the literature by more than one order of magnitude [88]. We also demonstrated the suitability of the InAsOI platform for heat management experiments because of its low electron-phonon coupling, scalable gating options, and ease of integration of highly sensitive SSmS thermometers. Our device operates at bath temperatures up to ~ 170 mK and represents a step forward toward the implementation of heat management and

routing structures [81, 91, 104]. Those effects are of great interest in the fields of radiation sensing [68, 107, 108] and energy management of quantum architectures [90, 97, 109, 110], as long as the realization of thermal logic gates and memories [102, 103, 111].

Chapter 8

Conclusions and future perspectives

This thesis was motivated by the challenge of developing efficient and scalable architectures for coherent caloritronics. Although micro- and nanoscale superconductors offer a unique playground for low-temperature thermal manipulation, the field has historically relied on magnetic fields for control. This approach suffers from significant drawbacks in scalability, integration, and overall complexity. The primary objective of this work was therefore to investigate and demonstrate a new paradigm for thermal management based on electrostatic control, paving the way for a more practical and scalable "caloritronic architecture" that leverages electric fields, much as modern CMOS technology does.

To this end, this work has delivered two main results, supported by a crucial investigation into a novel material platform.

First, we present a comprehensive theoretical framework for a bipolar thermoelectric superconducting single-electron transistor (SET). This study, detailed in Chapter 4, established the theoretical feasibility of manipulating superconducting thermoelectric effects purely via a gate voltage. By analyzing the system in the sequential tunneling regime and under Coulomb blockade, we demonstrated how an applied gate potential could tune the device's thermoelectric

properties, representing a significant step toward the electrical control of heat currents in solid-state devices.

Second, and most significantly, this thesis presented the *first experimental demonstration of a gate-tunable photonic field-effect heat transistor*. This device, the central focus of Chapter 7, utilizes a hybrid semiconductor-superconductor platform to electrostatically control radiative heat transfer between two reservoirs separated by a macroscopic distance of ~ 1 mm. The key innovation was the integration of gate-tunable Josephson Field-Effect Transistors (JoFETs) into a lumped-element circuit, enabling modulation of the coupling channel impedance by an electric field. This electrostatic control resulted in a *giant thermal modulation* of the cold reservoir's temperature ($\delta T_{\mathrm{cold}} \simeq 45$ mK), a performance that surpasses the current state-of-the-art by more than an order of magnitude.

The success of this experiment was underpinned by the work presented in Chapter 5: the characterization of the *InAs-on-Insulator (InAsOI) platform*. We demonstrated that this novel material exhibits extremely weak sub-Kelvin electron-phonon (e-ph) coupling. This property is paramount for caloritronic applications, as it thermally decouples the electronic system from the lattice phonons, minimizing energy losses to the substrate and maximizing the electronic temperature changes that are crucial for device operation. The suitability of InAsOI was further confirmed in Chapter 6 through the successful fabrication and characterization of the essential building blocks for the photonic transistor: high-quality gate dielectrics and high-performance JoFETs.

In summary, this thesis has successfully established that top-gated hybrid semiconductor-superconductor systems, and the InAsOI platform in particular, are a viable, scalable, and high-performance solution for coherent heat management. We not only proposed a new electrically driven thermoelectric device, but also demonstrated a record-breaking non-galvanic photonic heat transistor, advancing the field of coherent caloritronics a significant step closer to practical and complex applications.

Future Perspectives

The results obtained in this thesis open several promising avenues for future research, building directly upon the foundations laid herein.

1. *Experimental Realization of the Thermoelectric SET*
   The theoretical proposal of the gate-tunable bipolar superconducting thermoelectric SET in Chapter 4 is a compelling candidate for experimental verification. A clear and immediate future perspective is the fabrication and characterization of this device. This would lead to the realization of an active element which can convert thermal energy to electrical energy, controllable via an external electrical field.

2. *Integrated Caloritronic Circuits*
   Demonstrating a functional heat transistor is the first step toward more complex thermal circuits. The non-galvanic, "wireless" nature of the photonic device is particularly well-suited for integration. Future work should focus on scaling this concept to create integrated architectures, such as heat routers, splitters, and interferometers, in which multiple reservoirs are coupled and local gates actively and independently control their thermal links. This could lead to the realization of the previously envisioned thermal logic gates and memories.

3. *On-Chip Thermal Management for Quantum Systems*
   The ability to actively manage heat at the nanoscale is of profound interest for quantum computing and sensing architectures. A future direction would be to integrate our photonic heat transistor directly with quantum circuits (e.g., superconducting qubits or bolometers) to perform active, on-demand thermal management. This could involve using the device as a "thermal switch" to isolate a quantum processor from a noisy environment or to reset quantum devices to their ground state rapidly.

4. *Performance Optimization and Higher-Temperature Operation*
   Although our device sets a new record, its performance can be further optimized. Future studies could explore different circuit parameters to improve impedance matching and increase modulation depth. Furthermore, investigating materials with similar weak e-ph coupling but larger superconducting gaps could raise the operating temperature of these devices above the ~170 mK limit observed in this work, making them compatible with a broader range of cryogenic systems.

5. *Further Exploration of the InAsOI Platform*
   The "attractive thermal properties" of InAsOI make it a promising platform beyond the specific devices studied here. Its semiconducting nature, combined with superconductivity and low thermal losses, invites the exploration of new hybrid phenomena in which charge, heat, and superconducting coherence are intertwined and controlled by an electric field.

In conclusion, the work of this thesis has helped establish a new, robust, and scalable pathway for controlling heat at the nanoscale. The future of the field lies in harnessing this electrical control to build the complex, integrated caloritronic circuits that will be essential for the next generation of quantum technologies and advanced sensors.

Appendix A

Auxiliary JoFET characterization

In this appendix we are going to give the details on how we could measure the parameters of the JoFET without influencing the coupling circuit of the studied device.

The electrical performance of the JoFET architecture was evaluated on a twin architecture fabricated on the same chip (Fig. A.1 (a)), which was useful to avoid the impacts of parasitic elements due to the fabrication of the bonding pads and the relative measurement setup.

Fig. A.1 (b) shows the dependence of I_s on T_{bath}, where a monotonic decrease trend is observed as expected. Figure A.1 (c) reports the dependence of I_s as a function of the out-of-the-plane magnetic field B, where the B-tuned typical SQUID-like behavior is apparent. In particular, the interference pattern minima show I_s of about ~ 500 nA, instead of reaching a null switching current. This results in reduced variation of the B-tuned Josephson inductance L_J, causing a negligible impact on the modulation of the photonic heat current $\dot{Q}_{\gamma}^{hot \to cold}$. The results achieved ruled out the use of SQUID-like interference as an effective method for tuning photonic heat transport in our experimental configuration.

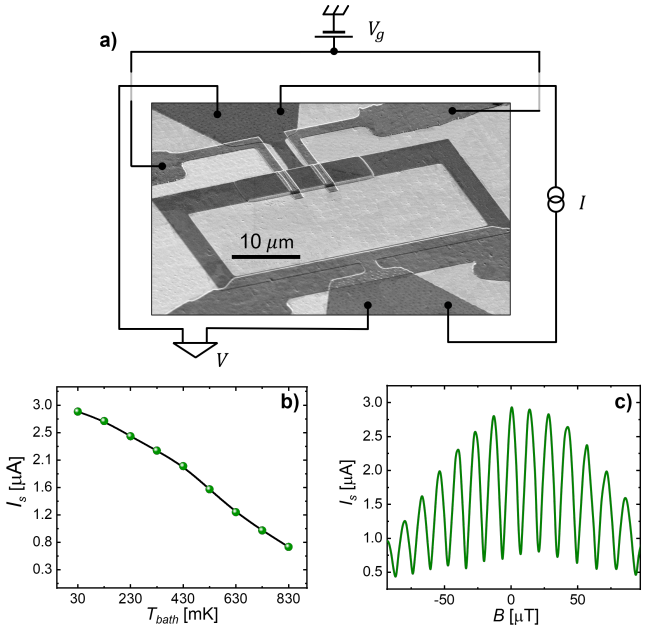


Figure A.1: JoFET twin architecture present on the same chip. (a): SEM image of the twin JoFET architecture with the wiring setup used for the measurements. The two JoFETs are also embedded in a SQUID loop, as in the coupling circuit of the studied device. The flux line that passes over the loop is also visible, but it was not used in the experiment. **(b)**: Switching current I_s of the twin JoFET architecture as a function of the bath temperature T_{bath}. **(c)**: Switching current of the twin JoFET architecture as a function of the out-of-plane magnetic field B.

Appendix B

T^*_{bath} calculation

In This appendix we are giving more details on the calculation performed to find out the limit bath temperature until which our photonic device works properly.

The temperature of the cold terminal is mainly determined by two competing heat fluxes: $\dot{Q}_\gamma^{hot\to cold}$ and $\dot{Q}_{e-ph}$, as shown in Eq. 7.3. In order to give an estimate of the conditions where one dominates the other, we neglect $\dot{Q}_\gamma^{cold\to JoFET}$, which is smaller than the other currents involved, as already explained in chapter 7.
To estimate the value of the crossover temperature $T^*_{bath} \approx 170$mK, cited in the main text, at which the V_g-sensitive behavior is expected to fade out, the following calculation was performed. We inject a power of $\dot{Q}_{inj} = 2.6$pW into the hot reservoir (as did experimentally) and compute the thermal balance in this reservoir to calculate T_{hot}:

$$\dot{Q}_{inj} - \dot{Q}_{e-ph}(T_{hot}, T_{bath}) = 0. \tag{B.1}$$

In the above equation, we neglected the term $\dot{Q}_\gamma^{hot\to cold}(T_{cold}, T_{bath}, V_g)$, as it is roughly three orders of magnitude smaller than the other two. Then we compute T_{cold} with the simplified thermal balance on the cold reservoir:

$$\dot{Q}_\gamma^{hot\to cold}(T_{cold}, T_{bath}, V_g) - \dot{Q}_{e-ph}(T_{cold}, T_{bath}) = 0, \tag{B.2}$$

and calculate the relative difference between T_{cold} and T_{bath} as $\eta_T = (T_{cold} - T_{bath})/(T_{bath})$ to evaluate the impact of the photonic transport with respect to the e-ph coupling in the cold reservoir. The results of this relative difference as a function of T_{bath} are shown in Fig. 7.8 (b). This figure shows the expected behavior, with the T_{cold} becoming closer and closer to T_{bath} as the T_{bath} increases. In particular, to define a crossover temperature, we take the point where $\eta_T = 0.1$ (marked by the horizontal grey dashed line), that is to say the reported value of $T_{bath} = 170$mK. Consequently, the area highlighted in blue in the figure is the experimentally relevant range of T_{bath}, where the dependence of T_{cold} on $\dot{Q}_{\gamma}^{hot \to cold}$ (and consequently on V_{gate}) is sizable.

Appendix C

Electron-phonon coupling measurements

In this appendix we are going to give the details on how we measured the relevant e-ph coupling parameters for our structure in order to perform all the simulations needed.

Due to the necessity to know the e-ph parameters to both perform simulations and properly design the sample, an extensive characterization about the e-ph coupling on the heterostructure was made. The setup to perform this measurements is the one shown in chapter 5, where a power P_{inj} is injected in an InAs mesa of volume V through Joule heaters and supposing that the electrons can only exchange heat with the lattice phonons, the thermal balance can be written as $P_{inj} - \Sigma V(T_e^n - T_{bath}^n) = 0$, where the electronic temperature T_e can be extracted as a function of P_{inj} at a fixed T_{bath} with Σ and n as parameters:

$$T_e = \sqrt[n]{\frac{P_{inj}}{\Sigma V} + T_{bath}^n}. \tag{C.1}$$

The electronic temperature T_e can be measured as a function of P_{inj} via a thermometer on the InAs mesa and fitting the $T_e(P_{inj})$ curves with the Eq. S3 one can find the fitting parameters σ and n. The fittings are shown in Fig. C.1 (a,b,c,d) where four selected T_e vs P_{inj} curves for four different T_{bath} are displayed to see the optimal

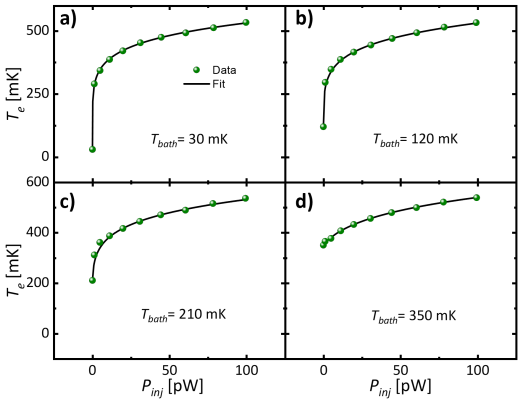


FIGURE C.1: **(a,b,c,d)**: These panels show preliminary measurements of e-ph coupling on this heterostructure. In particular the electronic temperature T_e was measured as a function of the injected power P_{inj} for different T_{bath} to extract the exponent n and the coupling constant Σ of the e-ph coupling formula. Experimental data with best fits are shown for four selected T_{bath} to show the optimal accordance.

accordance with the experimental data. The results for n and Σ are shown in Fig. 7.7 (e,f) of the main text where the points and errorbars are the outcome of a best fit procedure with Eq. C.1 and the yellow shaded region indicates the range of validity of the fittings which is $T_{bath} < 260$mK. This is due to a non perfect thermalization of the InAs mesa for higher temperatures of the bath [2].

Bibliography

1. Battisti, S., De Simoni, G., Chirolli, L., Braggio, A. & Giazotto, F. Bipolar Thermoelectric Superconducting Single-Electron Transistor. *Phys. Rev. Research* **6,** L012022 (2024).
2. Battisti, S. *et al.* Extremely Weak Sub-Kelvin Electron–Phonon Coupling in InAs on Insulator. *Applied Physics Letters* **125,** 202601 (2024).
3. Battisti, S. *et al.* Giant thermal modulation via a semiconductor-superconductor photonic field-effect heat transistor. *arXiv preprint arXiv:2510.17683* (2025).
4. Paghi, A., Battisti, S., Tortorella, S., De Simoni, G. & Giazotto, F. Cryogenic Behavior of High-Permittivity Gate Dielectrics: The Impact of Atomic Layer Deposition Temperature and the Lithographic Patterning Method. *Journal of Applied Physics* **137,** 044103 (2025).
5. Paghi, A. *et al.* Josephson Field Effect Transistors with InAs on Insulator and High Permittivity Gate Dielectrics. *ACS Appl. Electron. Mater.* **7,** 3756–3764 (2025).
6. Battisti, S. *et al.* Demonstration of High-Impedance Superconducting NbRe Dayem Bridges. *Appl. Phys. Lett.* **124,** 172601 (2024).
7. Koch, J. *et al.* Gate-Controlled Supercurrent Effect in Dry-Etched Dayem Bridges of Non-Centrosymmetric Niobium Rhenium. *Nano Res.* **17,** 6575–6581 (2024).

8. Antola, F., Battisti, S., Braggio, A., Giazotto, F. & Simoni, G. D. *Streamline Controlled Rectification of Supercurrent in Thin-Film Asymmetric Weak Links* 2025.
9. Bardeen, J., Cooper, L. N. & Schrieffer, J. R. Theory of Superconductivity. *Phys. Rev.* **108,** 1175–1204 (1957).
10. Tinkham, M. *Introduction to Superconductivity* (Courier Corporation, 2004).
11. Dynes, R. C., Garno, J. P., Hertel, G. B. & Orlando, T. P. Tunneling Study of Superconductivity near the Metal-Insulator Transition. *Phys. Rev. Lett.* **53,** 2437–2440 (1984).
12. Golubov, A. A., Kupriyanov, M. Y. & Il'ichev, E. The Current-Phase Relation in Josephson Junctions. *Rev. Mod. Phys.* **76,** 411–469 (2004).
13. Josephson, B. D. Possible New Effects in Superconductive Tunnelling. *Physics Letters* **1,** 251–253 (1962).
14. Averin, D. & Likharev, K. in *Modern Problems in Condensed Matter Sciences* 173–271 (Elsevier, 1991).
15. Andreev, A. F. THERMAL CONDUCTIVITY OF THE INTERMEDIATE STATE OF SUPERCONDUCTORS. II.
16. Beenakker, C. W. J. Universal Limit of Critical-Current Fluctuations in Mesoscopic Josephson Junctions. *Phys. Rev. Lett.* **67,** 3836–3839 (1991).
17. Kulik, I. O. & Omel'Yanchuk, A. N. Contribution to the Microscopic Theory of the Josephson Effect in Superconducting Bridges. *Soviet Journal of Experimental and Theoretical Physics Letters* **21,** 96 (1975).
18. Dubos, P. *et al.* Josephson Critical Current in a Long Mesoscopic S-N-S Junction. *Phys. Rev. B* **63,** 064502 (2001).
19. Mott, N. F., Jones, H., Jones, H. & Jones, H. *The Theory of the Properties of Metals and Alloys* (Courier Dover Publications, 1958).

20. Marchegiani, G., Braggio, A. & Giazotto, F. Nonlinear Thermoelectricity with Electron-Hole Symmetric Systems. *Phys. Rev. Lett.* **124,** 106801 (2020).

21. Marchegiani, G., Braggio, A. & Giazotto, F. Superconducting Nonlinear Thermoelectric Heat Engine. *Phys. Rev. B* **101,** 214509 (2020).

22. Germanese, G., Paolucci, F., Marchegiani, G., Braggio, A. & Giazotto, F. Bipolar Thermoelectric Josephson Engine. *Nat. Nanotechnol.* **17,** 1084–1090 (2022).

23. Germanese, G., Paolucci, F., Marchegiani, G., Braggio, A. & Giazotto, F. Phase Control of Bipolar Thermoelectricity in Josephson Tunnel Junctions. *Phys. Rev. Applied* **19,** 014074 (2023).

24. Pekola, J. P. *et al.* Hybrid Single-Electron Transistor as a Source of Quantized Electric Current. *Nature Phys* **4,** 120–124 (2008).

25. Wellstood, F. C., Urbina, C. & Clarke, J. Hot-Electron Effects in Metals. *Phys. Rev. B* **49,** 5942–5955 (1994).

26. Pothier, H. Energy Distribution Function of Quasiparticles in Mesoscopic Wires. *Phys. Rev. Lett.* **79,** 3490–3493 (1997).

27. Rammer, J. *Quantum Transport Theory Frontiers in Physics* **99** (Westview, Boulder, Colo., 2004).

28. *Electron-Electron Interactions in Disordered Systems* (eds Ėfros, A. L. & Pollak, M.) *Modern Problems in Condensed Matter Sciences* **vol. 10** (North-Holland ; Sole distributors for the U.S.A. and Canada, Elsevier Science Pub. Co, Amsterdam ; New York : New York, N.Y., U.S.A, 1985).

29. Voutilainen, J. Nonequilibrium Phenomena in Multiple Normal-Superconducting Tunnel Heterostructures. *Phys. Rev. B* **72** (2005).

30. Taskinen, L. J., Kivioja, J. M., Karvonen, J. T. & Maasilta, I. J. Direct Measurement of the Electron-Phonon Relaxation Rate in Thin Copper Films. *physica status solidi (c)* **1,** 2856–2859 (2004).

31. Sergeev, A. & Mitin, V. Electron-Phonon Interaction in Disordered Conductors: Static and Vibrating Scattering Potentials. *Phys. Rev. B* **61,** 6041–6047 (2000).

32. Giazotto, F., Heikkilä, T. T., Luukanen, A., Savin, A. M. & Pekola, J. P. Opportunities for Mesoscopics in Thermometry and Refrigeration: Physics and Applications. *Rev. Mod. Phys.* **78,** 217–274 (2006).

33. Timofeev, A. V. *et al.* Recombination-Limited Energy Relaxation in a Bardeen-Cooper-Schrieffer Superconductor. *Phys. Rev. Lett.* **102,** 017003 (2009).

34. Johnson, J. B. Thermal Agitation of Electricity in Conductors. *Phys. Rev.* **32,** 97–109 (1928).

35. Nyquist, H. Thermal Agitation of Electric Charge in Conductors. *Phys. Rev.* **32,** 110–113 (1928).

36. Pascal, L. M. A., Courtois, H. & Hekking, F. W. J. Circuit Approach to Photonic Heat Transport. *Phys. Rev. B* **83,** 125113 (2011).

37. Arif, O. *et al.* Influence of an Overshoot Layer on the Morphological, Structural, Strain, and Transport Properties of InAs Quantum Wells. *Nanomaterials* **14,** 592 (2024).

38. Benali, A. *et al.* Metamorphic InAs/InGaAs QWs with Electron Mobilities Exceeding 7 × 105 Cm2/Vs. *Journal of Crystal Growth* **593,** 126768 (2022).

39. Bernazzani, L., Marchegiani, G., Giazotto, F., Roddaro, S. & Braggio, A. Bipolar Thermoelectricity in Bilayer-Graphene–Superconductor Tunnel Junctions. *Phys. Rev. Applied* **19,** 044017 (2023).

40. Paolucci, F., Germanese, G., Braggio, A. & Giazotto, F. A Highly Sensitive Broadband Superconducting Thermoelectric Single-Photon Detector. *Applied Physics Letters* **122,** 173503 (2023).

41. Marchegiani, G., Braggio, A. & Giazotto, F. Phase-Tunable Thermoelectricity in a Josephson Junction. *Phys. Rev. Research* **2,** 043091 (2020).

42. Nazarov, Y. V. & Blanter, Y. M. *Quantum Transport: Introduction to Nanoscience* (Cambridge University Press, 2009).

43. Marchegiani, G., Braggio, A. & Giazotto, F. Noise Effects in the Nonlinear Thermoelectricity of a Josephson Junction. *Applied Physics Letters* **117,** 212601 (2020).

44. Bagrets, D. A. & Nazarov, Y. V. Full Counting Statistics of Charge Transfer in Coulomb Blockade Systems. *Phys. Rev. B* **67,** 085316 (2003).

45. Braggio, A., König, J. & Fazio, R. Full Counting Statistics in Strongly Interacting Systems: Non-Markovian Effects. *Phys. Rev. Lett.* **96,** 026805 (2006).

46. Flindt, C., Novotný, T., Braggio, A., Sassetti, M. & Jauho, A.-P. Counting Statistics of Non-Markovian Quantum Stochastic Processes. *Phys. Rev. Lett.* **100,** 150601 (2008).

47. Beenakker, C. W. J. Theory of Coulomb-blockade Oscillations in the Conductance of a Quantum Dot. *Phys. Rev. B* **44,** 1646–1656 (1991).

48. Maisi, V. F. *et al.* Excitation of Single Quasiparticles in a Small Superconducting Al Island Connected to Normal-Metal Leads by Tunnel Junctions. *Phys. Rev. Lett.* **111,** 147001 (2013).

49. Staring, A. A. M. *et al.* Coulomb-Blockade Oscillations in the Thermopower of a Quantum Dot. *EPL* **22,** 57 (1993).

50. Mahan, G. D. & Sofo, J. O. The Best Thermoelectric. *Proc. Natl. Acad. Sci. U.S.A.* **93,** 7436–7439 (1996).

51. Sothmann, B., Sánchez, R. & Jordan, A. N. Thermoelectric Energy Harvesting with Quantum Dots. *Nanotechnology* **26,** 032001 (2014).

52. Goldsmid, H. *Thermoelectric Refrigeration* (Springer, 2013).

53. Benenti, G., Casati, G., Saito, K. & Whitney, R. S. Fundamental Aspects of Steady-State Conversion of Heat to Work at the Nanoscale. *Physics Reports. Fundamental Aspects of Steady-State Conversion of Heat to Work at the Nanoscale* **694,** 1–124 (2017).

54. Bauer, G. & Kahlert, H. Low-Temperature Non-Ohmic Galvanomagnetic Effects in Degenerate n -Type InAs. *Phys. Rev. B* **5,** 566–579 (1972).

55. Price, P. J. Hot Electrons in a GaAs Heterolayer at Low Temperature. *Journal of Applied Physics* **53,** 6863–6866 (1982).

56. Muhonen, J. T. *et al.* Strain Dependence of Electron-Phonon Energy Loss Rate in Many-Valley Semiconductors. *Applied Physics Letters* **98,** 182103 (2011).

57. Paghi, A. *et al.* Supercurrent Time Division Multiplexing with Solid-State Integrated Hybrid Superconducting Electronics. *Nat Commun* **16,** 8442 (2025).

58. Paghi, A. *et al.* InAs on Insulator: A New Platform for Cryogenic Hybrid Superconducting Electronics (Adv. Funct. Mater. 7/2025). *Advanced Functional Materials* **35,** 2570040 (2025).

59. Giazotto, F. *et al.* Reflectionless Tunneling in Planar Nb/-GaAs Hybrid Junctions. *Applied Physics Letters* **78,** 1772–1774 (2001).

60. Giazotto, F. *et al.* Resonant Transport in Nb $/$GaAs $/$AlGaAs Heterostructures: Realization of the de Gennes–Saint-James Model. *Phys. Rev. Lett.* **87,** 216808 (2001).

61. Cochran, J. F. & Mapother, D. E. Superconducting Transition in Aluminum. *Phys. Rev.* **111,** 132–142 (1958).

62. Bhargava, S., Blank, H.-R., Narayanamurti, V. & Kroemer, H. Fermi-Level Pinning Position at the Au–InAs Interface Determined Using Ballistic Electron Emission Microscopy. *Applied Physics Letters* **70,** 759–761 (1997).

63. Melitz, W. *et al.* Scanning Tunneling Spectroscopy and Kelvin Probe Force Microscopy Investigation of Fermi Energy Level Pinning Mechanism on InAs and InGaAs Clean Surfaces. *Journal of Applied Physics* **108,** 023711 (2010).

64. Edwards, J. T. & Thouless, D. J. Numerical Studies of Localization in Disordered Systems. *J. Phys. C: Solid State Phys.* **5,** 807 (1972).

65. *Physics and Applications of the Josephson Effect* https://www.iris.unina.it/handle/11588/177176.

66. Suominen, H. J. *et al.* Anomalous Fraunhofer Interference in Epitaxial Superconductor-Semiconductor Josephson Junctions. *Phys. Rev. B* **95,** 035307 (2017).

67. Gasparinetti, S. *et al.* Fast Electron Thermometry for Ultrasensitive Calorimetric Detection. *Phys. Rev. Appl.* **3,** 014007 (2015).

68. Virtanen, P., Ronzani, A. & Giazotto, F. Josephson Photodetectors via Temperature-to-Phase Conversion. *Phys. Rev. Appl.* **9,** 054027 (2018).

69. Kokkoniemi, R. *et al.* Bolometer Operating at the Threshold for Circuit Quantum Electrodynamics. *Nature* **586,** 47–51 (2020).

70. Kokkoniemi, R. *et al.* Nanobolometer with Ultralow Noise Equivalent Power. *Commun Phys* **2,** 1–8 (2019).

71. Solinas, P., Giazotto, F. & Pepe, G. P. Proximity SQUID Single-Photon Detector via Temperature-to-Voltage Conversion. *Phys. Rev. Appl.* **10,** 024015 (2018).

72. Subero, D. *et al.* Bolometric Detection of Josephson Inductance in a Highly Resistive Environment. *Nat Commun* **14,** 7924 (2023).

73. Gunnarsson, D. *et al.* Interfacial Engineering of Semiconductor–Superconductor Junctions for High Performance Micro-Coolers. *Sci Rep* **5,** 17398 (2015).

74. Meschke, M., Pekola, J. P., Gay, F., Rapp, R. E. & Godfrin, H. Electron Thermalization in Metallic Islands Probed by Coulomb Blockade Thermometry. *Journal of Low Temperature Physics* **134,** 1119–1143 (2004).

75. José Martínez-Pérez, M. & Giazotto, F. A Quantum Diffractor for Thermal Flux. *Nat Commun* **5,** 3579 (2014).

76. Martínez-Pérez, M. J., Fornieri, A. & Giazotto, F. Rectification of Electronic Heat Current by a Hybrid Thermal Diode. *Nature Nanotech* **10,** 303–307 (2015).

77. Taskinen, L. J. & Maasilta, I. J. Improving the Performance of Hot-Electron Bolometers and Solid State Coolers with Disordered Alloys. *Applied Physics Letters* **89,** 143511 (2006).

78. Savin, A. *et al.* Electron-Phonon Coupling in Heavily Doped Silicon: Physics Days - Fysiikan Päivät 2001. *The XXXV annual conference of the Finnish physical society* (2001).

79. Roddaro, S. *et al.* Hot-Electron Effects in InAs Nanowire Josephson Junctions. *Nano Res.* **4,** 259–265 (2011).

80. Degheidy, A. R., Abuali, A. M. & Elkenany, E. B. The Response of Phonon Frequencies, Sound Velocity, Electronic, Optical, and Mechanical Properties of Indium (Phosphide, Arsenide, and Antimonide) to Hydrostatic Pressure. *ECS J. Solid State Sci. Technol.* **11,** 063016 (2022).

81. Giazotto, F. & Martínez-Pérez, M. J. The Josephson Heat Interferometer. *Nature* **492,** 401–405 (2012).

82. Meschke, M., Guichard, W. & Pekola, J. P. Single-Mode Heat Conduction by Photons. *Nature* **444,** 187–190 (2006).

83. Buonomo, B. *et al.* Electron Thermometry and Refrigeration with Doped Silicon and Superconducting Electrodes. *Journal of Applied Physics* **94,** 7784–7788 (2003).

84. Fornieri, A. & Giazotto, F. Towards Phase-Coherent Caloritronics in Superconducting Circuits. *Nature Nanotech* **12,** 944–952 (2017).

85. Fornieri, A., Martínez-Pérez, M. J. & Giazotto, F. Electronic Heat Current Rectification in Hybrid Superconducting Devices. *AIP Advances* **5,** 053301 (2015).

86. Hwang, S.-Y. & Sothmann, B. Phase-Coherent Caloritronics with Ordinary and Topological Josephson Junctions. *Eur. Phys. J. Spec. Top.* **229,** 683–705 (2020).

87. Giazotto, F. *et al.* Ultrasensitive Proximity Josephson Sensor with Kinetic Inductance Readout. *Applied Physics Letters* **92,** 162507 (2008).

88. Maillet, O., Subero, D., Peltonen, J. T., Golubev, D. S. & Pekola, J. P. Electric Field Control of Radiative Heat Transfer in a Superconducting Circuit. *Nat Commun* **11,** 4326 (2020).

89. Ronzani, A. *et al.* Tunable Photonic Heat Transport in a Quantum Heat Valve. *Nature Phys* **14,** 991–995 (2018).

90. Gubaydullin, A. *et al.* Photonic Heat Transport in Three Terminal Superconducting Circuit. *Nat Commun* **13,** 1552 (2022).

91. Partanen, M. *et al.* Quantum-Limited Heat Conduction over Macroscopic Distances. *Nature Phys* **12,** 460–464 (2016).

92. Ojanen, T. & Jauho, A.-P. Mesoscopic Photon Heat Transistor. *Phys. Rev. Lett.* **100,** 155902 (2008).

93. Marchegiani, G., Braggio, A. & Giazotto, F. Highly Efficient Phase-Tunable Photonic Thermal Diode. *Applied Physics Letters* **118,** 022602 (2021).

94. Paolucci, F., Marchegiani, G., Strambini, E. & Giazotto, F. Phase-Tunable Temperature Amplifier. *EPL* **118,** 68004 (2017).

95. Tam, M., Thomas, G. & Golubev, D. S. Photonic Heat Transport from Weak to Strong Coupling. *Phys. Rev. B* **107,** 104518 (2023).

96. Yeyati, A. L., Subero, D., Pekola, J. P. & Sánchez, R. Photonic Heat Transport through a Josephson Junction in a Resistive Environment. *Phys. Rev. B* **110,** L220502 (2024).

97. Partanen, M. *et al.* Flux-Tunable Heat Sink for Quantum Electric Circuits. *Sci Rep* **8,** 6325 (2018).

98. Martínez-Pérez, M. J., Solinas, P. & Giazotto, F. Coherent Caloritronics in Josephson-Based Nanocircuits. *J Low Temp Phys* **175,** 813–837 (2014).

99. Fornieri, A., Timossi, G., Bosisio, R., Solinas, P. & Giazotto, F. Negative Differential Thermal Conductance and Heat Amplification in Superconducting Hybrid Devices. *Phys. Rev. B* **93,** 134508 (2016).

100. Martínez-Pérez, M. J. & Giazotto, F. Efficient Phase-Tunable Josephson Thermal Rectifier. *Applied Physics Letters* **102,** 182602 (2013).

101. Fornieri, A., Blanc, C., Bosisio, R., D'Ambrosio, S. & Giazotto, F. Nanoscale Phase Engineering of Thermal Transport with a Josephson Heat Modulator. *Nature Nanotech* **11,** 258–262 (2016).

102. Wang, L. & Li, B. Thermal Logic Gates: Computation with Phonons. *Phys. Rev. Lett.* **99,** 177208 (2007).

103. Wang, L. & Li, B. Thermal Memory: A Storage of Phononic Information. *Phys. Rev. Lett.* **101,** 267203 (2008).

104. Li, N. *et al.* Colloquium: Phononics: Manipulating Heat Flow with Electronic Analogs and Beyond. *Rev. Mod. Phys.* **84,** 1045–1066 (2012).

105. Clarke, J. & Braginski, A. I. *The SQUID Handbook: Applications of SQUIDs and SQUID Systems* (John Wiley & Sons, 2006).

106. Aspnes, D. E. Dielectric Functions and Optical Parameters of Si, Ge, GaP, GaAs, GaSb, InP, InAs, and InSb from 1.5 to 6.0 eV. *Phys. Rev. B* **27,** 985–1009 (1983).

107. Singh, P. *et al.* Multiplexed Readout of Superconductor–Normal-Conductor–Superconductor Bolometers. *J. Appl. Phys.* **138** (2025).

108. Karimi, B. *et al.* Bolometric Detection of Josephson Radiation. *Nat. Nanotechnol.* **19,** 1613–1618 (2024).

109. Ibabe, Á. *et al.* Heat Dissipation Mechanisms in Hybrid Superconductor–Semiconductor Devices Revealed by Joule Spectroscopy. *Nano Lett.* **24,** 6488–6495 (2024).

110. Nakamura, S. *et al.* Probing Fast Quantum Circuit Refrigeration in the Quantum Regime. *Phys. Rev. Appl.* **23,** L011003 (2025).

111. Li, B., Wang, L. & Casati, G. Thermal Diode: Rectification of Heat Flux. *Phys. Rev. Lett.* **93,** 184301 (2004).